AN EXPERIMENTAL ANALYSIS OF A CYLINDRICAL SHOCK WAVE FOR USE IN A CYLINDRICAL GAS DYNAMIC LASER

Daniel Richard Donoghue

DUDLEY KNOX LIBRARY
NAVAL POSTGRADUATE SCHOOL
MONTEREY, CALIFORNIA 93940

NAVAL POSTGRADUATE SCHOOL
Monterey, California

THESIS

AN EXPERIMENTAL ANALYSIS
OF A
CYLINDRICAL SHOCK WAVE FOR USE
IN A
CYLINDRICAL GAS DYNAMIC LASER

by

Daniel Richard Donoghue

June 1975

Thesis Advisor: A.E. Fuhs

Approved for public release; distribution unlimited.

T168491

REPORT DOCUMENTATION PAGE

READ INSTRUCTIONS
BEFORE COMPLETING FORM

1. REPORT NUMBER	2. GOVT ACCESSION NO.	3. RECIPIENT'S CATALOG NUMBER

4. TITLE (and Subtitle) An Experimental Analysis of a Cylindrical Shock Wave For Use in a Cylindrical Gas Dynamic Laser	5. TYPE OF REPORT & PERIOD COVERED Master's Thesis; June 1975
	6. PERFORMING ORG. REPORT NUMBER
7. AUTHOR(s) Daniel Richard Donoghue	8. CONTRACT OR GRANT NUMBER(s)
9. PERFORMING ORGANIZATION NAME AND ADDRESS Naval Postgraduate School Monterey, California 93940	10. PROGRAM ELEMENT, PROJECT, TASK AREA & WORK UNIT NUMBERS
11. CONTROLLING OFFICE NAME AND ADDRESS Naval Postgraduate School Monterey, California 93940	12. REPORT DATE June 1975
	13. NUMBER OF PAGES 148
14. MONITORING AGENCY NAME & ADDRESS(if different from Controlling Office)	15. SECURITY CLASS. (of this report) Unclassified
	15a. DECLASSIFICATION/DOWNGRADING SCHEDULE

16. DISTRIBUTION STATEMENT (of this Report)

Approved for public release; distribution unlimited.

17. DISTRIBUTION STATEMENT (of the abstract entered in Block 20, if different from Report)

18. SUPPLEMENTARY NOTES

19. KEY WORDS (Continue on reverse side if necessary and identify by block number)

Cylindrical Shock Wave
Cylindrical Gas Dynamic Laser

20. ABSTRACT (Continue on reverse side if necessary and identify by block number)

The goal of this research was to experimentally demonstrate the feasibility of a cylindrical shock wave to serve as the major pressure recovery mechanism for either cylindrical gas dynamic lasers or chemical lasers. An analysis was conducted to determine the minimum distance between the nozzle exit cylinder and the shock wave location, $r_m - r_e$, required for power

(20. ABSTRACT Continued)

extraction. A cylindrical nozzle array was designed using the axisymmetric method of characteristics for a Mach number of 4.5 with a flexibility of other Mach numbers. A chamber incorporating end wall boundary layer bleed and ejectors for back pressure control was designed and built. The apparatus was run up to a pressure of 18 atmospheres. Three flow regimes were identified. A value of $(r_m - r_e)/(r_s - r_e)$ of 0.3 was attained, where r_s is the shock wave location. Flow in the end wall nozzles consisted of a Coanda jet with a subsonic flow region adjacent to the wall; flow was not altered by boundary layer bleed. Except for the end wall nozzles a cylindrical shock wave was established.

An Experimental Analysis
# of a
Cylindrical Shock Wave For Use
in a
Cylindrical Gas Dynamic Laser

by

Daniel Richard Donoghue
Ensign, United States Navy
B.S., United States Naval Academy, 1974

Submitted in partial fulfillment of the
requirements for the degree of

MASTER OF SCIENCE IN AERONAUTICAL ENGINEERING

from the

NAVAL POSTGRADUATE SCHOOL
June 1975

Thesis
D[illegible]
c.[illegible]

DUDLEY KNOX LIBRARY
NAVAL POSTGRADUATE SCHOOL
MONTEREY, CALIFORNIA 93940

ABSTRACT

The goal of this research was to experimentally demonstrate the feasibility of a cylindrical shock wave to serve as the major pressure recovery mechanism for either cylindrical gas dynamic lasers or chemical lasers. An analysis was conducted to determine the minimum distance between the nozzle exit cylinder and the shock wave location, $r_m - r_e$, required for power extraction. A cylindrical nozzle array was designed using the axisymmetric method of characteristics for a Mach number of 4.5 with a flexibility of other Mach numbers. A chamber incorporating end wall boundary layer bleed and ejectors for back pressure control was designed and built. The apparatus was run up to a pressure of 18 atmospheres. Three flow regimes were identified. A value of $(r_m - r_e)/(r_s - r_e)$ of 0.3 was attained, where r_s is the shock wave location. Flow in the end wall nozzles consisted of a Coanda jet with a subsonic flow region adjacent to the wall; flow was not altered by boundary layer bleed. Except for the end wall nozzles a cylindrical shock wave was established.

TABLE OF CONTENTS

I. INTRODUCTION ---------------------------------- 12

II. CYLINDRICAL LASER GEOMETRY ------------------ 16

- A. PREVIOUS GDL ------------------------------ 16
- B. THEORETICAL POWER OUTPUT -------------- 18

III. EXPERIMENTAL DEVELOPMENT ------------------- 24

- A. DESCRIPTION OF EXPERIMENT ------------- 24
- B. CYLINDRICAL NOZZLE FEED SYSTEM --------- 29
- C. NOZZLE DESIGN --------------------------- 47
- D. EJECTOR DESIGN -------------------------- 59
- E. BOUNDARY LAYER BLEED ------------------- 62
- F. EXPERIMENTAL PROCEDURE ---------------- 71

IV. RESULTS AND CONCLUSIONS -------------------- 75

- A. RESULTS ---------------------------------- 75
- B. CONCLUSIONS AND RECOMMENDATIONS -------- 100

APPENDIX A: THEORETICAL LASING POWER AVAILABLE ---- 102

APPENDIX B: CALCULATIONS FOR DETERMINING INLET (FEED) AREA ------------------------------ 109

APPENDIX C: DETAILS OF THROAT HEIGHT CALCULATIONS --------------------------- 110

APPENDIX D: AXIAL VARIATION OF MACH NUMBER AND PRESSURE ------------------------------ 113

APPENDIX E: DETERMINING POINTS ON THE NOZZLE WALL - 120

APPENDIX F: EJECTOR NOZZLE DESIGN ----------------- 127

APPENDIX G: LISTING OF BOUNDARY LAYER BLEED PROGRAM ------------------------------- 144

LIST OF REFERENCES ------------------------------- 146

INITIAL DISTRIBUTION LIST ------------------------- 147

LIST OF TABLES

Table No.

1 Throat Height and Exit Mach Number for Various Inlet Mach Numbers --------------- 38

2 Radial Variation of Mach Number and Pressure ---------------------------------- 48

3 Description of Wall Contour -------------- 57

4 Flow Conditions for Boundary Layer Bleed (From Ref. 8) ---------------------- 68

5 Wall Static Pressure at Nozzle Exit and Calculated Mach Number --------------- 83

D-1 Symbols for Computer Program AXIAL ------- 116

E-1 Results of Axisymmetric Method of Characteristics -------------------------- 123

F-1 Symbols for Computer Program EJECTOR ----- 141

LIST OF FIGURES

Figure No.

1 Schematic of a Cylindrical GDL (From Ref. 2) ---------------------------- 13

2 Schematics of Linear GDL's
(a) Closed Cycle
(b) Open Cycle --------------------------- 15

3 Schematic of Cylindrical GDL with Diffusers --------------------------- 17

4 AVCO Everett Test Rig (From Ref. 2) ------ 19

5 Cylindrical Nozzle Stack with Lasing Mirrors --------------------------- 20

6 Outer Radius of Lasing Mirror VS. Nozzle Stack Length --------------------- 23

7 Cylindrical Nozzle Test Rig ------------- 26

8 Assembled Nozzle Stack (Courtesy NWC, China Lake) -------------- 27

9 Disassembled Nozzle Stack (Courtesy NWC, China Lake) -------------- 28

10 Side View Photograph of Single Nozzle Ring (Courtesy NWC, China Lake) ---------- 31

11 Dimensions of Nozzle Ring (Side View) ---- 32

12 End View Photograph of Single Nozzle Ring (Courtesy NWC, China Lake) ---------- 33

13 Dimensions of Nozzle Ring (End View) ----- 34

14 End View of Nozzle Stack ----------------- 35

15 Throat Height VS. Inlet Mach Number ------ 39

16 Exit Mach Number VS. Inlet Mach Number --- 40

17 Exit Mach Number VS. Throat Height ------- 41

18 Mach Number VS. Axial Station ------------ 45

Figure No.

19 Pressure VS. Axial Station ---------------- 46

20 Mach Number VS. Radius -------------------- 49

21 Pressure VS. Radius ----------------------- 50

22 Characteristic Element -------------------- 53

23 Complete Characteristic Network ----------- 54

24 Nozzle Wall Contour: Fourth Degree Polynomial Fit to Calculated Wall Points --- 58

25 Detail of Nozzle Ring Trailing Edge -------- 60

26 Detail of Nozzle Ring Throat -------------- 61

27 Back Pressure VS. Exhaust Width with Ejector Nozzle Diameter as a Parameter ----- 63

28 Boundary Layer Bleed Flow Model (From Ref. 8) ------------------------------ 66

29 Fraction of Boundary Layer Bleed as a Function of Pressure Ratio and Non-dimensional Bleed Slot Width (From Ref. 8) - 67

30 Bleed Hole Design ------------------------- 69

31 Nozzle Stack With Boundary Layer Bleed ----- 70

32 Photograph of Experimental Apparatus ------- 73

33 Schlieren Photographs of Normal Shocks Standing in Six Nozzles
(a) 70 PSI
(b) 130 PSI -------------------------------- 76

34 Schlieren Photographs of Four Nozzles Before "Starting"
(a) No Flow
(b) 50 PSI --------------------------------- 77

35 Schlieren Photographs of Center Three Nozzles Starting
(a) 75 PSI
(b) 100 PSI – First Shock Structure Established ---------------- 78

Figure No.

36 Schematic of Coanda Jet Formation
(a) Flow at Pressure Less than 50 PSI
(b) Resulting Coanda Jet Attached to Nozzle Wall ---------------------------- 79

37 Schematic of Flow at a Total Pressure of 100 PSI --------------------------------- 80

38 Schlieren Photograph of Flow Just Before Transition to Second Flow Structure – Total Pressure 125 PSI -------------------- 81

39 Wall Static Pressure VS. Total Pressure --- 84

40 Wall Mach Number VS. Total Pressure ------- 85

41 Schlieren Photographs Showing Curved Shock Segments Beyond Trailing Edges of Nozzle After Transition to Second Stage
(a) 150 PSI
(b) 175 PSI -------------------------------- 89

42 Schlieren Photographs of Probe Showing Regions of Subsonic Flow
(a) 150 PSI – Subsonic Behind Curved Shock Segment
(b) 150 PSI – Subsonic in Wall Region ----- 90

43 Schematic of the Flow Structure at a Total Pressure of 175 PSI ----------------- 91

44 Schlieren Photograph of Flow Just Before Developing to Third Stage – Total Pressure 200 PSI -------------------- 92

45 Schlieren Photographs Showing Development of Flow into Third Stage
(a) 220 PSI
(b) 240 PSI -------------------------------- 93

46 Schlieren Photograph of Flow at Maximum Total Pressure of 250 PSI. Normal Shock Segments Approximately 3/8 inch from Trailing Edges ---------------------------- 96

47 Schematic of the Flow Structure at a Total Pressure of 250 PSI ----------------- 97

48 Schlieren Photographs of Flow with Boundary Layer Bleed Applied to Upper Plate ------------------------------------ 99

Figure No.

A-1 Lasing Mirror Intensity Loading ---------- 103
D-1 Axial Flow Model ------------------------- 114
E-1 Modified Characteristic Element ---------- 121
F-1 Ejector Nozzle Flow Model ---------------- 128
F-2 Top View of Ejector Flow Model ----------- 129
F-3 Ejector Flow Mixing Model ---------------- 135
F-4 Ejector Nozzle Geometry ------------------ 139

SPECIAL NOTE:

During reproduction the quality of the Schlieren and shadowgraph photographs are degraded. Glossy prints are available upon request from Professor A. E. Fuhs, Department of Mechanical Engineering, Naval Postgraduate School, Monterey, California, 93940.

ACKNOWLEGEMENT

The author wishes to express his most sincere gratitude and appreciation to Professor Allen E. Fuhs of the Naval Postgraduate School for his help in the preparation and execution of this project. The research was motivated by a request from Ronald Dettling of the Naval Weapons Center, China Lake. Funding support for this project was provided by Naval Air Systems Command, Code 320, William Volz. The nozzles were fabricated by the Naval Weapons Center, China Lake, through the cooperation of Mr. Ronald Dettling. This help is greatly appreciated. The author would also like to express his gratitude to Mr. Donald Harvey for the fabrication of the test apparatus, and to my dear wife for her help in the preparation of this report and for her moral support throughout its development.

I. INTRODUCTION

At present there are three types of lasers that employ supersonic flow: chemical, CO electrical, and gas dynamic. All three are capable of producing large amounts of lasing power, but are restricted to use in platforms that are not limited by weight and volume. Due primarily to the large diffusers necessary to restore the flow to ambient pressure, large volume and weight are required to handle a given flow.

A cylindrical geometry gas dynamic laser has advantages not found in the other supersonic lasers mentioned:

(1) diffuserless operation
(2) elimination of nozzle bending stresses
(3) elimination of boundary layer corner interactions.

Such a geometry would result in a compact system achieving lasing by rapid expansion in the radial direction rather than linearly as is presently done. The supersonic radial flow is then slowed to subsonic and raised to near ambient pressures by traveling through a cylindrical shock wave sufficiently downstream of the nozzles to allow for a reasonably large lasing cavity. A cylindrical shock wave eliminates the need for diffusers, thereby reducing the weight and volume of the device considerably.

Supersonic conditions are achieved from flow traveling through axially symmetric nozzle rings, thus eliminating nozzle bending stresses found in linear gas dynamic lasers. A schematic of a cylindrical GDL is shown in figure (1).

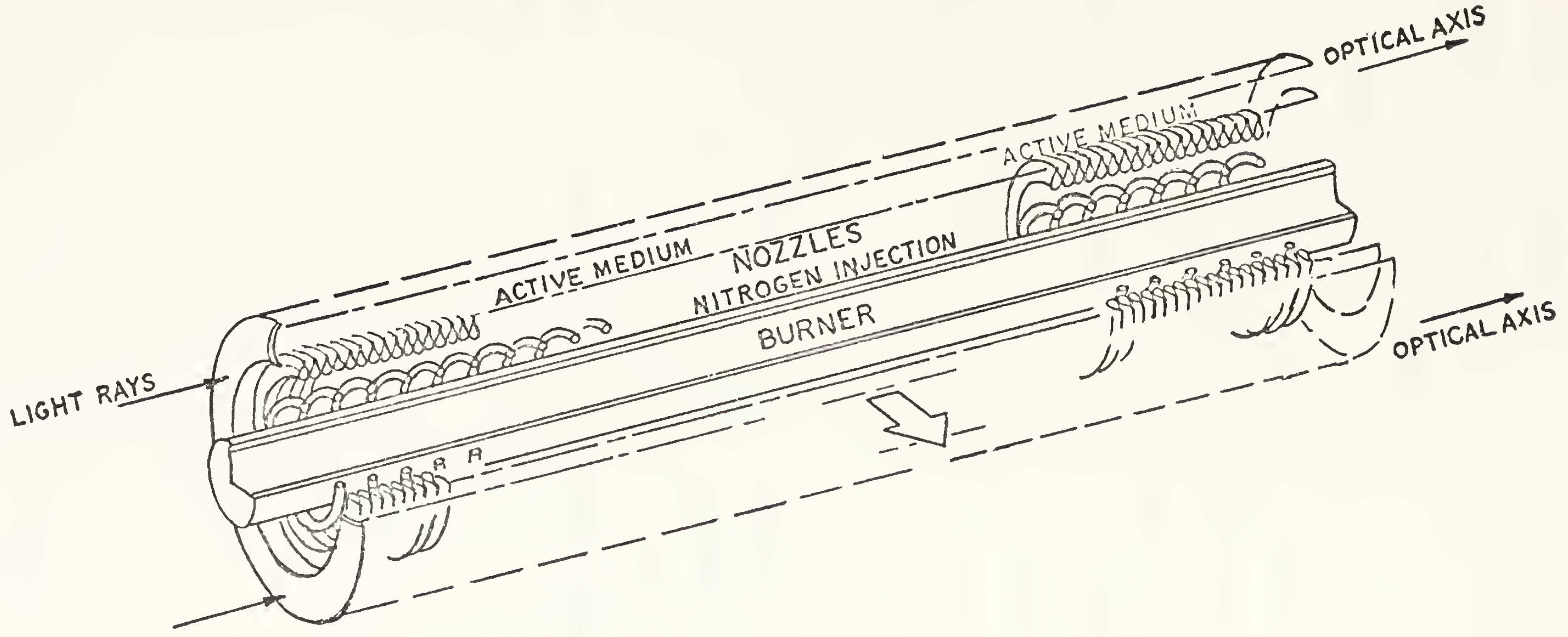
OPTICAL AXIS
ACTIVE MEDIUM
ACTIVE MEDIUM
NOZZLES
NITROGEN INJECTION
BURNER
LIGHT RAYS
OPTICAL AXIS

FIGURE 1 SCHEMATIC OF A CYLINDRICAL GDL (FROM REF. 2)

Figure (2) shows schematic diagrams of two types of linear GDL's. Boundary layer buildup on the four walls of the lasing cavity interact at the corners, creating increased possibilities of flow separation and non-homogeneous conditions in the lasing medium. By having a flat plate at each end of the nozzle stack, the cylindrical geometry would eliminate such interaction. Since the radial flow experiences increasing area as it moves outward, the boundary layer buildup on each plate is less than in the linear case.

A cold flow test of a number of nozzle rings was conducted to establish a cylindrical shock wave and to determine whether such an apparatus is feasible for use in a cylindrical gas dynamic laser.

A theoretical power output example is included in section II of this report. Section III contains the development of the nozzle feed, the nozzle ring geometry and the ejector and boundary layer bleed systems. Experimental results are described in section IV.

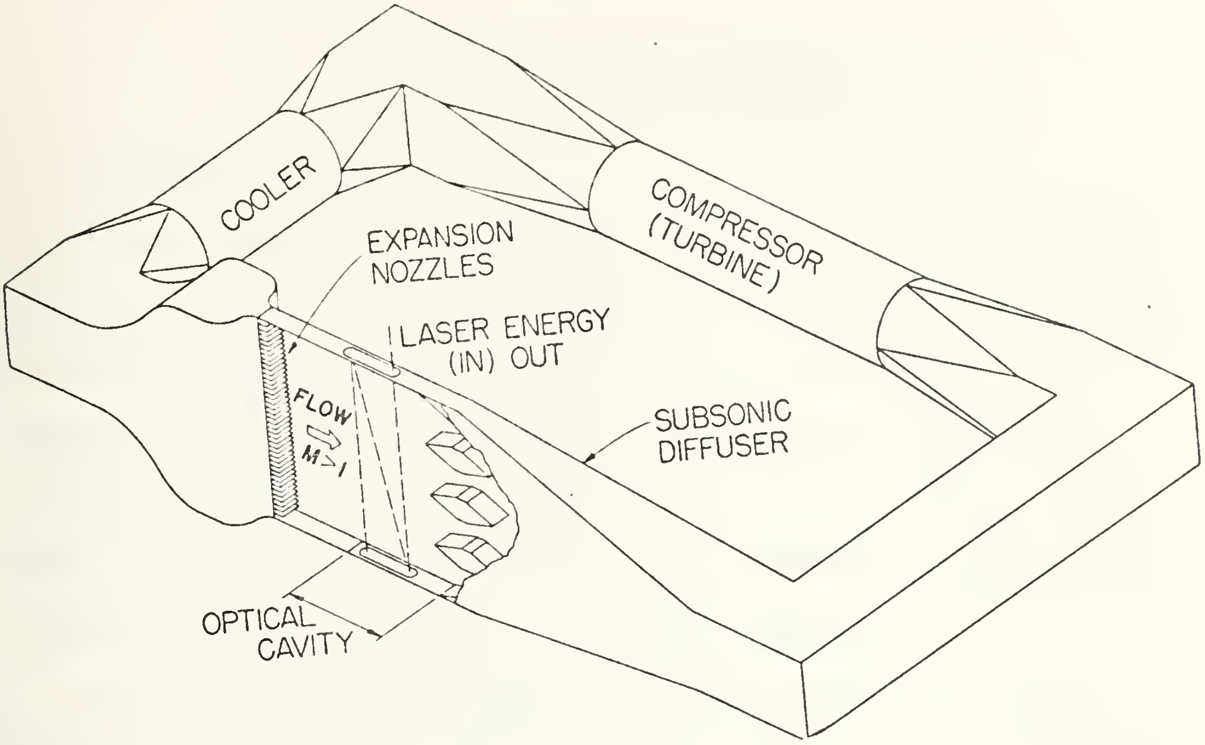
COOLER
COMPRESSOR (TURBINE)
EXPANSION NOZZLES
LASER ENERGY (IN) OUT
FLOW
M>1
SUBSONIC DIFFUSER
OPTICAL CAVITY

(a) Closed Cycle

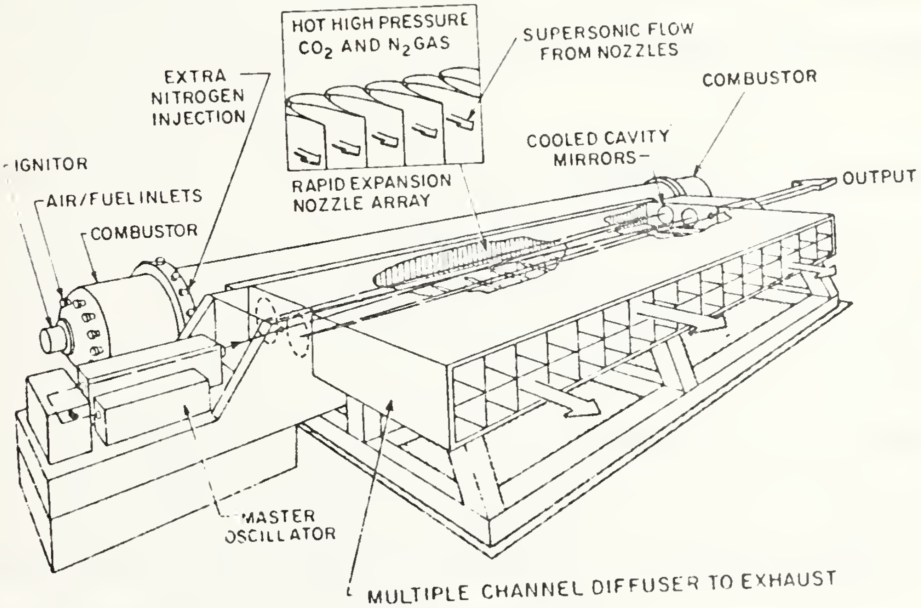
HOT HIGH PRESSURE CO_2 AND N_2 GAS
SUPERSONIC FLOW FROM NOZZLES
COMBUSTOR
EXTRA NITROGEN INJECTION
COOLED CAVITY MIRRORS
IGNITOR
OUTPUT
AIR/FUEL INLETS
RAPID EXPANSION NOZZLE ARRAY
COMBUSTOR
MASTER OSCILLATOR
MULTIPLE CHANNEL DIFFUSER TO EXHAUST

(b) Open Cycle

FIGURE (2) SCHEMATICS OF LINEAR GDL'S
(FROM REF. 5)

II. CYLINDRICAL LASER GEOMETRY

A. PREVIOUS GDL'S

Linear gas dynamic lasers are currently in use and have successfully produced laser beams in the order of a megawatt of power. These devices are quite large and heavy, thus limiting their use in operating environments (such as an aircraft) where such parameters are limited. These limitations are due primarily to the large diffusers necessary to return the supersonic flow to ambient pressure.

A cylindrical GDL could reduce the weight and volume necessary to handle a given flow by expansion to supersonic velocities in the radial direction and returning to ambient pressure by means of a cylindrical shock wave. Other advantages include elimination of bending stresses and reduced boundary layer interferences.

Ortwerth [Ref. (1)] designed a cylindrical source flow device, but retained diffusers similar to those used in linear GDL's. The diffusers were aligned radially as shown in figure (3). Such a design reduces the volume required of such a device by having an annular lasing cavity rather than a linear one. Retaining the diffusers does not allow for the substantial reductions in weight and volume that a cylindrical shock wave would facilitate.

Sponsored by the Air Force Weapons Laboratory, the AVCO Everett Research Laboratory [Ref. (2)] conducted an extensive

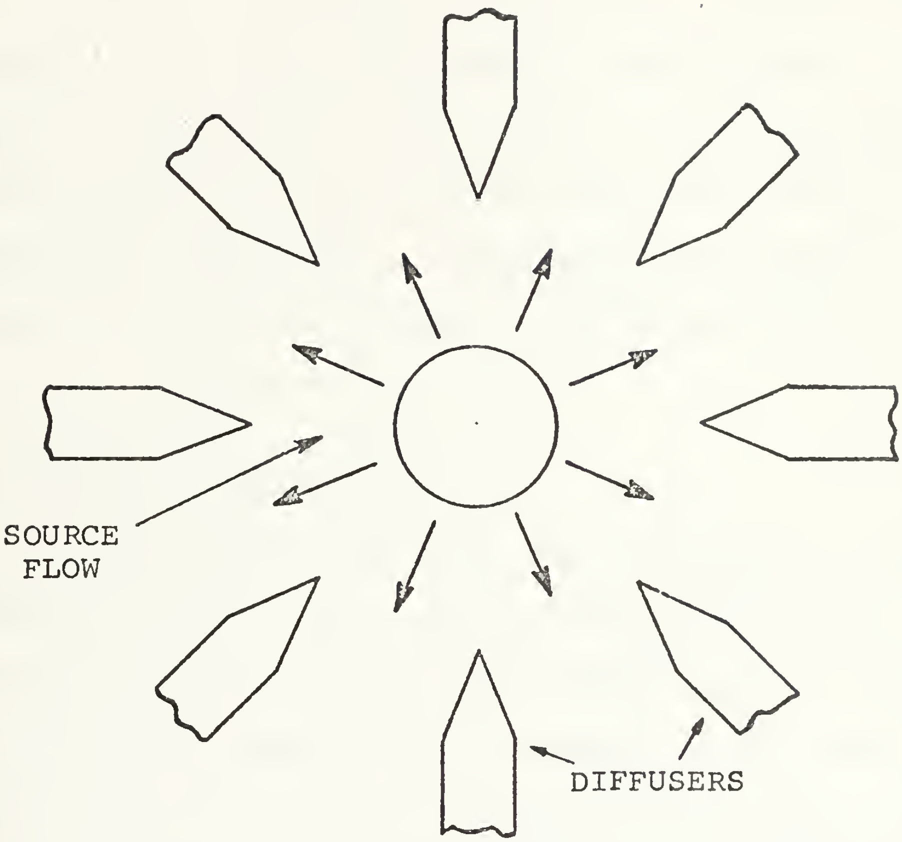
SOURCE FLOW
DIFFUSERS

FIGURE (3) SCHEMATIC OF A CYLINDRICAL GDL WITH DIFFUSERS

theoretical program to establish the feasibility of cylindrical source flow for a cylindrical GDL. Included in the program was a cold flow test of one nozzle ring which established supersonic flow at the predicted mach number but failed to create a cylindrical shock wave. Results showed that homogeneity of the lasing medium can be made acceptable. Separation of the boundary layer interfered with the establishment of a cylindrical shock wave, and it was recommended that some type of boundary layer control be used.

Figure (4) shows the assembly used in the AVCO Everett test.

B. THEORETICAL POWER OUTPUT

In a linear GDL the diffusers can be placed far enough downstream so that a large lasing cavity is assured. In a cylindrical GDL the width of the lasing cavity is determined by the shock location. To extract all the power available from a given flow, the cylindrical shock must not occur too near the nozzle exit. Figure (5) shows the nozzle stack with the lasing mirrors.

Assuming a Gaussian intensity distribution on each mirror, the intensity I is given by

$$I(r) = I_{peak} e^{-r^2 c} \quad . \tag{1}$$

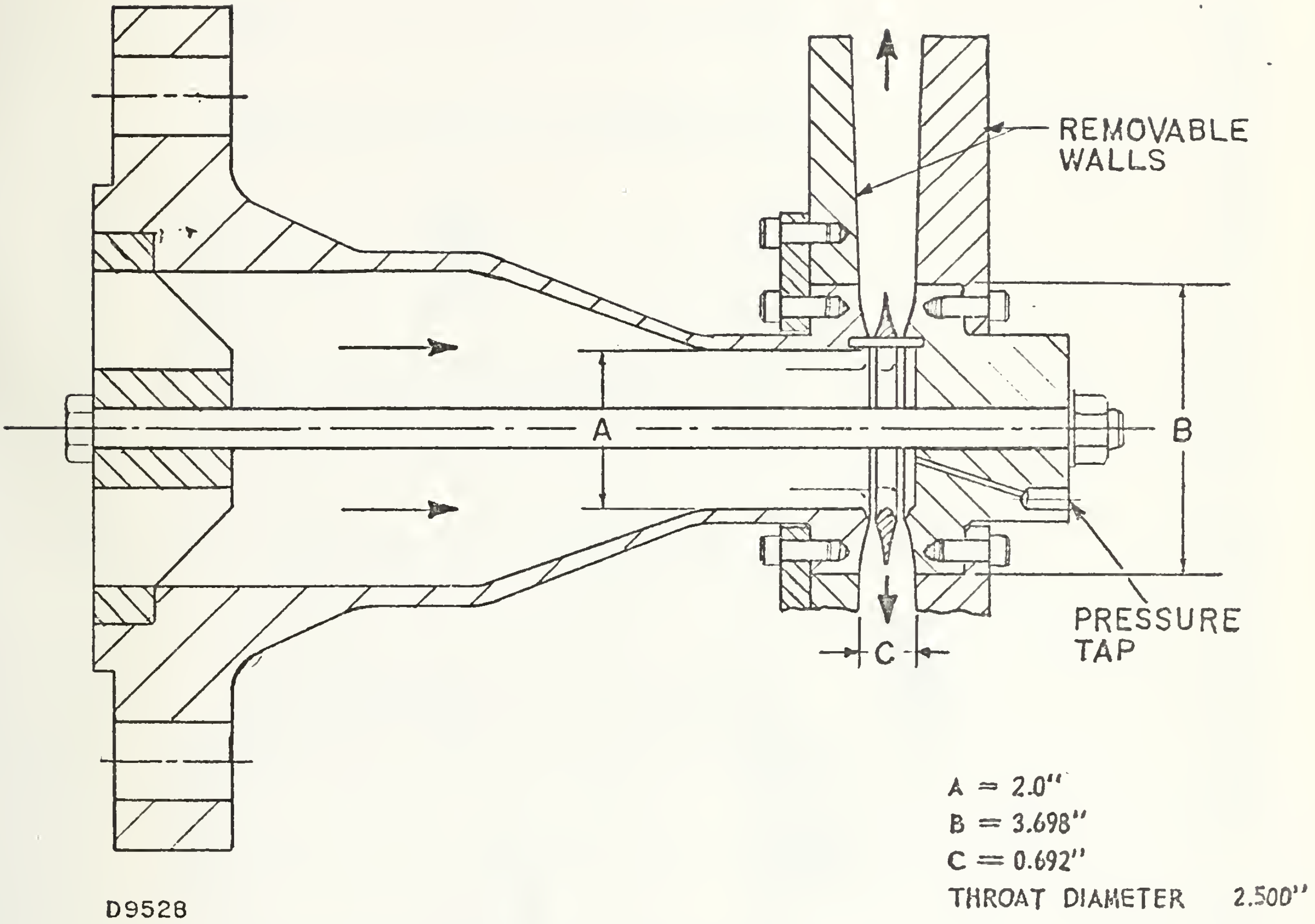
REMOVABLE WALLS
A
B
C
PRESSURE TAP
A = 2.0"
B = 3.698"
C = 0.692"
THROAT DIAMETER 2.500"
D9528

FIGURE (4) AVCO EVERETT TEST RIG (FROM REF. 2)

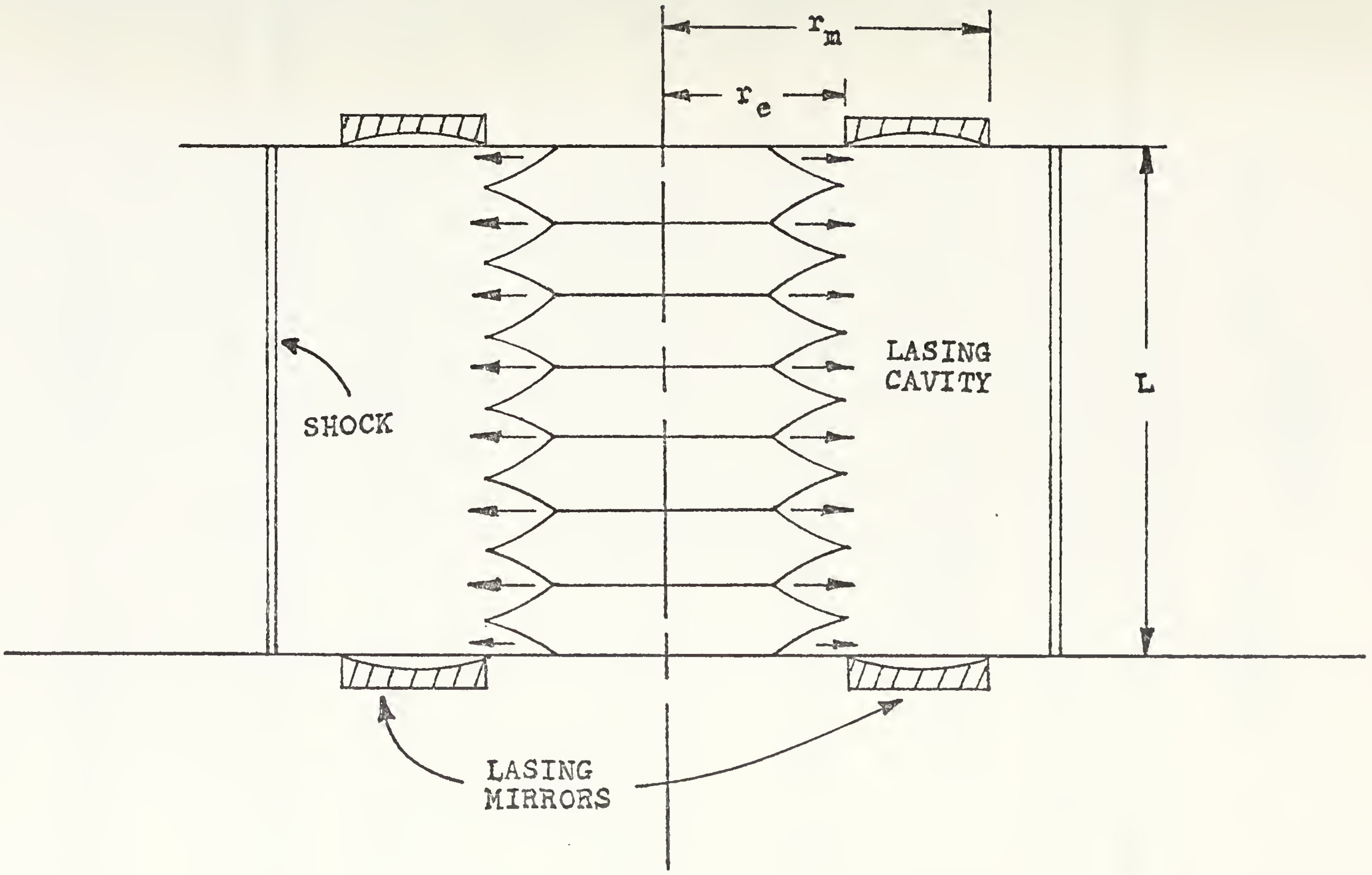
r_m
r_e
LASING CAVITY
L
SHOCK
LASING MIRRORS

FIGURE (5) CYLINDRICAL NOZZLE STACK WITH LASING MIRRORS

Satisfying the boundary conditions and re-defining r yields

$$I(r) = I_p e^{-[\frac{r-\bar{r}}{r_e-\bar{r}}\sqrt{2}\,]^2} \quad \frac{\text{kilowatts}}{\text{cm}^2} \tag{2}$$

where r_e and r are shown in figure (A-1) in Appendix A.

Integrating over the mirror area gives the total power

$$P = 2\ I_p \int_{r_e}^{r_m} r\ \exp[\frac{r-\bar{r}}{r_e-\bar{r}}\sqrt{2}\ ]^2\ dr \tag{3}$$

An alternate method of finding the power available from the flow is

Power = (mass flow rate) x (specific energy)

or

$$P = 2\ r_e\ L\rho_o a_o(\rho/\rho_o)(a_e/a_o)\ M_e \text{ x } (E) \text{ kilowatts} \tag{4}$$

where subscripts "e" and "o" refer to exit and stagnation conditions respectively. Equating equations (3) and (4) gives

$$I_p \int_{r_e}^{r_m} r\ \exp[\frac{r-\bar{r}}{r_e-\bar{r}}\sqrt{2}\ ]^2\ dr = r_e\ L\rho_o a_o(\rho/\rho_o)(a_e/a_o)\ M_e\ E \tag{5}$$

where the only unknown is the outer radius of the mirror, r_m.

Performing the integral in equation (5) and solving for r_m.

$$r_m = \sqrt{r_e^2 + c} \tag{6}$$

$$\text{where} \quad c = \frac{4r_e \, L\rho_o a_o (a/a_o) M_e \, E(\rho/\rho_o)}{\sqrt{\frac{\pi}{2}} \, I_p \, \mathrm{erf}(\sqrt{2})}$$

Using the values for the constants listed in Appendix A, equation (6) reduces to

$$r_m = \sqrt{2.13 + .2692\ L} \tag{7}$$

where L is the overall length of the nozzle stack. Figure (6) shows the minimum shock location for increasing nozzle stack length.

For six nozzle rings, the outer radius of the mirrors is 1.77 inches. Using this value in equation (3), the power is found to be 32 kilowatts. Details of the theoretical power available calculations are shown in Appendix A.

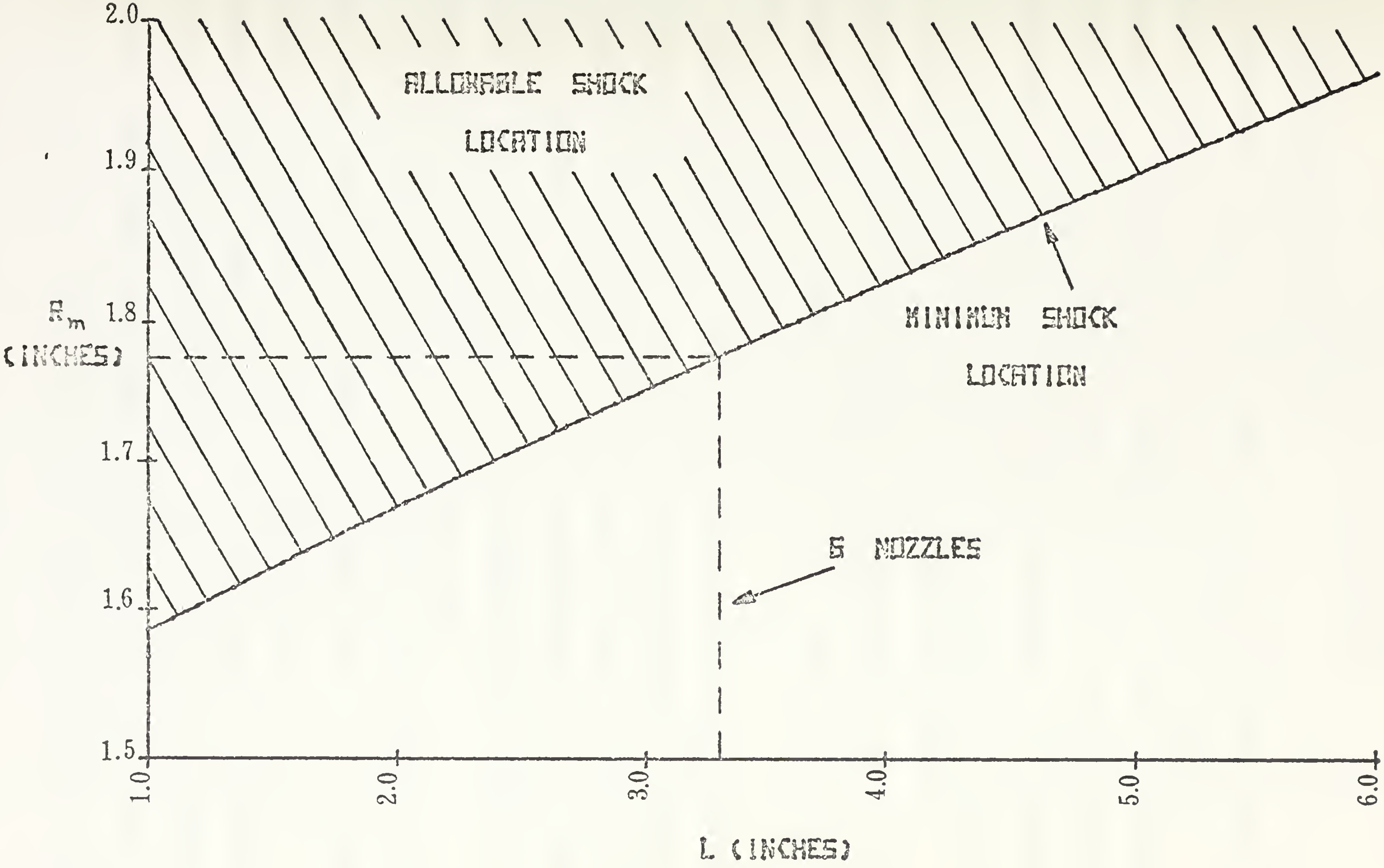

FIGURE (6) OUTER RADIUS OF LASING MIRROR VS. NOZZLE STACK LENGTH

III. EXPERIMENTAL DEVELOPMENT

A. DESCRIPTION OF EXPERIMENT

Reference 2 is a final report of analytical and experimental programs conducted by the AVCO Everett Research Laboratory to determine the feasibility of using a cylindrical geometry for a gas dynamic laser. The Naval Weapons Center, China Lake, California, expressed an interest in the concept of a cylindrical GDL and requested that research be conducted to determine whether a cylindrical shock wave could be established by incorporating the recommendations of the AVCO Everett report. Funding of this project was provided by Naval Air Systems Command, Code 320.

Before determining the actual shape of the nozzle rings (see figures (8) and (9)), it was first necessary to calculate the throat height, that is, the spacing between each nozzle ring in the stack. This spacing is determined by the mass flow that could be supplied to the nozzle stack, which is limited by the feed holes. See figure (14).

Once the throat height was determined, the exit to throat area ratio, and thus the exit Mach number, was found from the geometry of the nozzle rings. The axisymmetric method of characteristics found in Ref. 3 was then used to determine the contour of the nozzle walls. Once the equation describing the wall shape was calculated, the design was sent to the machine facility at NWC, China Lake, where the nozzle rings

were fabricated. Figures (8), (9), (10), (12) and (14) were provided by NWC, China Lake.

To prevent separation of the boundary layer at the shock location, suction was used to bleed off the low energy flow in the lower portion of the boundary layer. Extensive analytical investigation of supersonic boundary layer bleed was conducted and is found in section III-D of this report.

The loss in total pressure across a normal shock of the strength anticipated resulted in total pressure downstream of the shock (using a reservoir pressure of ten atmospheres) to be less than one atmosphere. Ejector nozzles were necessary to lower the back pressure seen by the flow exiting the nozzle rings and thus allow them to start. Design of the ejector apparatus is found in section III-E of this report.

Figure (7) shows the assembled experimental apparatus with dimensions. The design allowed for testing of up to eight nozzles at the design Mach number. The assembly shown was attached to the free jet located in building 230 of the Naval Postgraduate School. Air was supplied to the free jet from a 2400 cubic foot tank capable of pressure up to three hundred pounds per square inch. The moisture was removed from the air before it entered the tank by means of a hydryer. A model 06231 Lammert Industries vacuum pump was used to evacuate a 200 cubic foot tank to provide suction for boundary layer bleed.

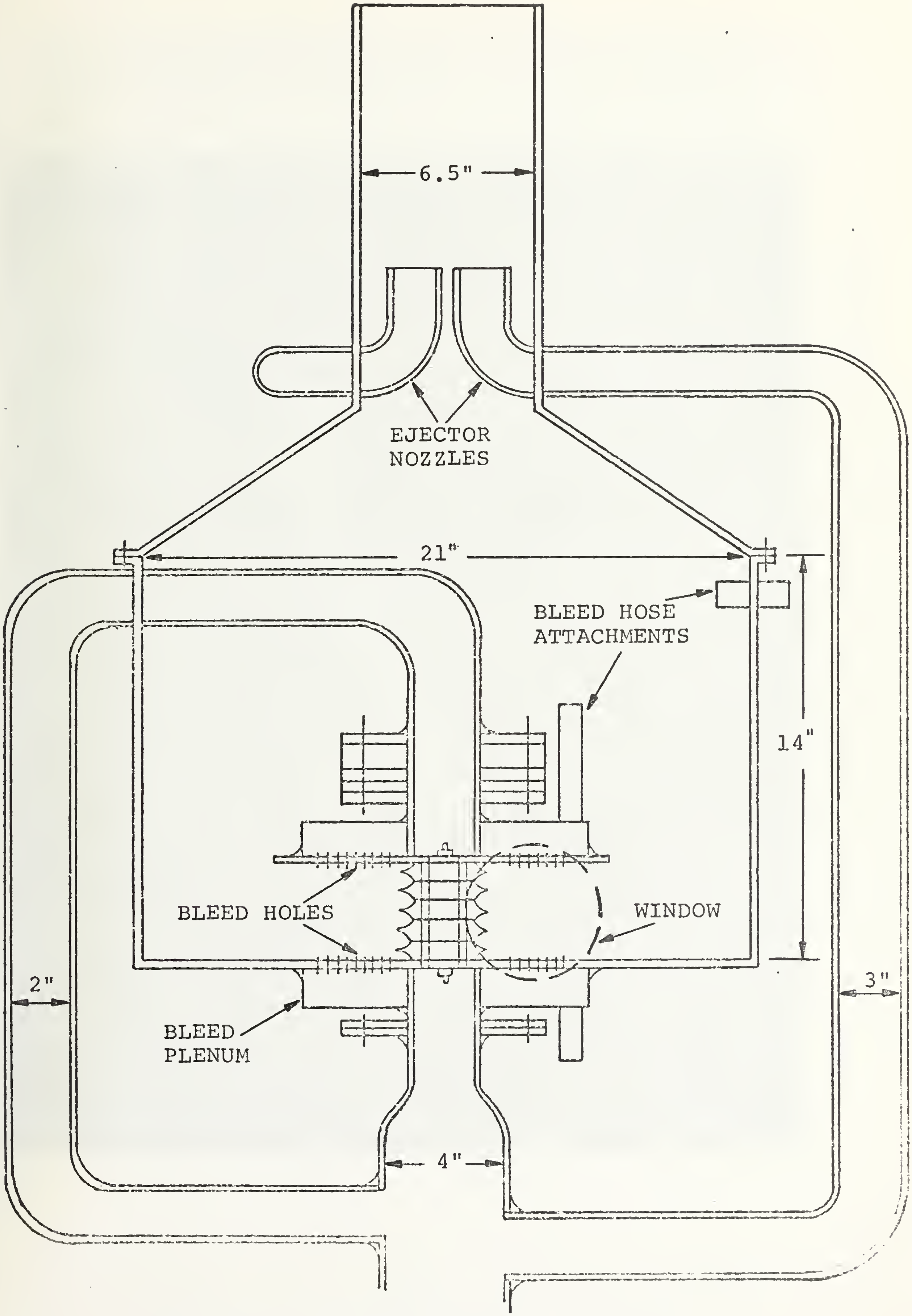
6.5"
EJECTOR
NOZZLES
21"
BLEED HOSE
ATTACHMENTS
14"
BLEED HOLES
WINDOW
2"
3"
BLEED
PLENUM
4"

FIGURE (7) CYLINDRICAL NOZZLE TEST RIG

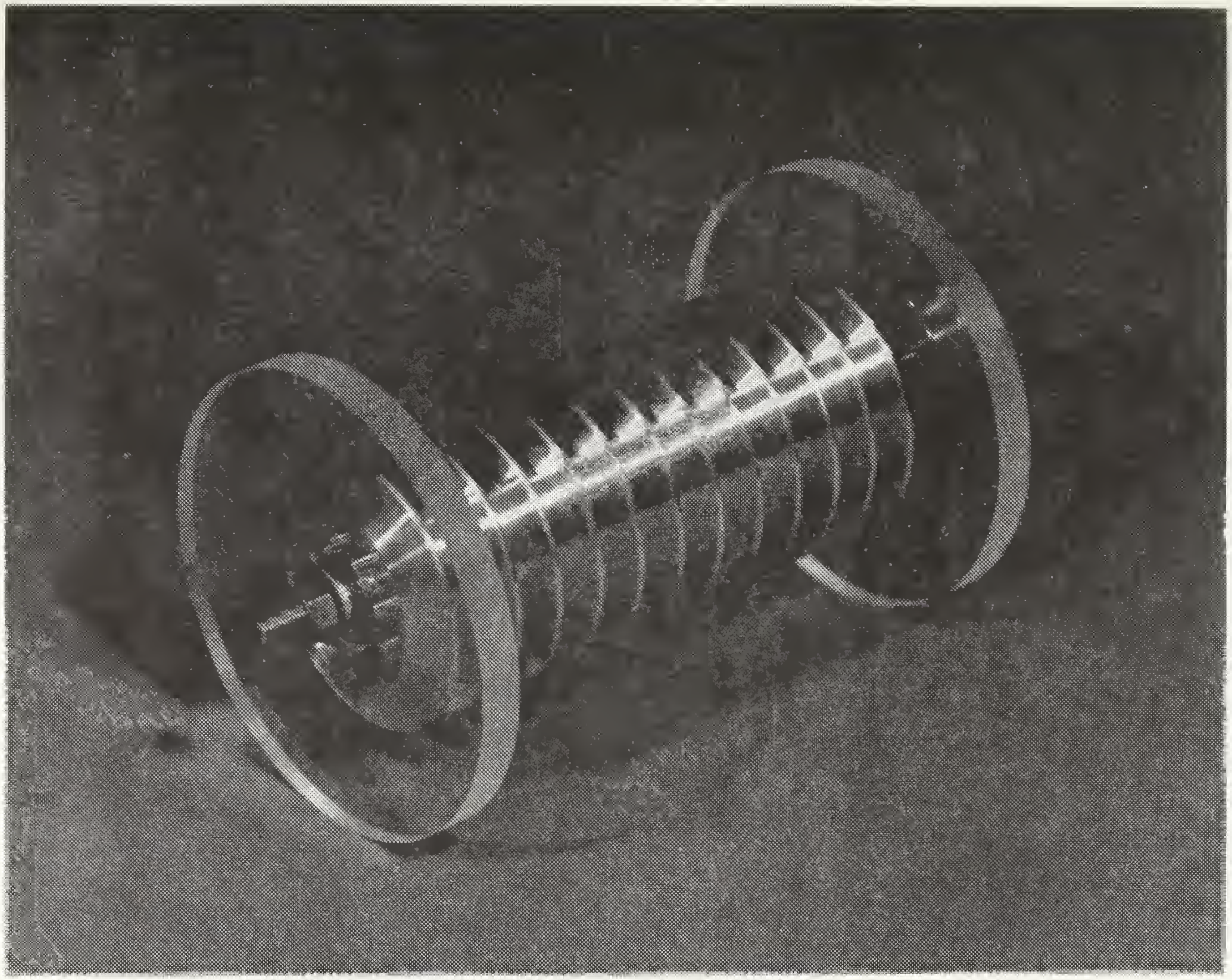

FIGURE (8) ASSEMBLED NOZZLE STACK (COURTESY NWC, CHINA LAKE)

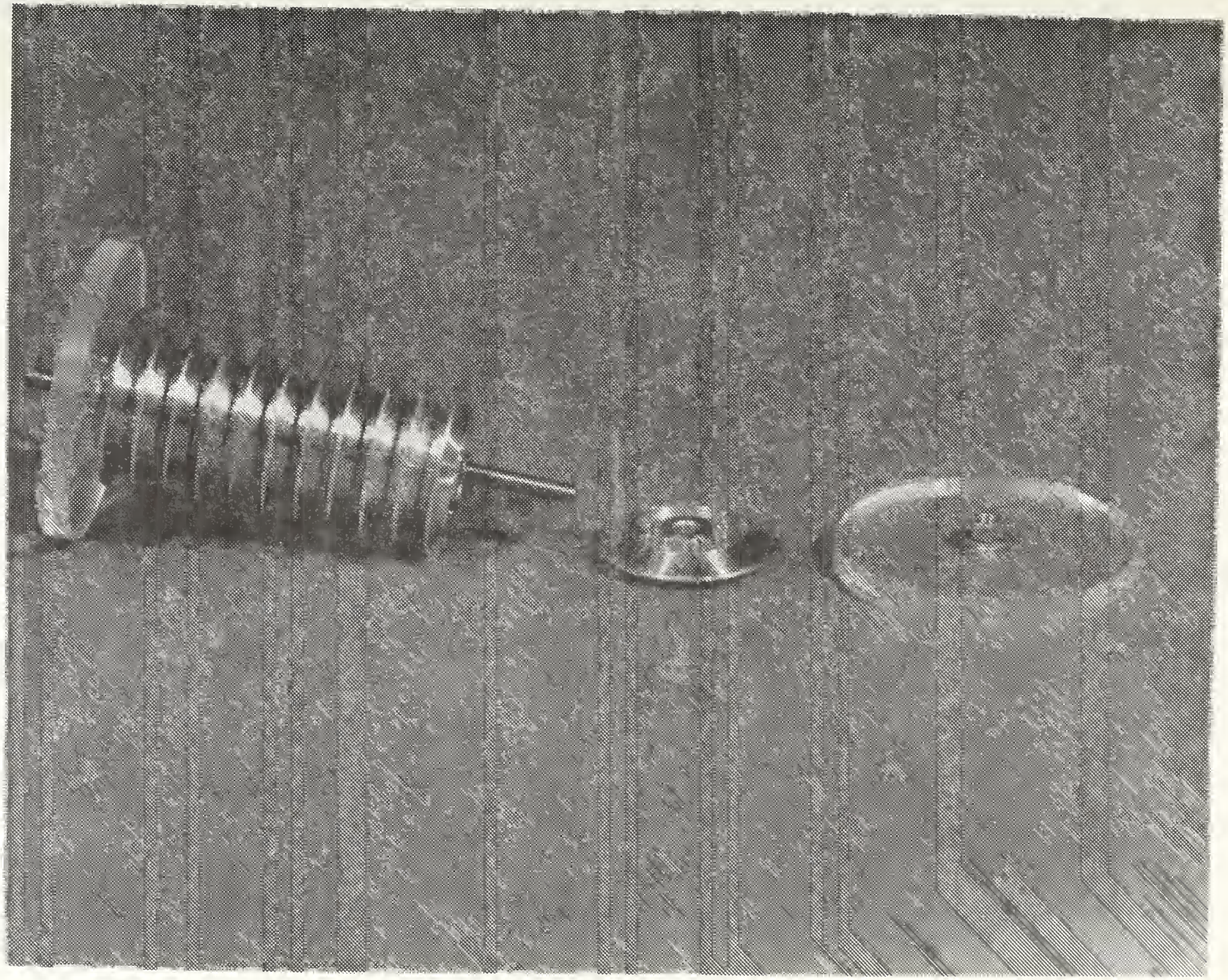

FIGURE (9) DISASSEMBLED NOZZLE STACK (COURTESY NWC, CHINA LAKE)

B. NOZZLE FEED SYSTEM

1. Throat Height

It was found, as expected, that the throat height was the most critical dimension of the entire design. A relatively large throat height is desirable in that the ratio of the nozzle exit area to the throat area is kept small, thus keeping the exit Mach number reasonably low. This would have the advantages of ease in starting and smaller total pressure loss across the shock.

A large throat height also requires large mass flow requirements, and the amount of air that can be fed to the nozzle rings is limited by the inlet holes in the center of each ring. Figures (10) through (14) show the dimensions and photographs of the nozzle rings. The area of the feed holes must be greater than the combined throat areas of the nozzle ring stack to prevent choking of the flow at the feed holes. Thus if many nozzle rings are to be tested, an extremely small throat height must be used. This would result in a number of complications:

(i) An excessively large A_{exit}/A_{throat}, causing high supersonic or hypersonic flow at the nozzle exit and thereby creating a problem in starting and a large loss in total pressure across the shock.

(ii) Extreme heat concentrations at the throat (not a problem in cold flow testing).

(iii) Difficulty in fabricating spacing washers of uniform thickness, causing unacceptable variations in the flow due to changes in the throat height.

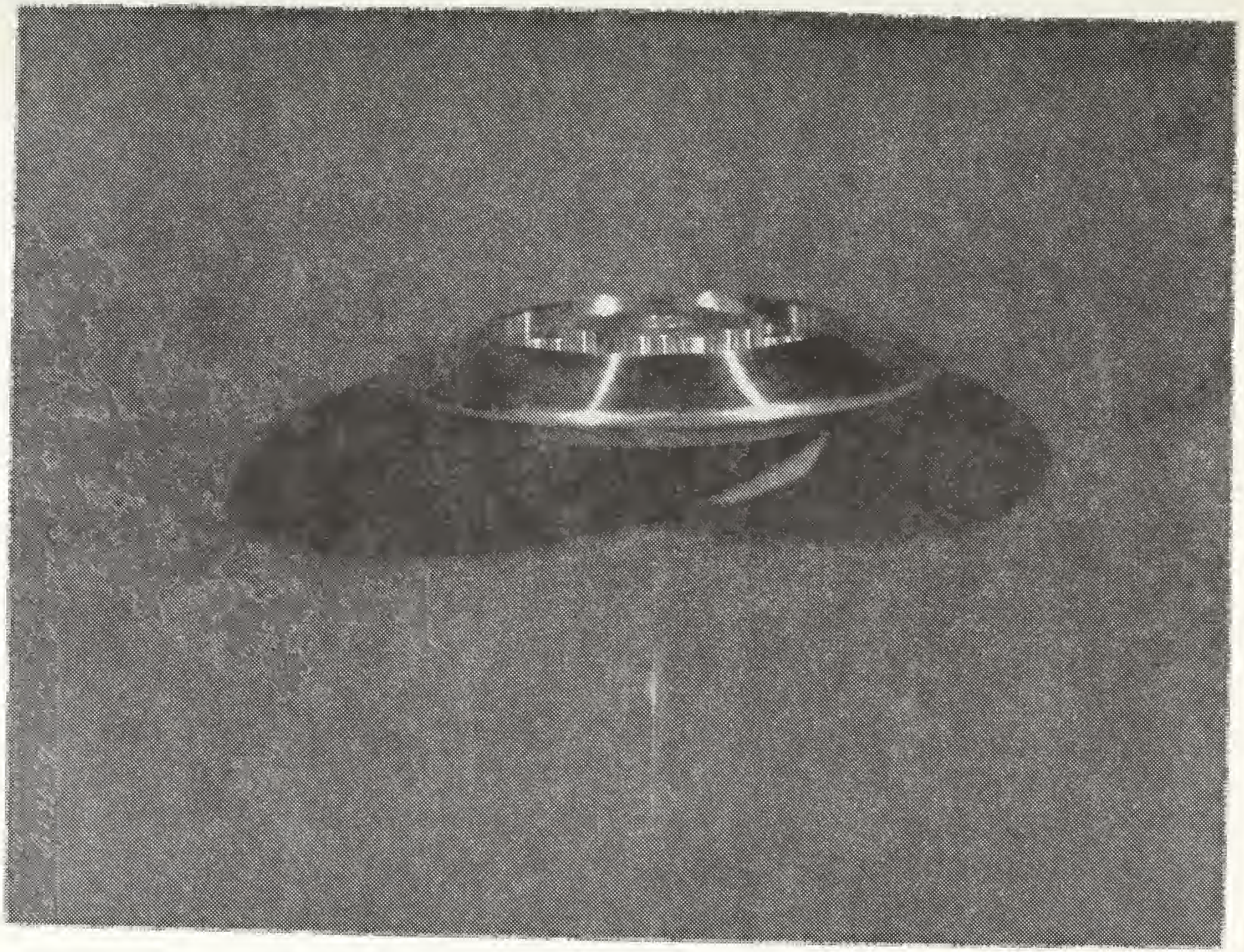

FIGURE (10) SIDE VIEW PHOTOGRAPH OF SINGLE NOZZLE RING (COURTESY NWC, CHINA LAKE)

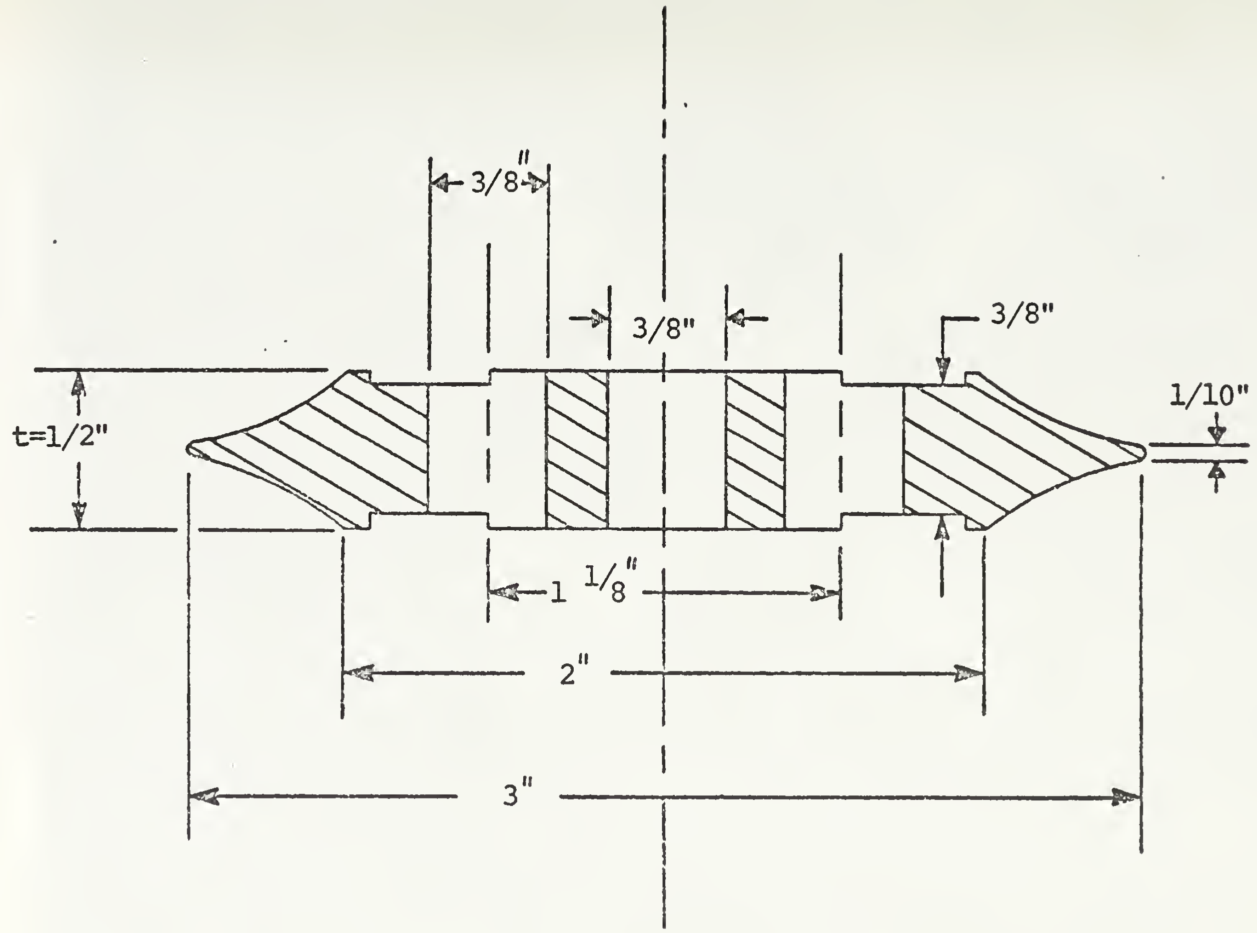
3/8"
3/8"
3/8"
1/10"
t=1/2"
1 1/8"
2"
3"

FIGURE (11) DIMENSIONS OF NOZZLE RING (SIDE VIEW)

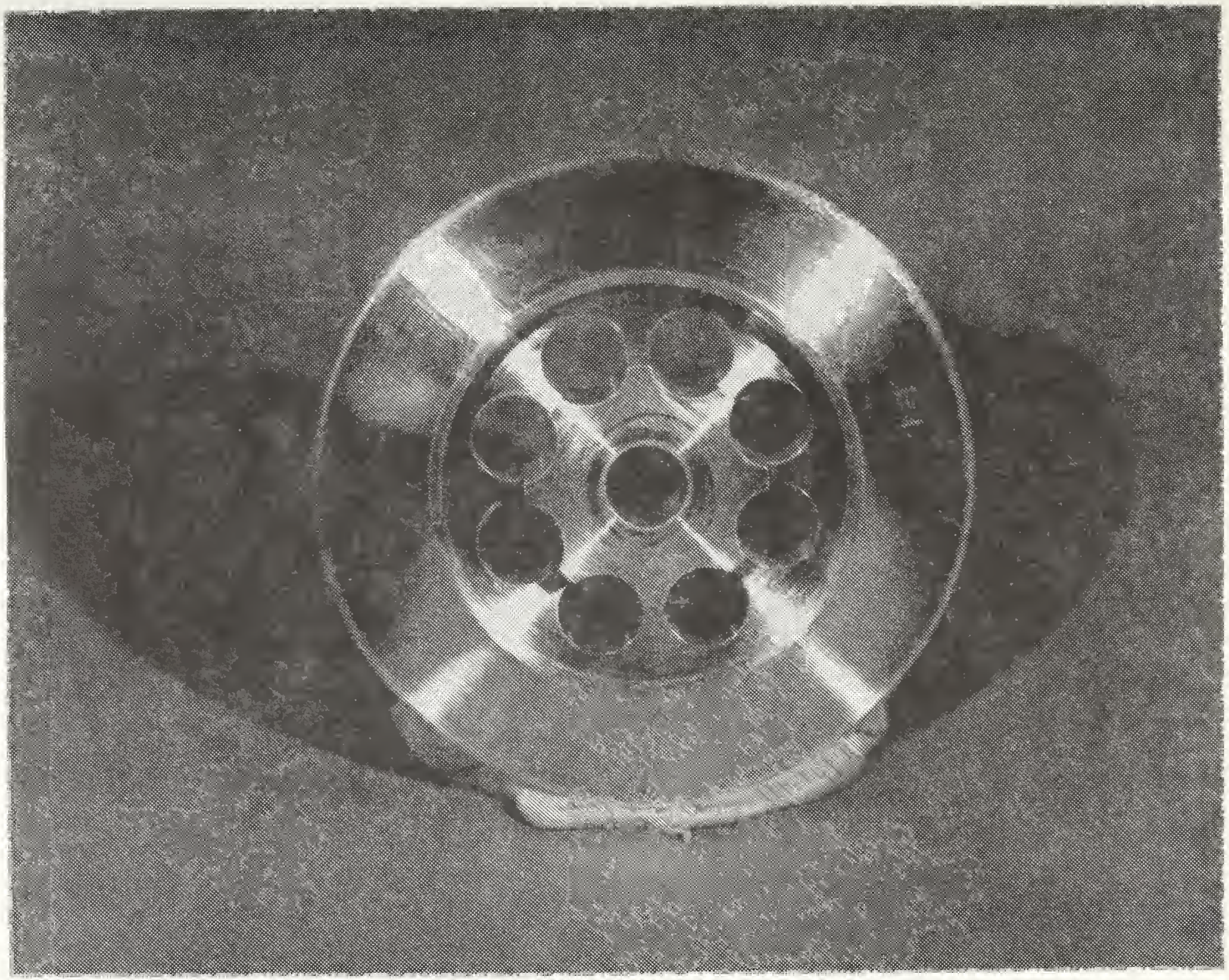

FIGURE (12) END VIEW PHOTOGRAPH OF SINGLE NOZZLE RING (COURTESY NWC, CHINA LAKE)

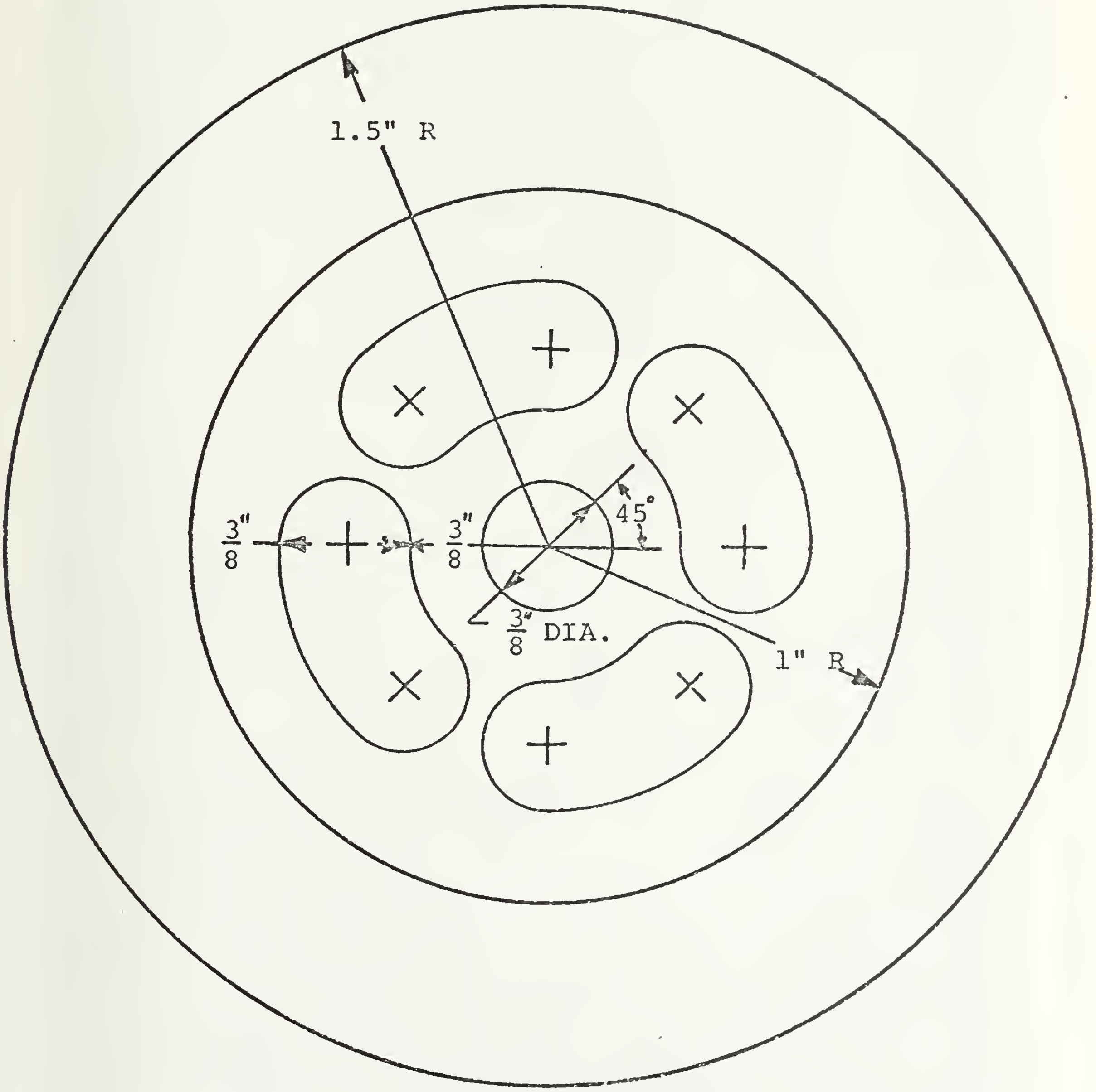
1.5" R
3"/8
3"/8
45°
3"/8 DIA.
1" R

FIGURE (13) DIMENSIONS OF NOZZLE RING (END VIEW)

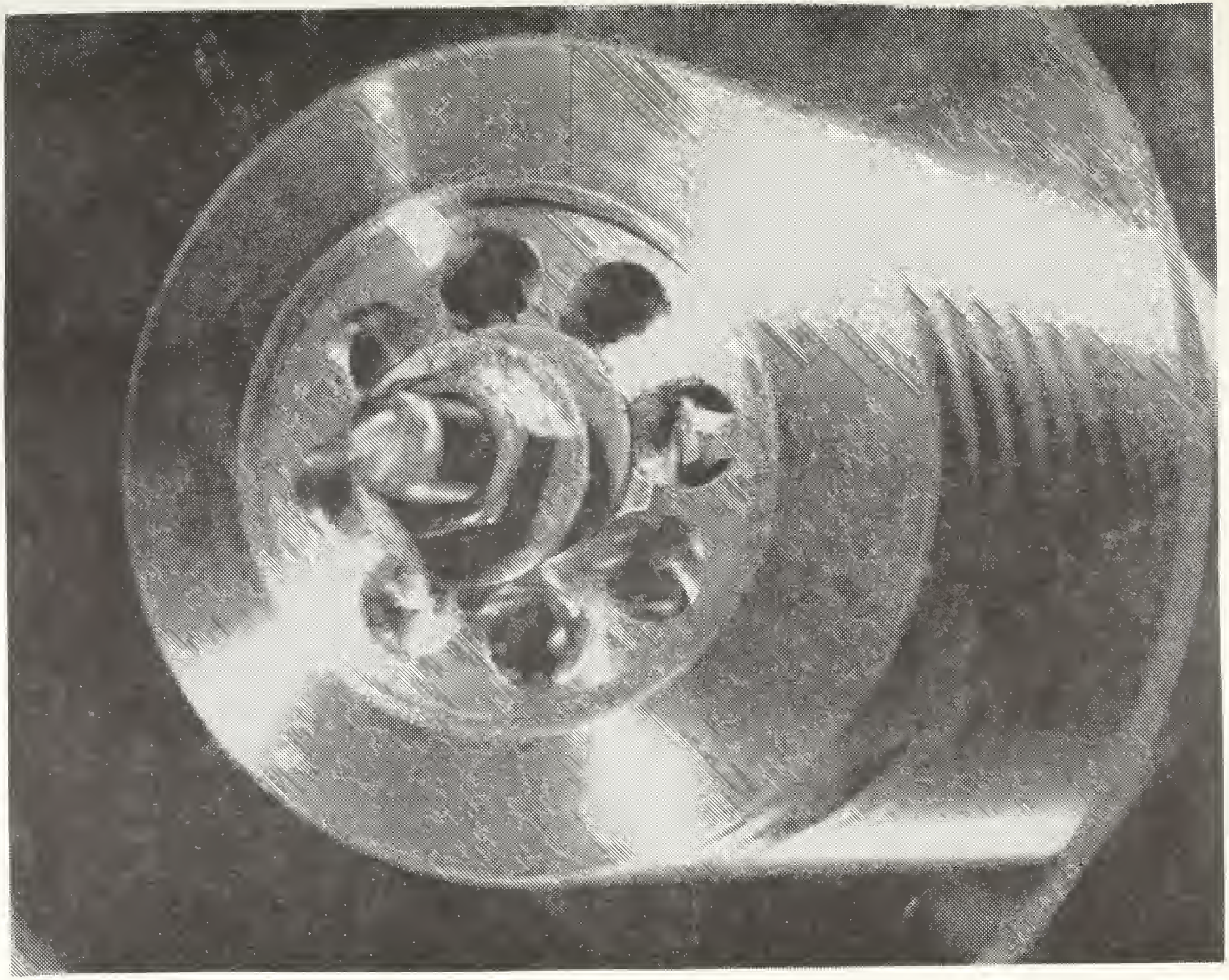

FIGURE (14) END VIEW OF NOZZLE STACK

The throat height must satisfy the continuity equation:

$$\dot{m}_{in} = \sum_{n=1}^{6} \dot{m}_n$$

where n is the number of nozzle rings. This can also be expressed as

$$(2\rho_{in}U_{in}A_{in})^{\dagger} = 6\rho^*U^*A^* \quad . \qquad (1)$$

Rewriting equation (1) using the equation of state and solving for the throat height:

$$h = \frac{1}{6\pi} M_{in}A_{in}\left(\frac{P_{in}}{P^*}\right)\left(\frac{T^*}{T_{in}}\right)^{\frac{1}{2}}$$

Using the value of inlet area previously obtained and using the isentropic relations for pressure and temperature in equation (2), the throat height in inches can be expressed as

$$h = \frac{.092\ M}{(1 + .2M_{in}^{2})^{3}} \quad . \qquad (3)$$

[†] The factor of two in equation (1) results from the nozzle stack being fed from both ends.

Equation (3) shows that the throat height is a function of inlet Mach number only. Details of the throat height calculations are found in Appendix C.

The exit Mach number is determined by the ratio of the exit area to the throat area. This ratio is found from the geometry of figure (11) to be

$$\frac{A_{exit}}{A} = \frac{2\pi r_e(h+t)}{2\pi r_t h}$$

or

$$\frac{A_e}{A} = \frac{1.5(h+.5)}{h} \quad . \tag{4}$$

Also, assuming isentropic flow through the nozzle, the area ratio can be expressed as

$$\frac{A_e}{A} = \left[\frac{1}{M_e} \left[\left(\frac{2}{\gamma+1}\right)\left(1 + \frac{\gamma-1}{2} M_e^{\,2}\right)\right]^{\frac{\gamma+1}{2(\gamma-1)}} \right] \quad . \tag{5}$$

Equations (4) and (5) show that the exit Mach number is directly dependent upon the throat height. Since the throat height is a function only of the inlet Mach number, the exit Mach number is also a function of the inlet Mach number. The results of equations (3), (4) and (5) for various inlet Mach numbers are listed in Table (1). Figures (15) through (17) show the results of Table (1) in graphical form.

Table 1 Throat Height and Exit Mach Number for Various Inlet Mach Numbers.

M_{inlet}	h (inches)	M_{exit}
.2	.0179	5.65
.4	.0334	4.95
.6	.0446	4.62
.8	.0511	4.47

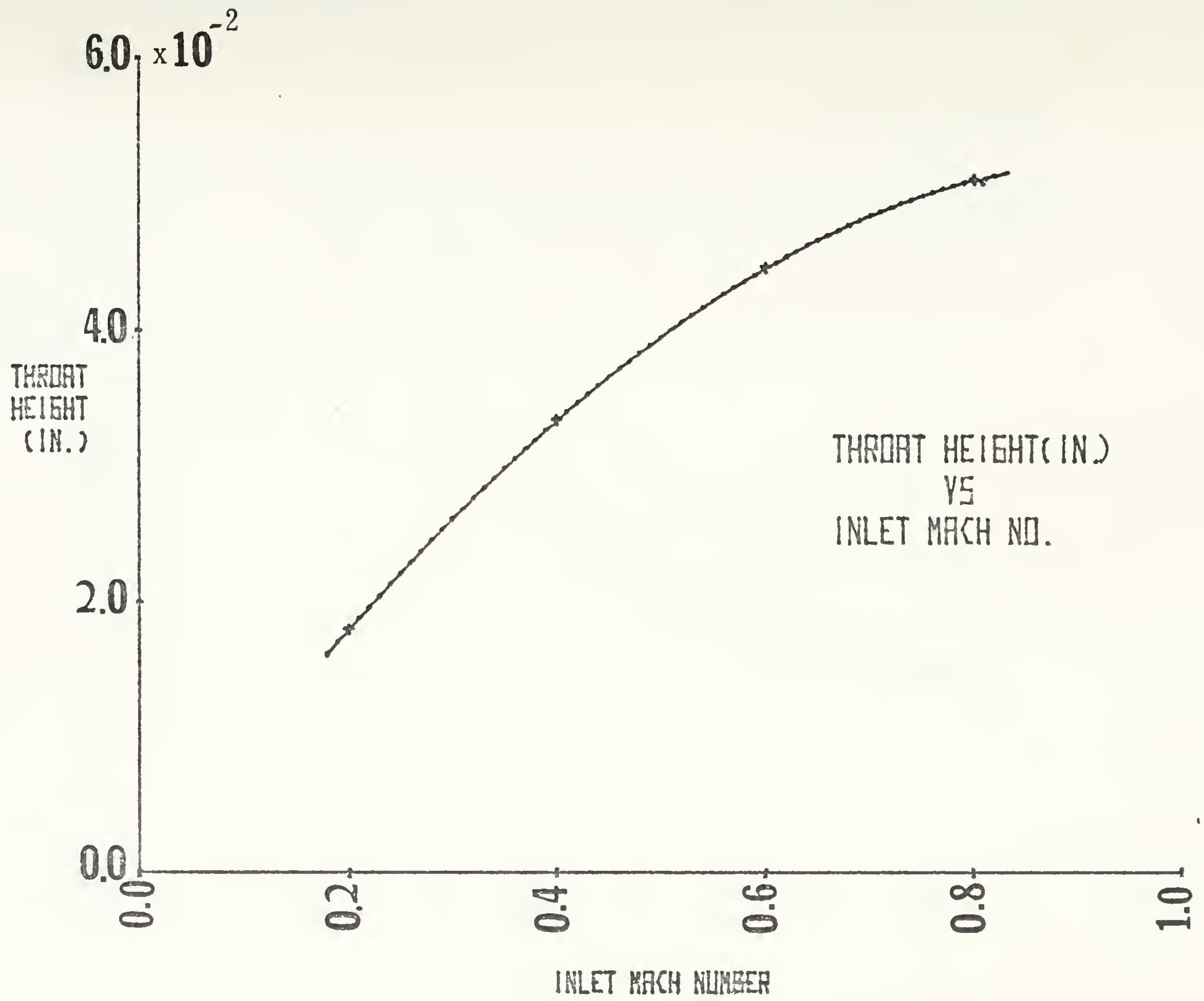

FIGURE (15) THROAT HEIGHT VS. INLET MACH NUMBER

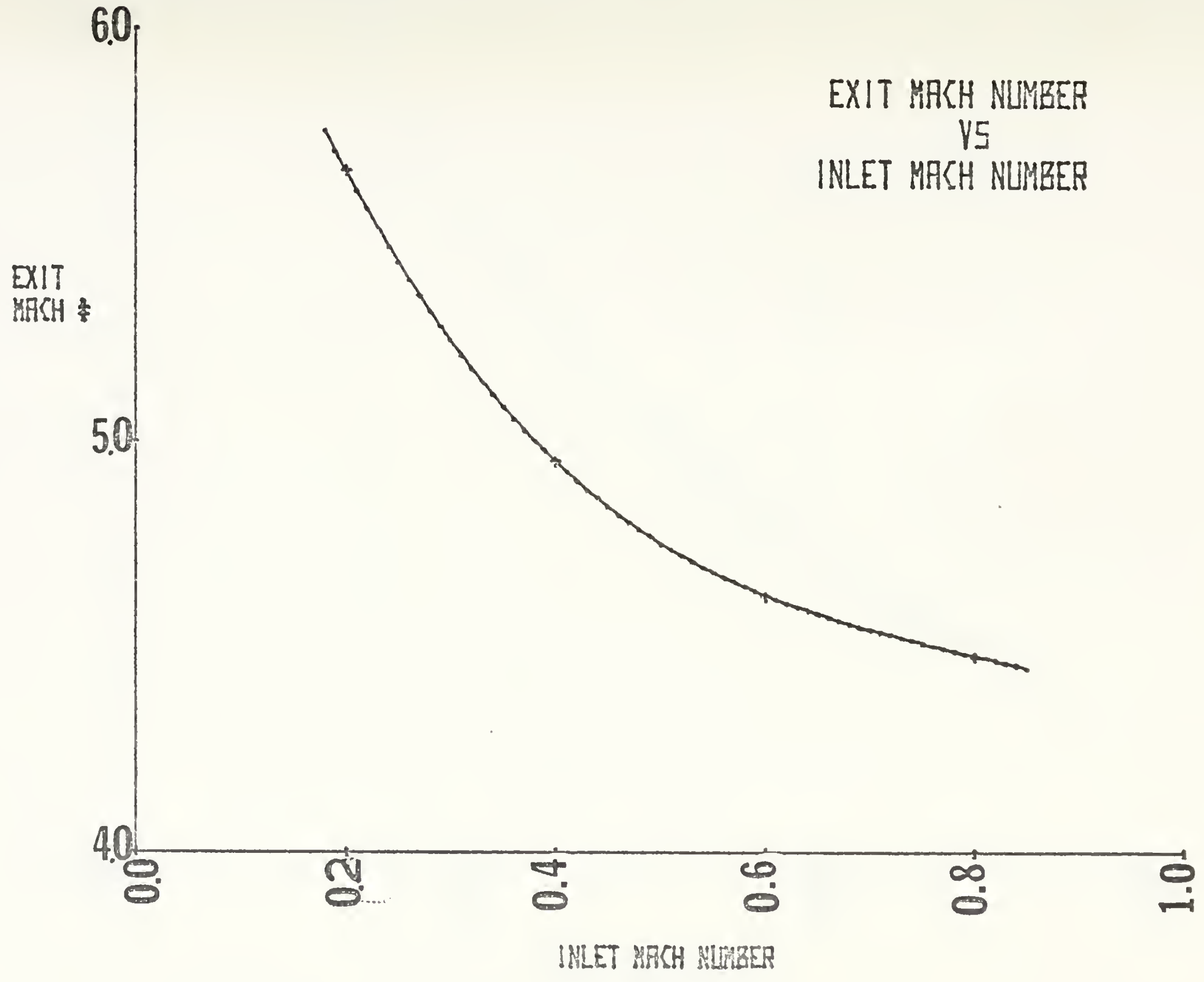

FIGURE (16) EXIT MACH NUMBER VS. INLET MACH NUMBER

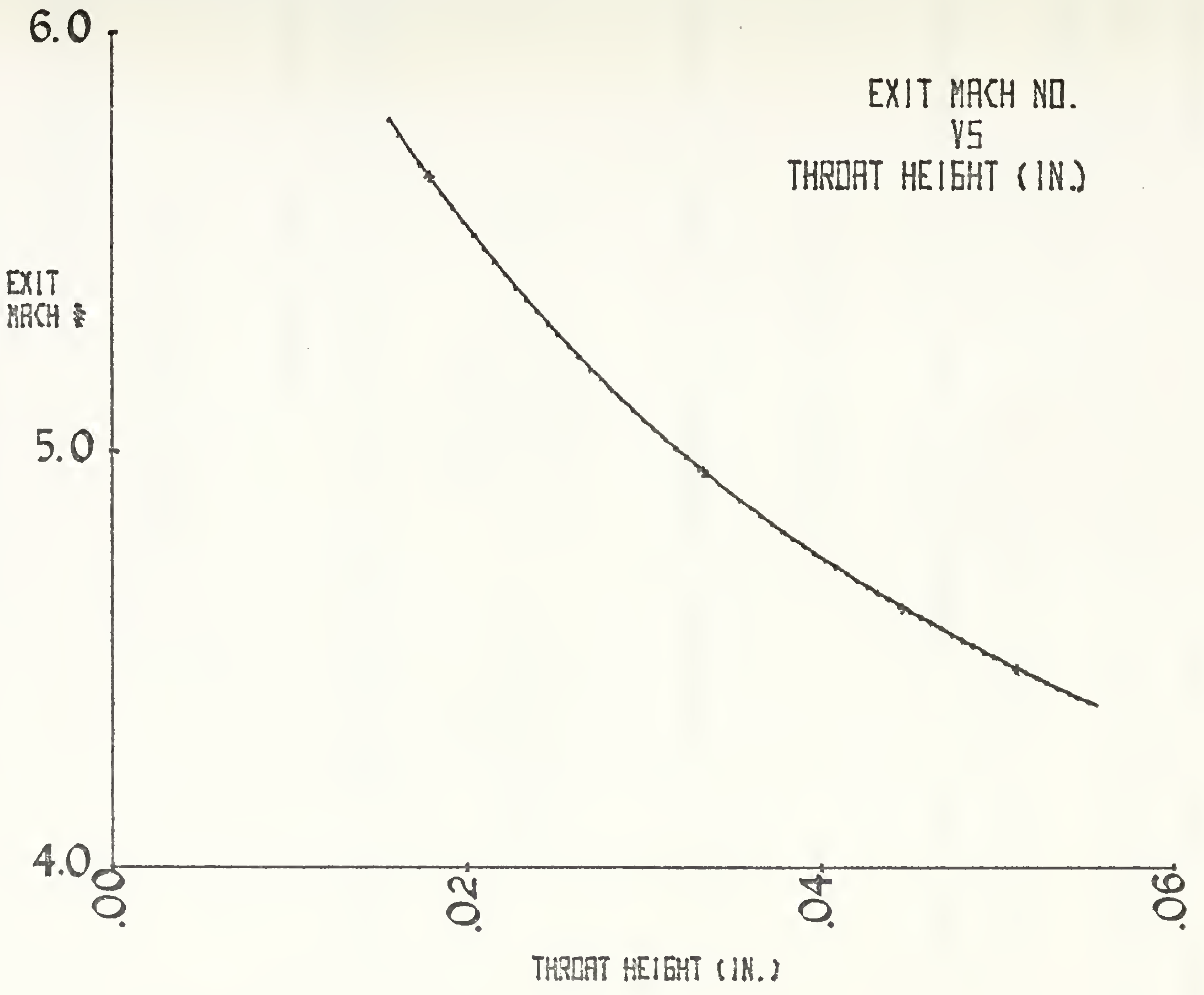

FIGURE (17) EXIT MACH NUMBER VS. THROAT HEIGHT

A throat height of .05 inches was chosen to allow for the lowest exit Mach number that would not result in a choked inlet condition. From figure (17), a throat height of .05 inches results in an exit Mach number of 4.5. The axisymmetric method of characteristics was used to design the contour of the nozzle rings. These calculations are found in section III-C.

Knowing the throat height between each nozzle ring, the mass flow rate can be determined. For each nozzle,

$$\dot{m}_{nozzle} = \rho^* U^* A^* \quad .$$

Using the equation of state and rearranging yields

$$\dot{m}_n = \left[\frac{P_o(\frac{P^*}{P_o})(49.1)}{R(T_o \frac{T^*}{T_o})^{\frac{1}{2}}}\right] \left[\frac{.2\pi(1)(105)}{144}\right] .$$

Substituting the appropriate values, the mass flow per nozzle is found to be

$$\dot{m}_n = 1.08 \text{ lb m/sec} \quad .$$

Total mass flow is

$$\dot{m}_{total} = 6\ (\dot{m}_n)$$

$$\dot{m}_{total} = 6.48 \text{ lb}_m/\text{sec} \quad .$$

2. Axial Variation of Mach Number and Static Pressure

After the flow enters the nozzle stack, changes in Mach number and static pressure occur in the axial direction. Shapiro [Ref. 4] develops influence coefficients that relate changes in one flow condition to changes in another. Assuming constant molecular weight, the change in Mach number is related to the area change by

$$\frac{dM^2}{M^2} = - \frac{2(1 + \frac{\gamma-1}{2} M^2)}{1-M^2} (\frac{dA}{A}) \quad . \qquad (6)$$

Appendix D shows the model used for the axial flow through the nozzle stack. The pressure change is also related to changes in area and is given by

$$\frac{dP}{P} = \frac{\gamma M^2}{1-M^2} \frac{dA}{A} \quad . \qquad (7)$$

Using the geometry of the nozzle stack, and rearranging equations (6) and (7), axial Mach number and pressure changes are found to be

$$M_{i+1} = M_i - M_i \left[\frac{1 + \frac{\gamma-1}{2} M_i^{\,2}}{1 - M_i^{\,2}} (.06667)\right] \qquad (8)$$

and

$$P_{i+1} = P_i + P_i \left[\frac{\gamma M_i^{\,2}}{1 - M_i^{\,2}} (.06667)\right] \quad . \qquad (9)$$

A computer program was written using equations (8) and (9) to determine values of Mach number and pressure in the axial direction. Figures (18) and (19) are the results of this program in graphical form. A listing of the program and the results are found in Appendix D, along with details of the preceding development.

3. Radial Variation of Pressure and Mach Number

As the flow leaves the nozzles, it experiences increasing area as it moves out radially. This area increase results in increasing Mach number and a corresponding decrease in static pressure.

From the nozzle ring geometry,

$$A/A^* = \frac{2\pi r(h+t)}{2\pi r_t h}$$

$$A/A^* = 11.0(r) \quad . \tag{10}$$

Assuming isentropic flow:

$$A/A^* = \frac{1}{M}\left[\frac{2}{\gamma+1}\left(1+\frac{\gamma-1}{2}M^2\right)\right]^{\frac{\gamma+1}{2(\gamma-1)}} \tag{11}$$

and

$$P_o/P = \left[\left(1+\frac{\gamma-1}{2}M^2\right)\right]^{\frac{\gamma}{\gamma-1}} \quad . \tag{12}$$

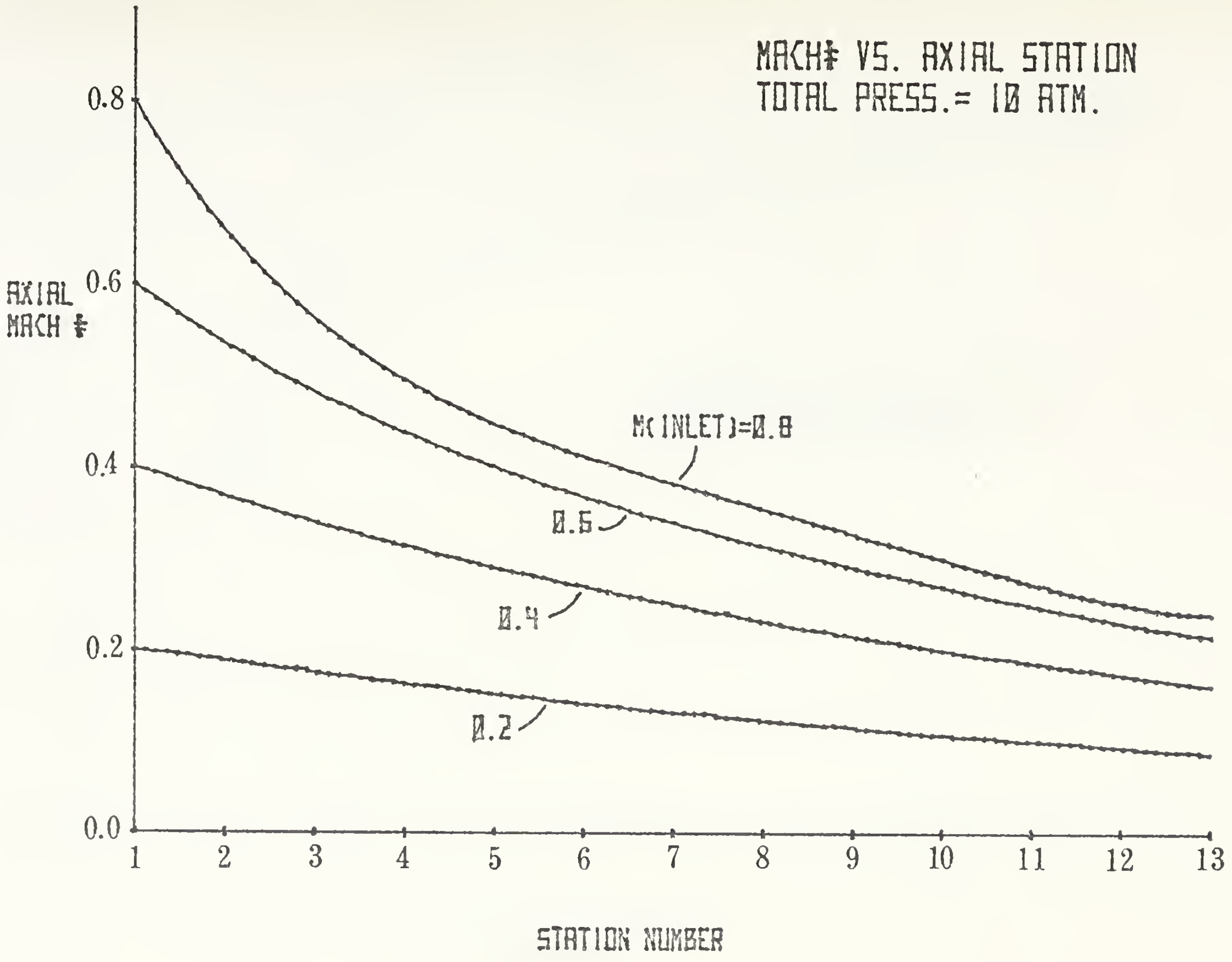

FIGURE (18) MACH NUMBER VS. AXIAL STATION

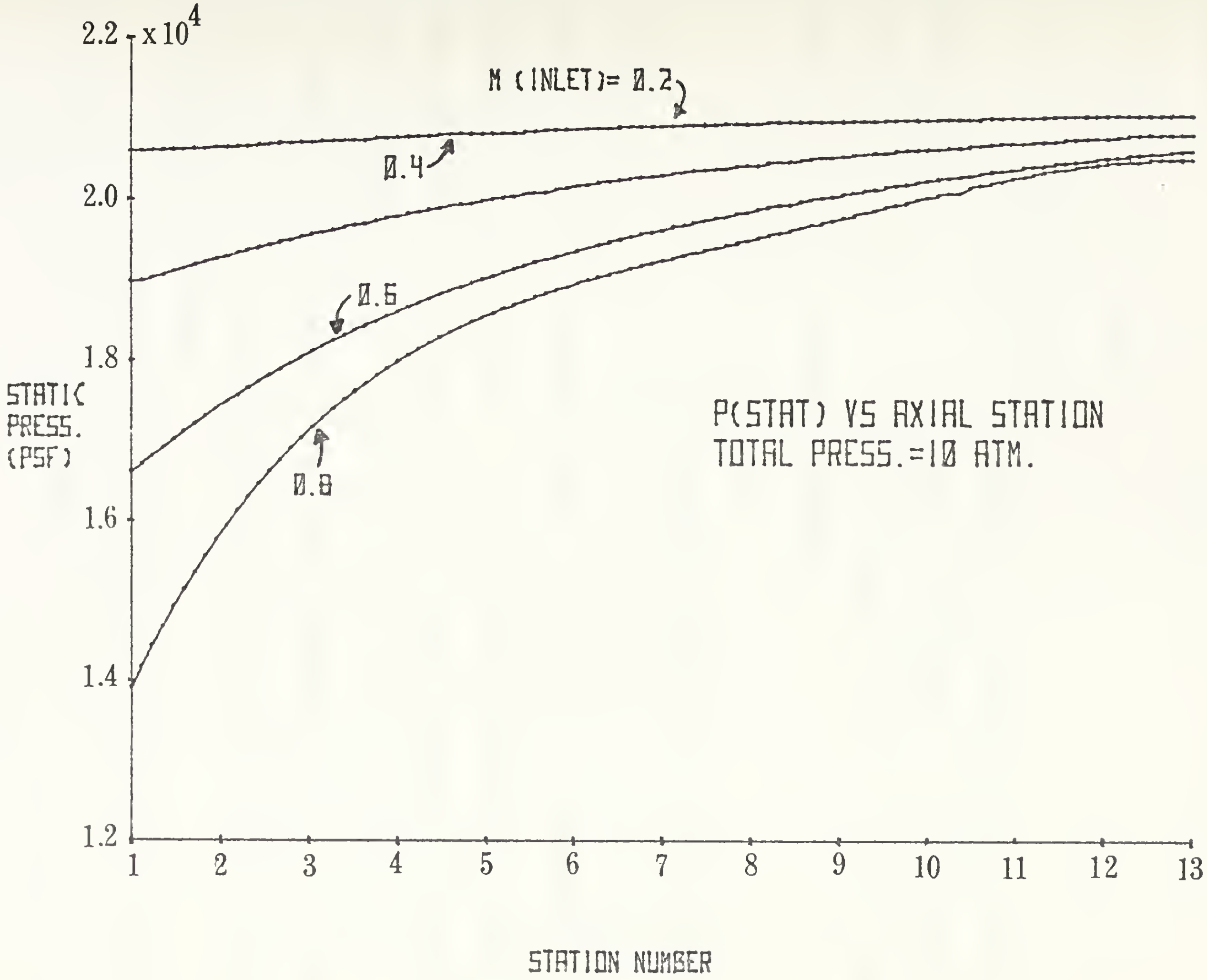

FIGURE (19) PRESSURE VS. AXIAL STATION

Equations (10), (11) and (12) relate Mach number and pressure to radial position. Table (2) is a summary of these three equations for different radii. Figures (20) and (21) are graphical representations of Mach number and pressure as functions of radius.

C. NOZZLE RING DESIGN

1. Nozzle Contour

As was shown previously in Section III-A, an exit Mach number of 4.5 was chosen for design. The curvature of the nozzle rings was determined by the use of the axisymmetric method of characteristics.

a. Initial Turning

In a two-dimensional nozzle the flow is turned through ($\nu_{final}/2$) degrees at the throat, where ν_{final} is the value of the Prandtl-Meyer function corresponding to the design exit Mach number. In a three-dimensional case the flow expands from throat to tip (and therefore the Mach number increases) due solely to the increase in area. Thus to achieve the desired exit Mach number in the three dimensional case, the flow should be turned less than in the two-dimensional case.

Assuming parallel plates, the ratio of the exit area to the throat area reduces to

$$A_e/A_{throat} = 1.5/1 \quad .$$

Table 2 Radial Variation of Mach Number and Pressure

r (in.)	M	P_{stat} (psf)
1.5	4.50	73.11
2.0	4.84	48.30
2.5	5.089	36.07
3.0	5.239	30.39
3.5	5.479	23.27
4.0	5.674	18.85
4.5	5.869	14.92

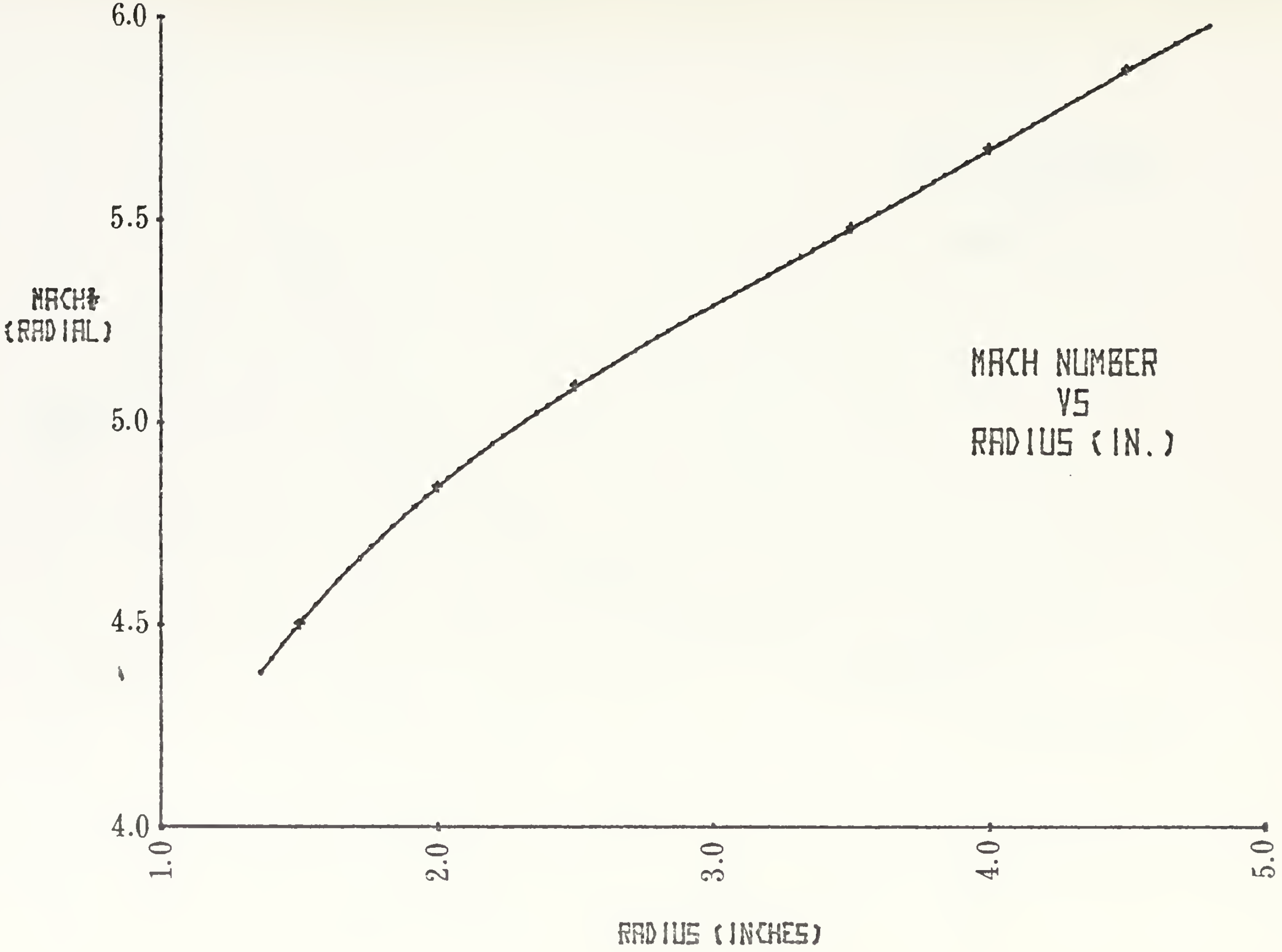

FIGURE (20) MACH NUMBER VS. RADIUS

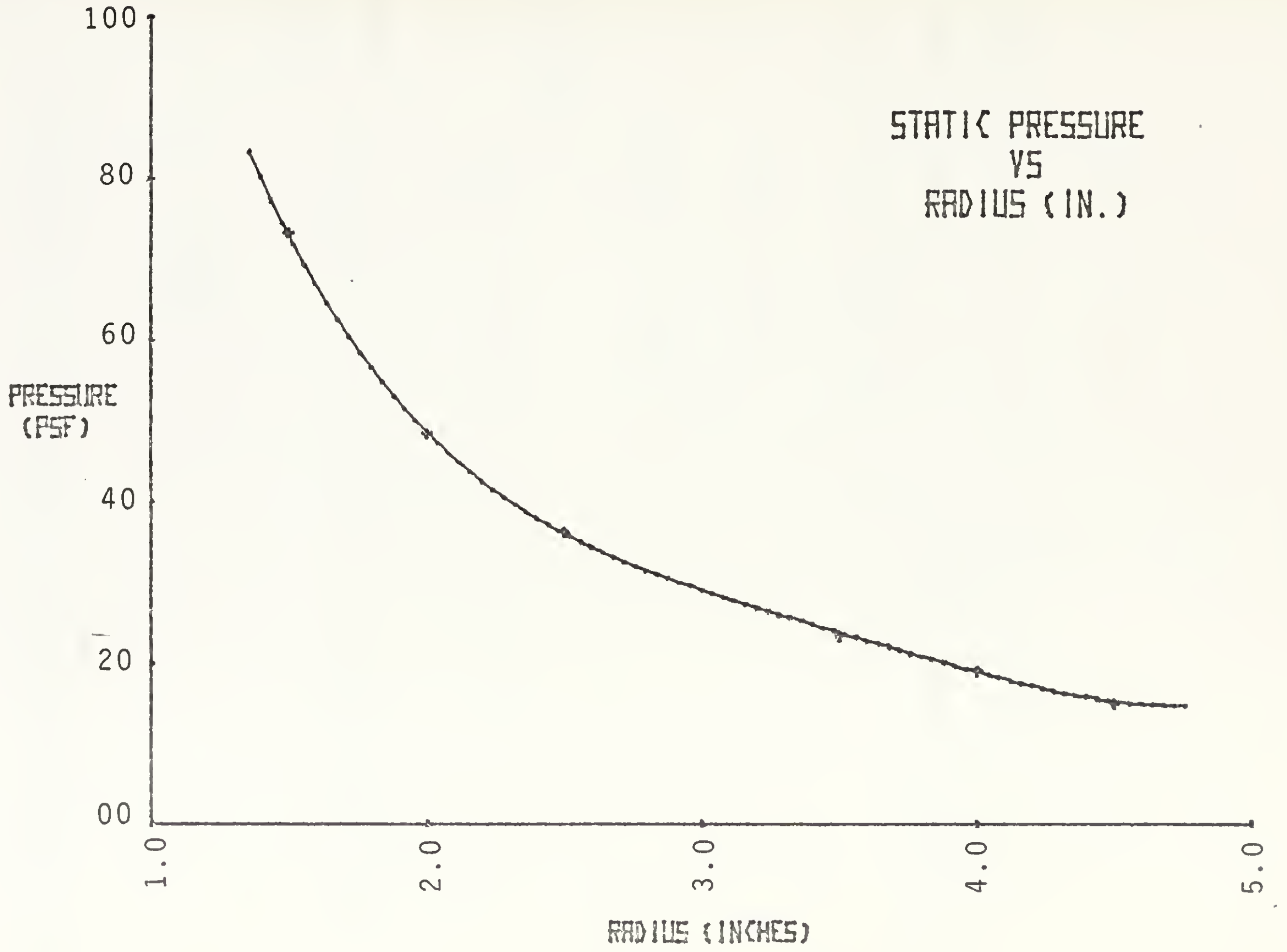

FIGURE (21) PRESSURE VS. RADIUS

Using a design Mach number corresponding to an area ratio of

$$A/A^* = (A/A^*)M = 4.5(1/1.5)$$

or

$$A/A^* = 10.4 \quad ,$$

and then treating the initial turning as if it were a two-dimensional case should give approximate results (that is, an exit Mach number near 4.5). For

$$A/A^* = 10.4 \ ,$$

$$M_{exit} = 3.96$$

which yields

$$\nu_{exit} = 65.3°$$

Therefore the initial turning of the flow at the throat should be

$$\Delta\theta = \frac{\nu_{exit}}{2} = 32.65°$$

where θ is measured from the flow direction entering the throat.

b. Axisymmetric Method of Characteristics

Liepmann and Roshko [Ref. 3] develop expressions for finding the Prandtl-Meyer function (ν) and the flow for direction (θ) for an axially symmetric flow and are given by

$$\nu_3 = \frac{1}{2}(\nu_1 + \nu_2) + \frac{1}{2}(\theta_1 - \theta_2) + \frac{1}{2}[\sin \mu_1 \frac{\sin \theta_1}{r_1} \Delta\xi_{13} + \sin \mu_2 \frac{\sin \theta_2}{r_2} \Delta\eta_{23}] \tag{13}$$

and

$$\theta_3 = \frac{1}{2}(\nu_1 - \nu_2) + \frac{1}{2}(\theta_1 + \theta_2) + \frac{1}{2}[\sin \mu_1 \frac{\sin \theta_1}{r_1} \Delta\xi_{13} - \sin \mu_2 \frac{\sin \theta_2}{r_2} \Delta\eta_{23}] \tag{14}$$

where all angles and subscripts are as shown in figure (22).

Using equations (13) and (14) the nonsimple core of the characteristic mesh was calculated. Figure (23) shows the entire characteristic mesh. The initial turning at the sharp-edged throat was divided into eight segments as figure (23) illustrates. Section II of Appendix E contains tables of Mach number, Mach angle, flow angle and Prandtl-Meyer function for each point in the mesh.

As the last of the right running characteristics from the throat reached the plane of symmetry (point 70), the Mach number was found to be 4.47, and the flow angle was

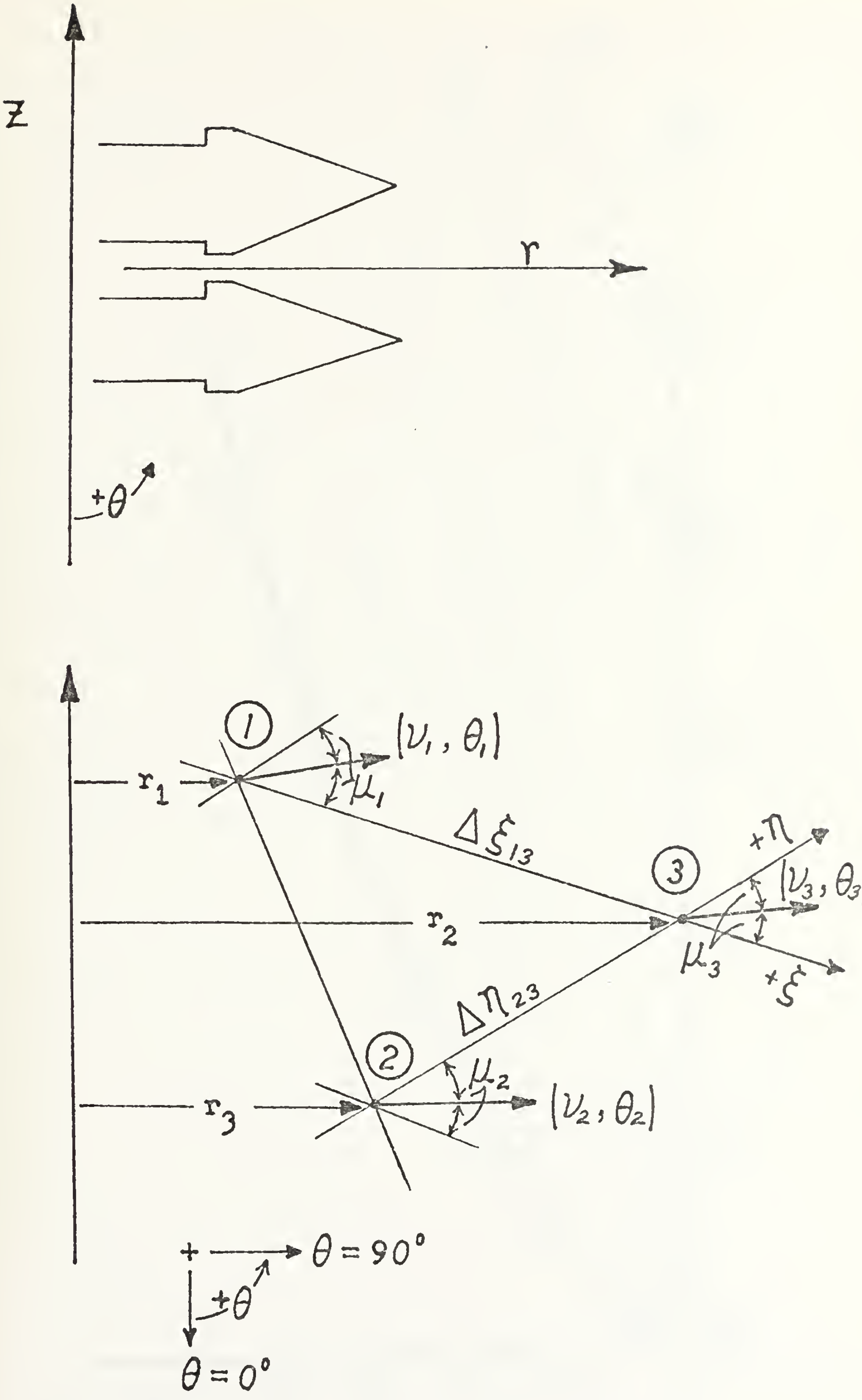
Z
r
+θ
①
(ν₁, θ₁)
r₁
μ₁
Δξ₁₃
③
+η
(ν₃, θ₃)
r₂
μ₃
+ξ
Δη₂₃
②
μ₂
(ν₂, θ₂)
r₃
+
θ = 90°
±θ
θ = 0°

FIGURE (22) CHARACTERISTIC ELEMENT

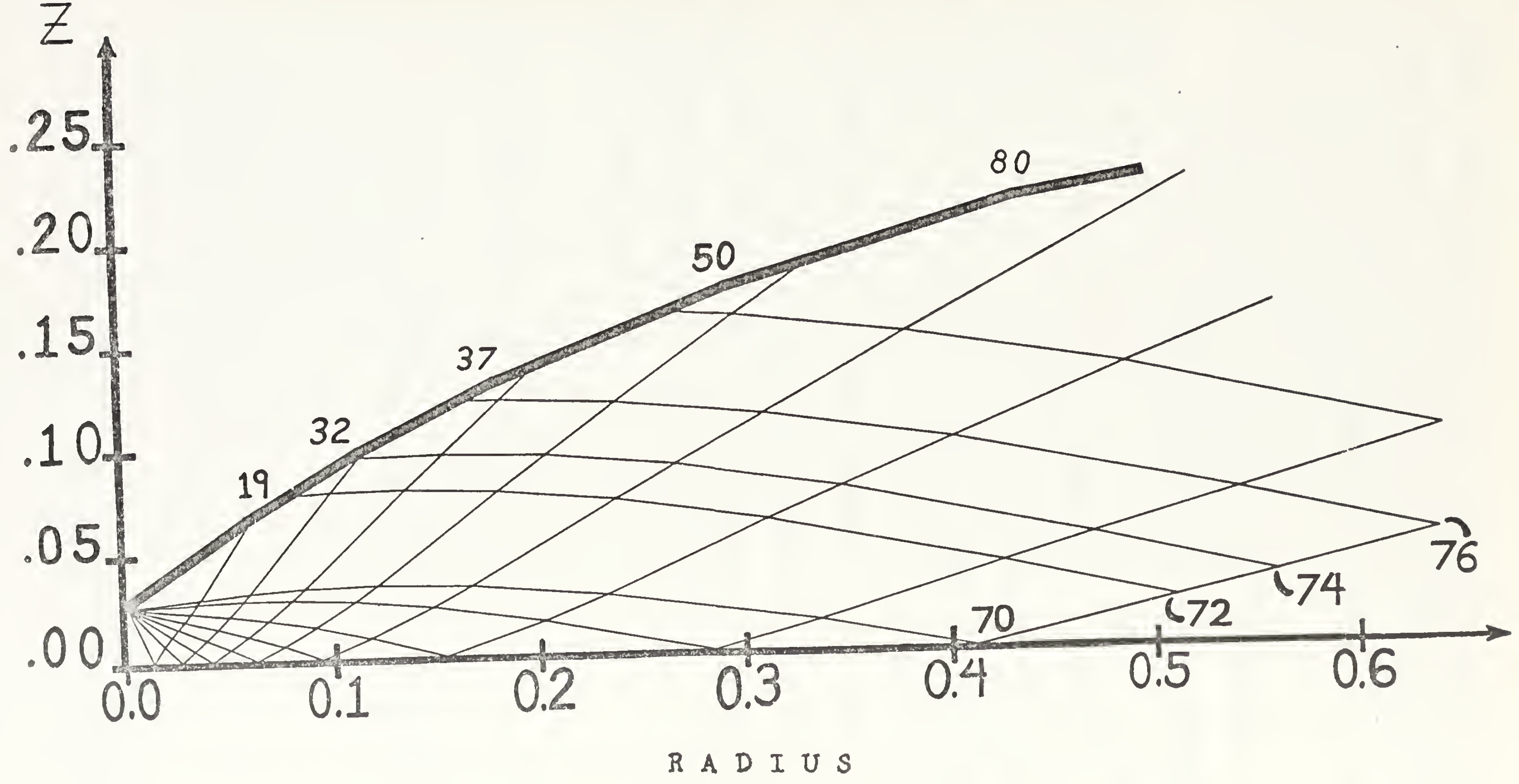

FIGURE (23) COMPLETE CHARACTERISTIC NETWORK

90°. These flow conditions show that by reducing the design Mach number by the method previously described, and then treating the initial turning as a two-dimensional case, accurate results will be obtained.

c. Establishing Points on the Nozzle Wall

The left running characteristic from point 70 is a straight line, and the flow conditions at any point on this characteristic will be the same as at point 70, that is, $M = 4.47$ and $\theta = 90°$. Points on the nozzle wall were determined by calculating points along a right running characteristics in the $-\xi$ direction starting from a point on the left running characteristic between points 70 and 76.

Following a development similar to Ref. 3, equations (13) and (14) were modified to calculate points of the characteristic mesh proceeding in the $-\xi$ direction. The modified equations are

$$\nu_3 = \frac{1}{2}(\nu_1 + \nu_2) + \frac{1}{2}(\theta_1 - \theta_2) + \frac{1}{2}\left[-\sin\mu_1 \frac{\sin\theta_1}{r_1}\Delta\xi_{13} + \sin\mu_2 \frac{\sin\theta_2}{r_2}\Delta\eta_{23}\right] \tag{15}$$

and

$$\theta_3 = \frac{1}{2}(\nu_1 - \nu_2) + \frac{1}{2}(\theta_1 + \theta_2) + \frac{1}{2}\left[-\sin\mu_1 \frac{\sin\theta_1}{r_1}\Delta\xi_{13} - \sin\mu_2 \frac{\sin\theta_2}{r_2}\Delta\eta_{23}\right] \tag{16}$$

where angles and subscripts are as shown in figure (E-1) found in Appendix E. Equations (15) and (16) were used to construct right running characteristics in the $-\xi$ direction from points 72, 74, 76 and 78 (not shown) until the left running characteristics reflected from the centerline were met. Starting at the throat the wall was drawn at 32.65° (relative to the centerline) until point 19 was reached, where the wall angle was reduced to the flow angle that was calculated for point 19. This procedure was continued for points 32, 37 and 50. The last point (point 80) was the result of changing the angle of the wall to the estimated flow angle at that point. This line was extended until a radius of 1.5 inches was reached. Limiting the exit radius to this value was an effort to keep the exit Mach number as low as possible as was discussed previously.

d. Wall Shape

The r and z coordinates of the points where the wall slope changes, as well as the throat and the exit points, were fit with a fourth-degree polynomial using the Hewlett Packard model 9830-A computer and a polynomial regression program. The coordinates of the points and the coefficients of the fourth-degree polynomial are shown in Table (3). Figure (24) shows the nozzle contour from throat to exit.

2. Trailing Edge

As can be seen from figure (24), the nozzle contour is not tangent to the ring centerline at r = 1.5 inches.

Table 3 Description of Wall Contour

A. Wall Point Coordinates from Method of Characteristics

Point Number	X Coord.	Y Coord.
(throat)	1.00	.025
19	1.06	.066
32	1.11	.097
37	1.18	.138
50	1.29	.173
80	1.44	.215
(exit)	1.50	.226

B. Coefficients of Fourth Degree Polynomial Fit to Points

B(0) = -6.375

B(1) = 18.144

B(2) =-19.773

B(3) = 9.939

B(4) = -1.910

R-Square = 0.99997

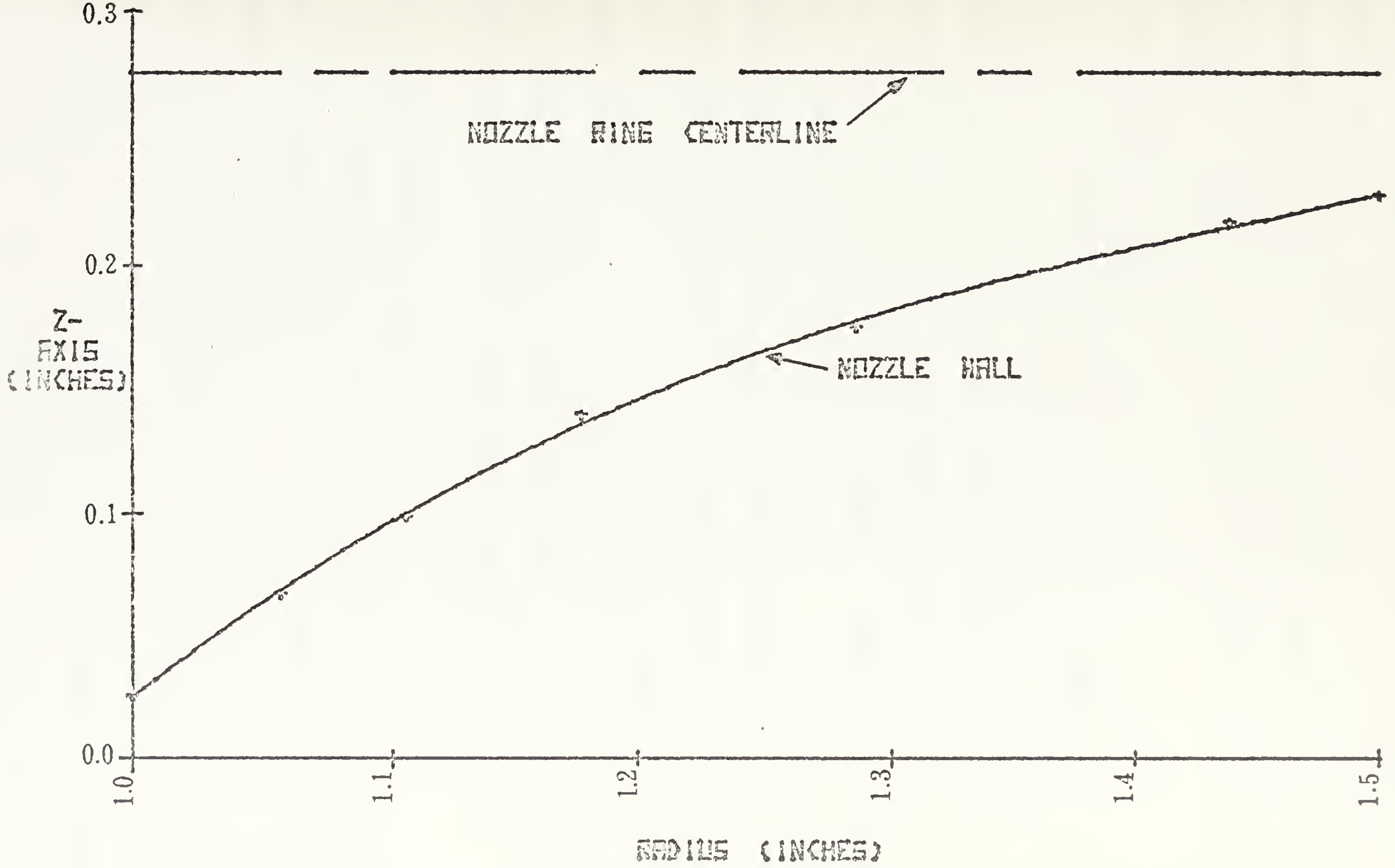

FIGURE (24) NOZZLE WALL CONTOUR: FOURTH DEGREE POLYNOMIAL FIT TO CALCULATED WALL POINTS

Rather than change the shape of the wall to a contour that would result in a sharp trailing edge, it was decided to maintain the design contour. This resulted in the flow exiting the nozzle at a 5° angle and a blunt trailing edge as shown in figure (25).

3. Throat Shape

A sharp-edged throat was used to obtain the highest degree of turning for the shortest length. Reference 5 states that to be assured of uniform flow at the nozzle entrance, the radius of curvature of the inlet should be two to three times the throat height. Figure (26) shows the details of the nozzle inlet and throat. Due to the original geometry of the nozzle ring (before machining) the ratio of the radius of curvature to the throat height was limited to between 1.5 and 2.0. The shaded area in figure (26) represents the machining tolerance of the inlet contour. The center of curvature was displaced to the left of the sharp corner to assure horizontal tangency of the flow.

D. EJECTOR NOZZLE DESIGN

For a reservoir stagnation pressure of ten atmospheres and Mach-five flow, the total pressure downstream of the normal shock will be less than one atmosphere. To lower the back pressure and thus allow the cylindrical nozzles to start, ejector nozzles were designed and installed in the exhaust section of the apparatus as illustrated in figure (7). Using the continuity, momentum and energy equations,

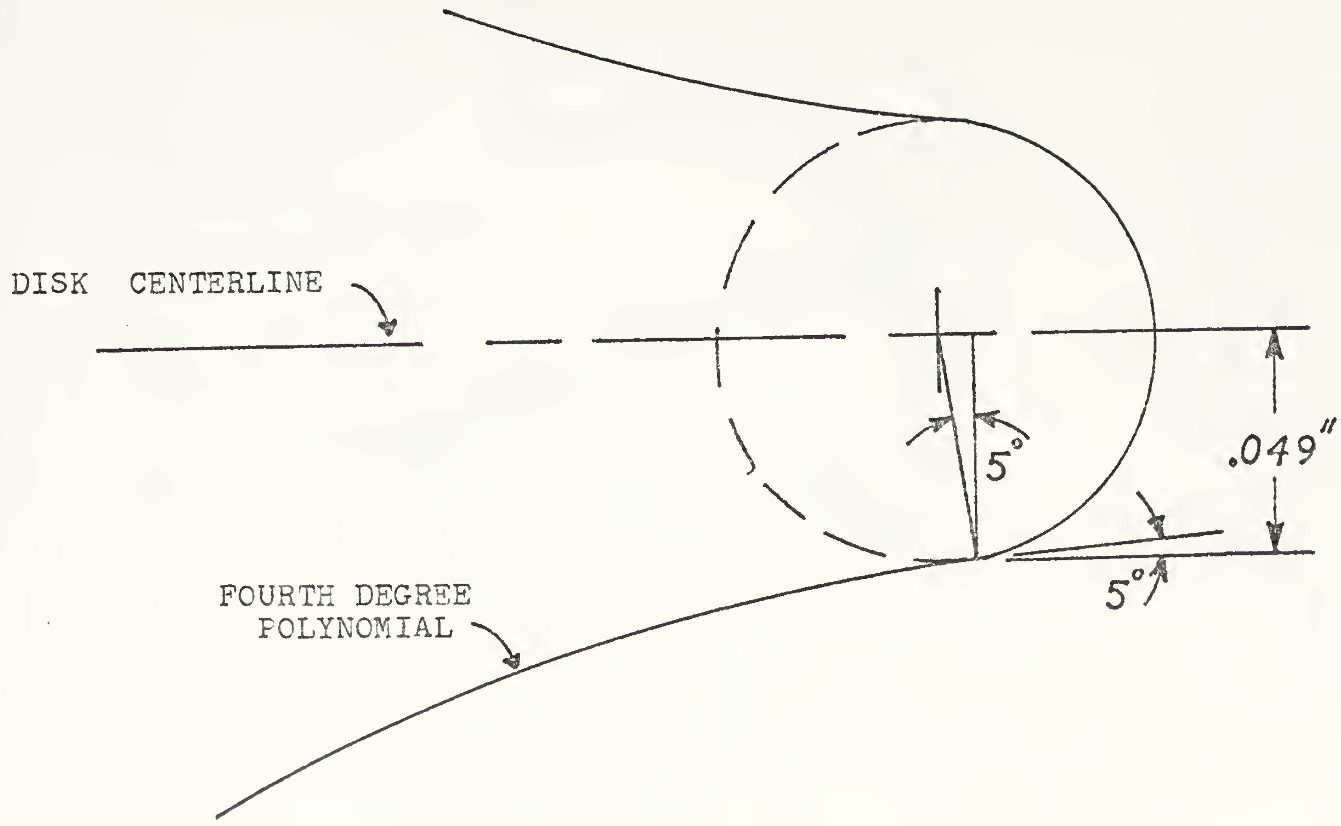
DISK CENTERLINE
.049"
5°
5°
FOURTH DEGREE POLYNOMIAL

FIGURE (25) DETAIL OF NOZZLE RING TRAILING EDGE

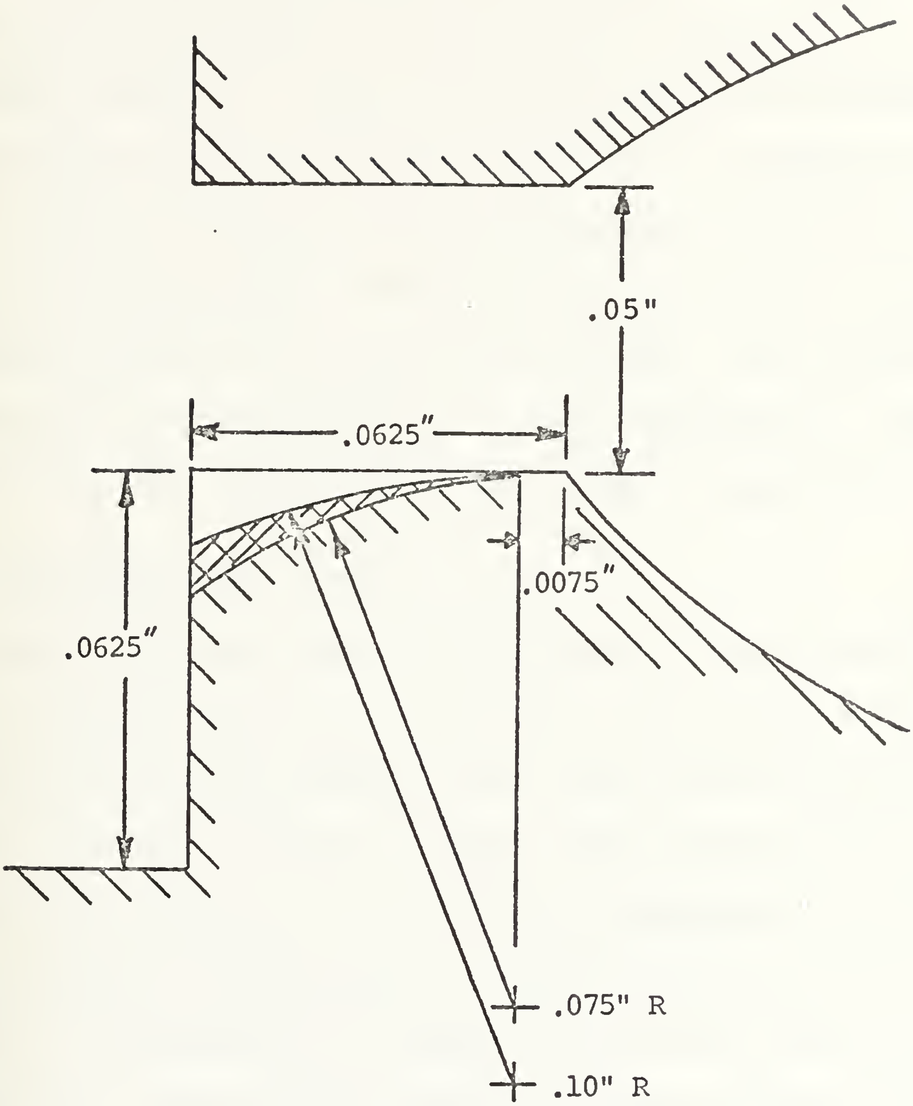
.05"
.0625"
.0625"
.0075"
.075" R
.10" R

FIGURE (26) DETAIL OF NOZZLE RING THROAT

solutions to the flow were found for different combinations of exhaust area and ejector nozzle diameter. A computer program was written to solve the three equations, and the results are tabulated in Appendix F. Figure (27) is a graph of these results. Any combination of nozzle diameter (D1) and exhaust width (D3) which results in a chamber pressure (P1) below the total pressure line will allow the cylindrical nozzles to start. A nozzle diameter of 1.75 inches and exhaust width of 6.5 inches were chosen. This combination results in a back pressure of .562 atmospheres. Complete details of this development are found in Appendix F.

E. BOUNDARY LAYER BLEED

Boundary layer bleed was employed to keep the flow from separating at the shock location. By bleeding off the low energy air in the boundary layer the remaining flow will have sufficient energy to support the pressure rise associated with a shock of the strength anticipated. A search of the literature relating to boundary layer failed to locate specific information on supersonic boundary layer bleed techniques, specifically, hole size and pressure ratio required to remove a certain fraction of the boundary layer. Since information could not be found, a model was developed to make such a prediction.

1. Flow Model

A model fluid discussed by Stewartson [Ref. 7] was used in this development. The fluid is assumed to have a Prandtl number of unity and the viscosity is proportional to

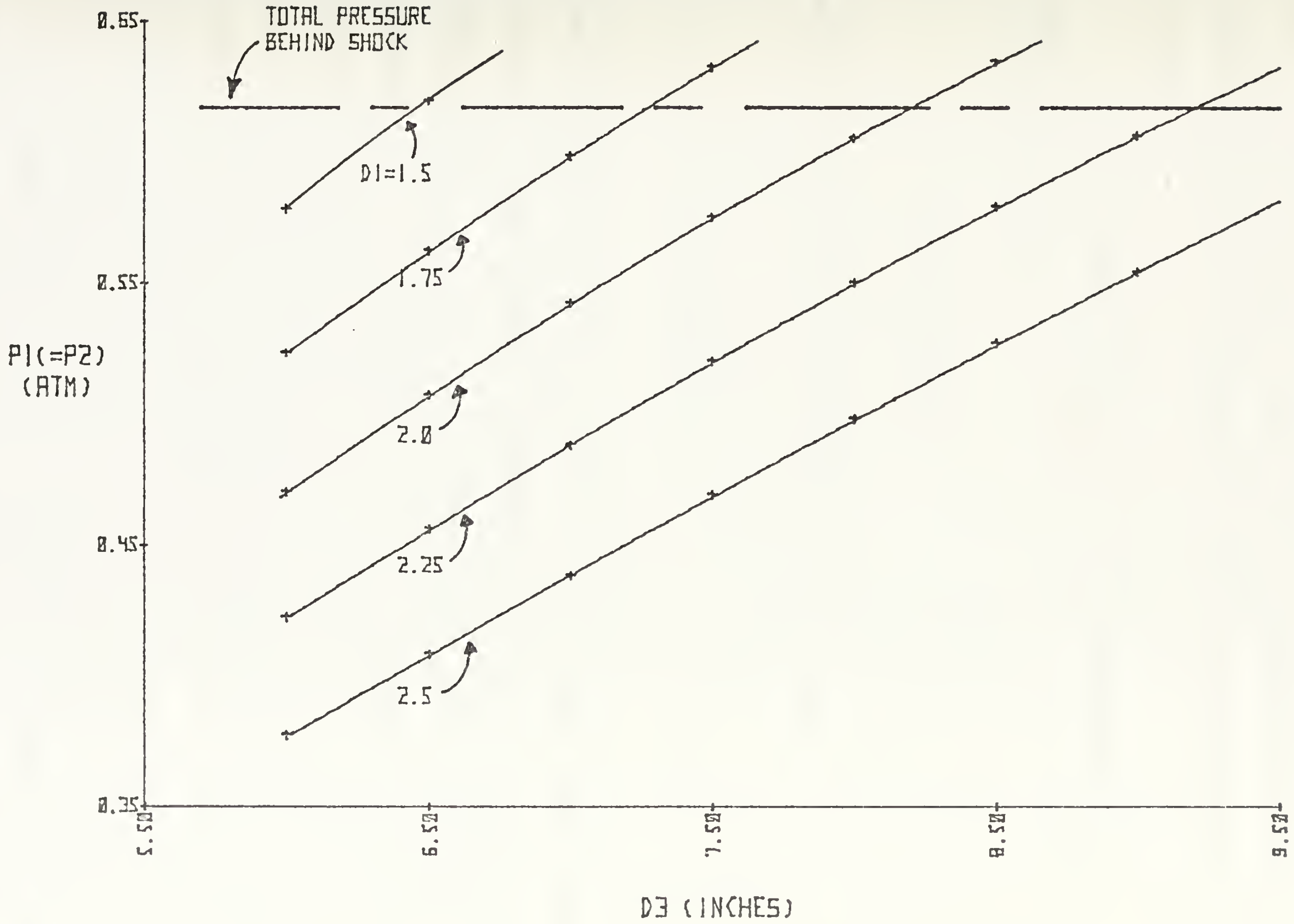

FIGURE (27) BACK PRESSURE VS. EXHAUST WIDTH WITH EJECTOR NOZZLE DIAMETER AS A PARAMETER

the static temperature so that $\mu\rho = \mu_1\rho_1$, where subscript 1 denotes the reference condition. Assuming the fluid has a Blasius profile and that stagnation temperature is constant through the boundary layer, the incompressible profile was transformed to a compressible profile by the method described in Ref. 7.

For analytical ease, a Blasius profile was approximated by

$$u/U = \sin(A\eta)$$

where A = 54° and η is given by Ref. 7 as

$$\eta = X\sqrt{2/R_e} \quad .$$

The reference length is denoted by X. The model shown in figure (28) was used to describe the flow. By applying a bleed plenum pressure (P_2) lower than the freestream pressure (P_1), a streamline (4) is assumed to stagnate on the downstream edge of a slot of width H. All flow below this streamline goes through the slot, which is assumed long enough to have parallel streamlines at the slot exit. By assuming isentropic flow in each streamtube below (4), it is possible to calculate flow conditions at the slot exit by specifying (P_1/P_2). Using the continuity equation leads to a slot width, H. The complete set of equations

programmed for the Hewlett Packard model 9830 computer, and is listed in Appendix G.

2. Results of Calculation

Figure (29) illustrates the results of the computer program and plots the fraction of the boundary layer that enters the slot (Y/δ) as a function of the pressure ratio (P_1/P_2), with nondimensional slot width H/δ as a parameter. Table (4) gives the results for the flow conditions anticipated for radial flow at a Mach number of 4.5. The symbols used are shown in figure (28) or have been given previously with the exception of a_{o_e}, which is the stagnation speed of sound at the edge of the boundary layer.

The dot-dash-dot line in figure (29) represents the locus of maximum Y/δ for a given slot width and pressure ratio.

3. Bleed Hole Design

Using the values from table (4), (specifically H and X) the total bleed area was found to be

$$A_{bleed} = 2\pi(r_e + X)H$$

$$= 2\pi(1.5 + 3)(.00143)$$

$$A_{bleed} = .38 \text{ in}^2 \quad .$$

Three hundred holes were drilled through each plate at a diameter of .141 inches as shown in figures (30) and (31).

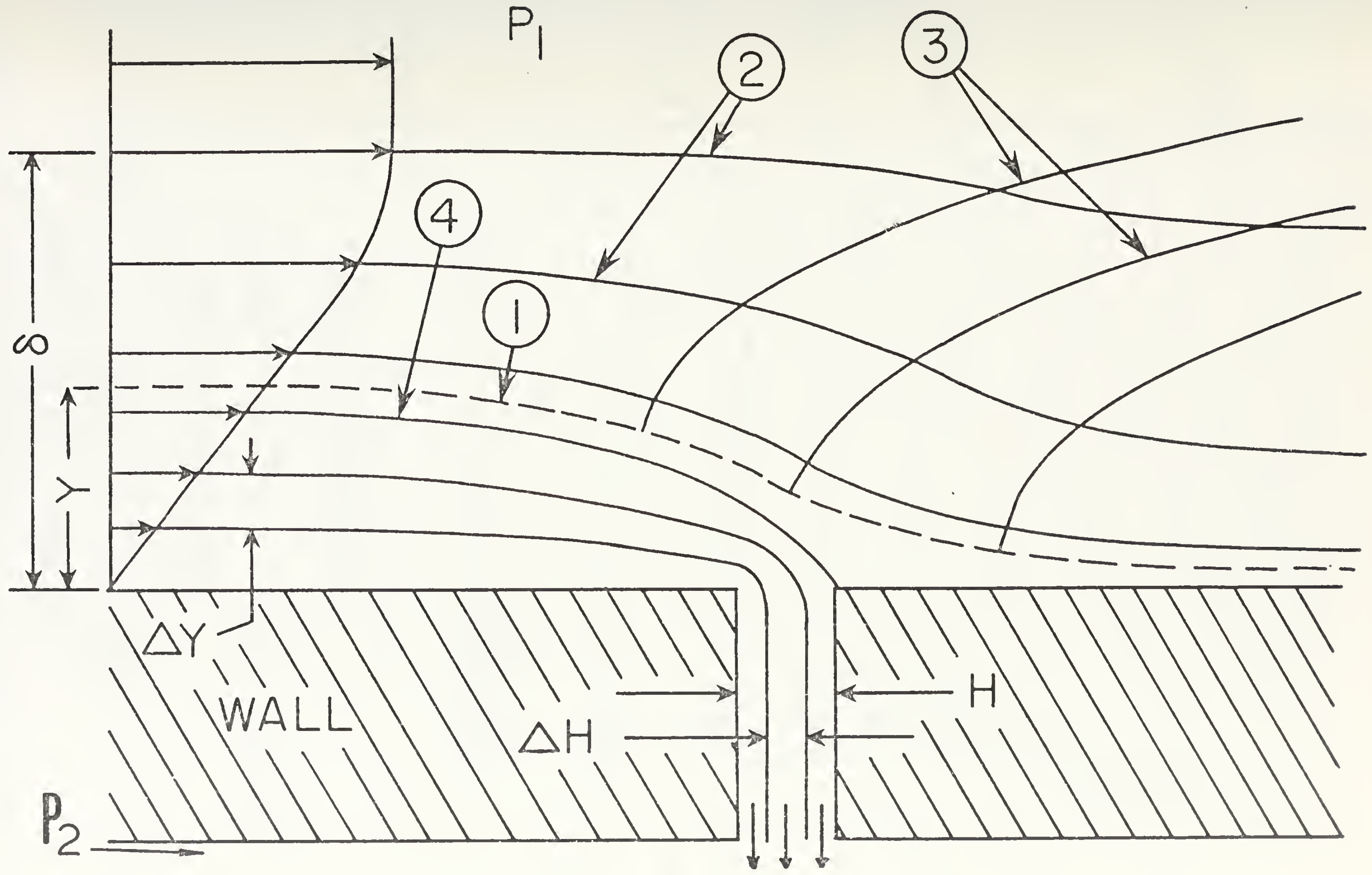
P1
⓶
⓷
⓸
⓵
δ
Y
ΔY
WALL
ΔH
H
P2

FIGURE (28) FLOW GEOMETRY FOR BLEED OF A HYPERSONIC OR SUPERSONIC BOUNDARY LAYER (FROM REF. 8)
(1) Sonic line
(2) Streamlines
(3) Mach lines
(4) Dividing streamline which stagnates on the donstream slot edge

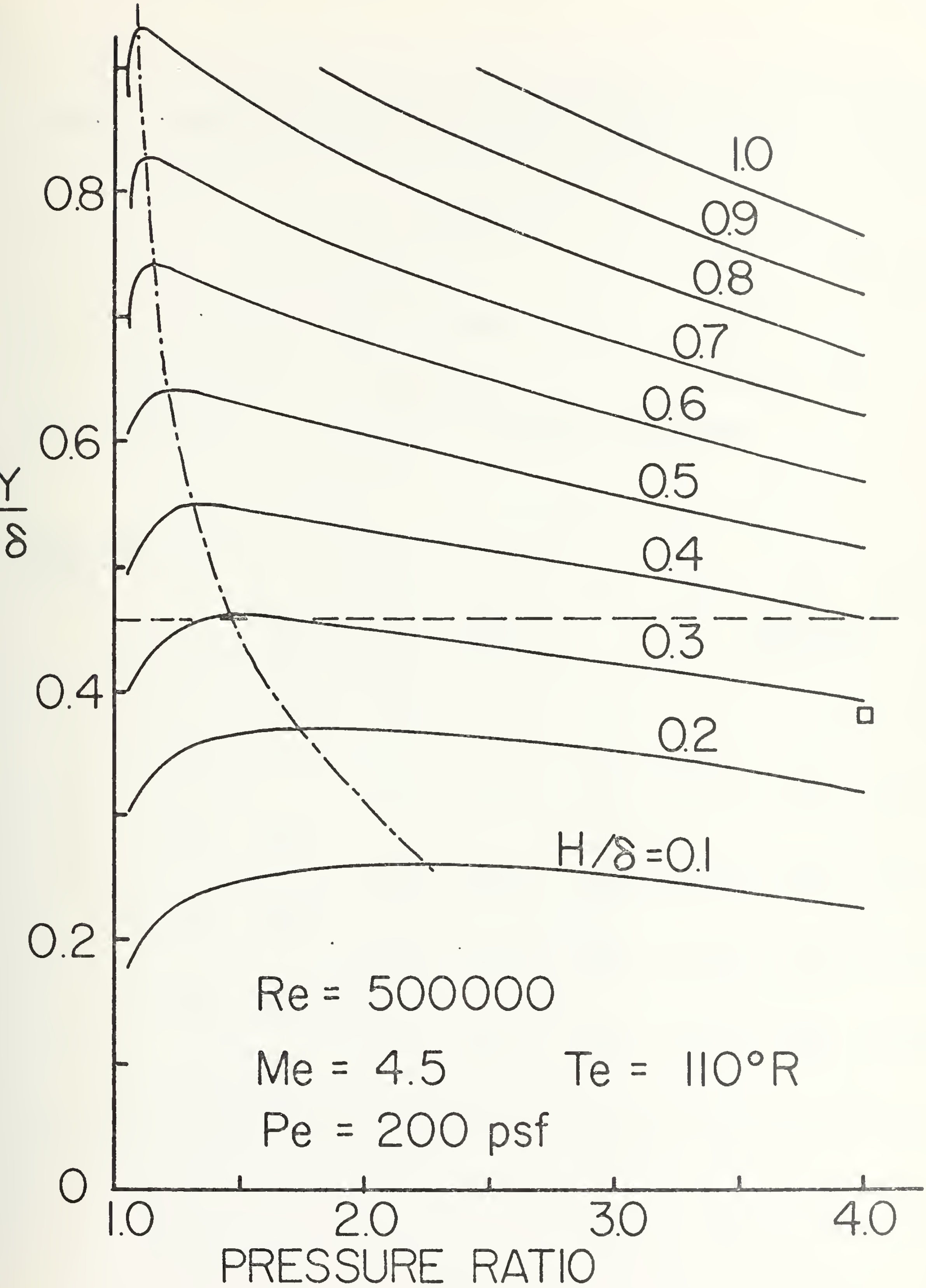

FIGURE (29) PLOT OF FRACTION BOUNDARY LAYER BLEED, Y/δ, AS A FUNCTION OF PRESSURE RATIO AND NON-DIMENSIONAL BLEED SLOT WIDTH (FROM REF. 8)

Table 4 Flow Conditions for Boundary Layer Bleed (from Ref. 8)

$M = 4.5$

$R_e = 500{,}000$

$x = 0.25$ ft

$\gamma = 1.4$

$A = 54°$

$a_{o_e} = 1157$ ft/sec

$U_e = 2318$ ft/sec

$p_1 = 200$ psf

$p_2 = 50$ psf

$\delta = 0.00504$ ft

$Y/\delta = 0.385$

$H/\delta = 0.283$

$H = .00143$ ft

$\dot{m}_{total} = 1.82$ E-4 slugs/sec

STREAMTUBE NUMBER	η	Y E-3 ft	ΔY E-4 ft	ΔH E-5 ft	M	M_E	$\dot{m}$ E-5 slugs/sec	$\Delta H/\Delta Y$
	0	0						
1			.40	.60	.076	1.56	0.74	0.15
	.16	.40						
2			.40	1.88	.227	1.58	2.21	0.47
	.32	.80						
3			.39	3.01	.381	1.63	3.67	0.77
	.48	1.19						
4			.38	3.98	.537	1.69	5.10	1.04
	.64	1.58						
5			.37	4.75	.698	1.78	6.51	1.28
	.80	1.95						

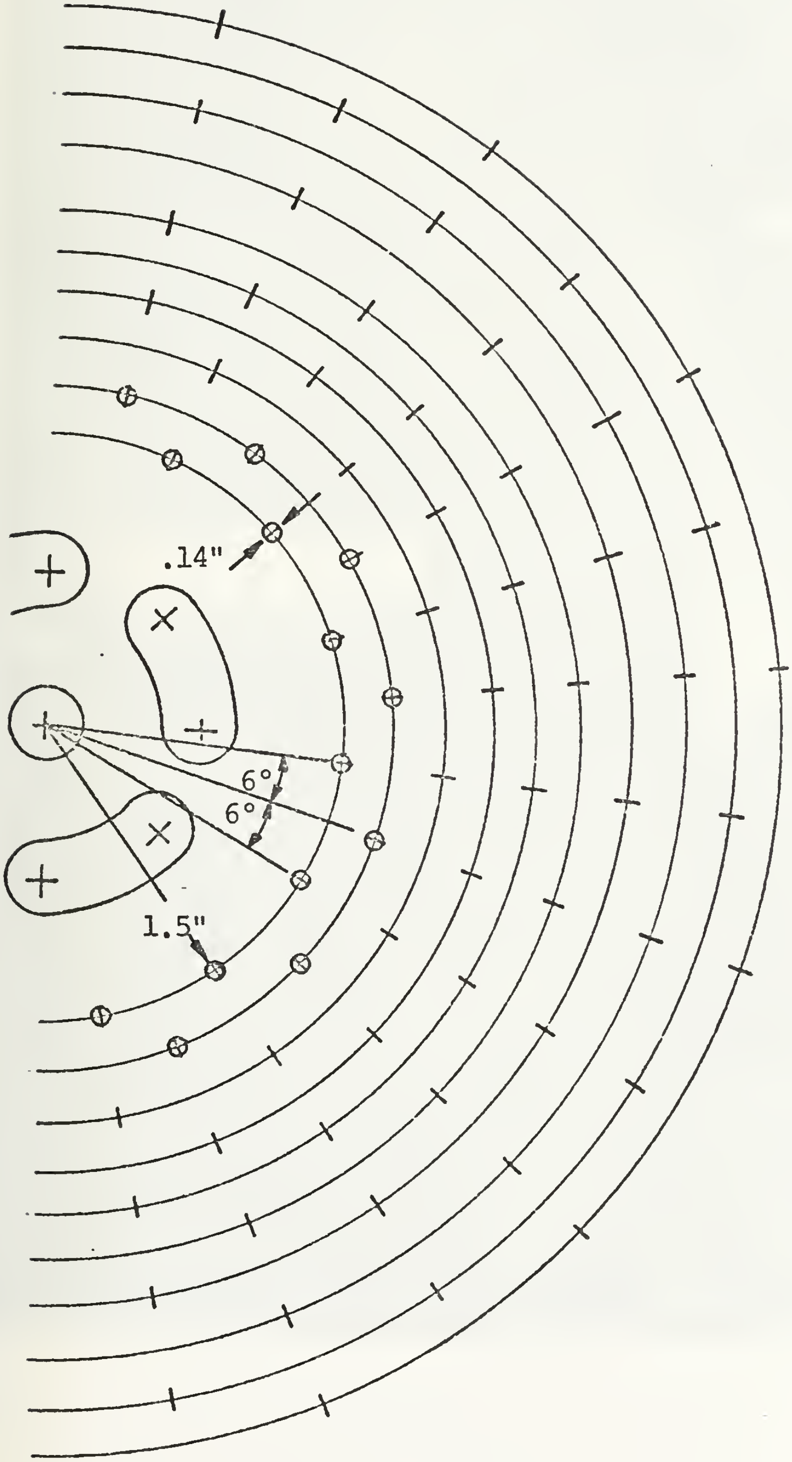

ALL ROWS ARE
1/4" APART

FIGURE (30) BLEED HOLE DESIGN

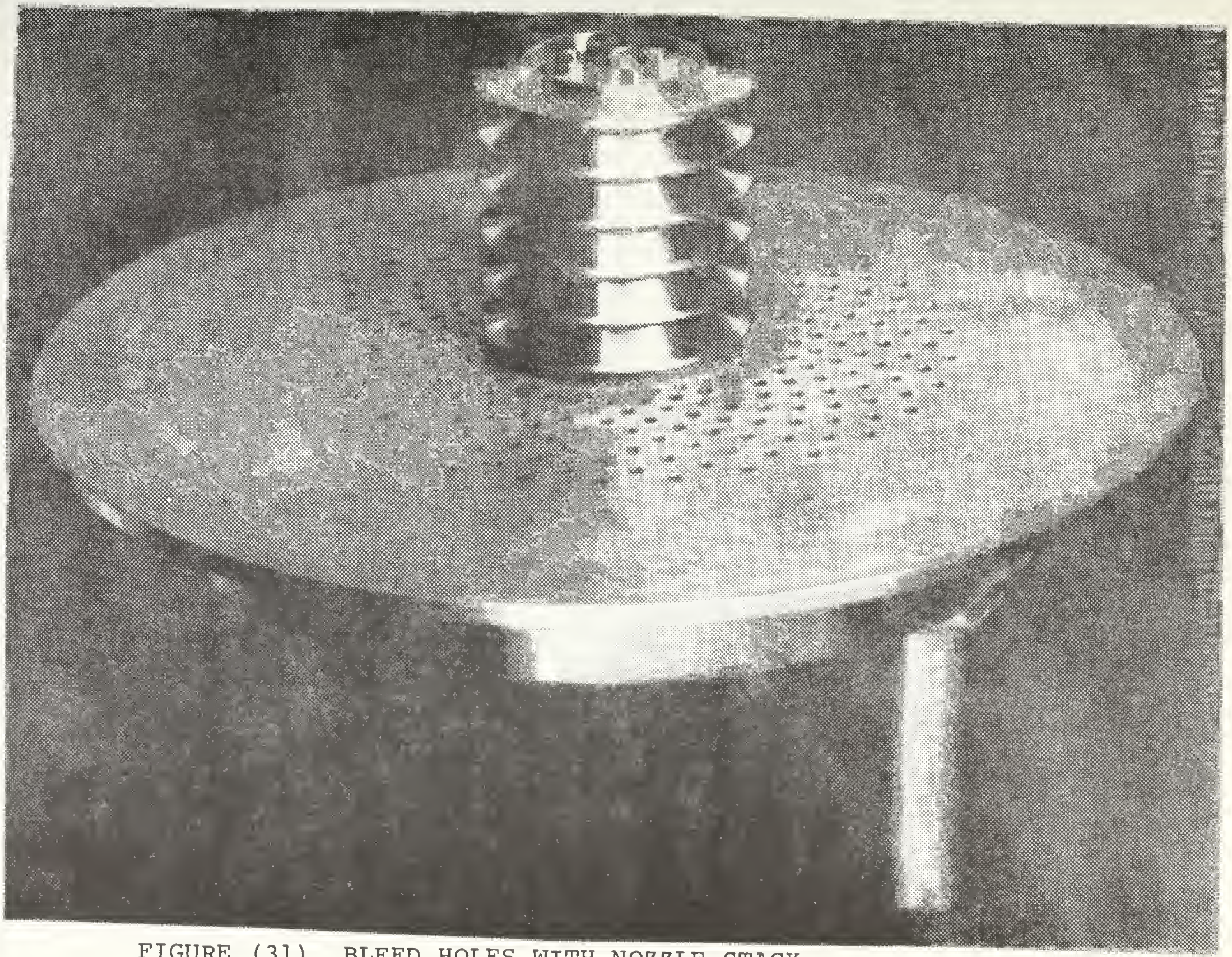

FIGURE (31) BLEED HOLES WITH NOZZLE STACK

The total area of the holes on one plate is larger than the calculated bleed area. This was done for three reasons:

1) to bleed off a greater fraction of the boundary layer than calculated if needed (see figure (29)),
2) to keep the same bleed area but vary the radial position of the effective bleed area (i.e., if bleed was desired at an inner radius, the outer holes were covered, or vice versa.),
3) since the bleed plenum was fitted with pressure taps, flow velocities could be attained by securing the suction to the plenum and recording the pressure drop in the plenum due to the flow over the bleed holes. By covering all but one row of holes the velocity at a desired radius could be obtained by using the isentropic relation for pressure and Mach number or Bernoulli's equation.

F. EXPERIMENTAL PROCEDURE

Initially six nozzle rings were tested in the apparatus illustrated in figure (7). Stagnation pressure applied to the nozzle stack, controlled by means of a regulator valve, was increased to a maximum of 130 pounds per square inch. Boundary layer bleed was attained by connecting the vacuum pump directly to the bleed plenums. The flow was observed using shadowgraph and Schlieren techniques. A typical run consisted of establishing the sensitivity of the Schlieren

(or shadowgraph) system to the desired level, starting the vacuum pump and allowing it to reach its lowest pressure, and then increasing the pressure to designated levels where photographs were taken.

The number of nozzles was then changed from six to four and the spacing of the nozzle rings (the throat height) was increased from .05 inches to .09 inches. This change decreased the exit Mach number from 4.5 to 3.9. Since the total pressure loss across the shock was less, the back pressure did not need to be lowered to below atmospheric. Therefore the ejector nozzles were removed. Removing the ejectors allowed for longer runs at high pressures due to a decrease of approximately forty percent in the mass flow from the reservoir.

The four nozzle rings were tested in the apparatus modified as shown in figure (32) in a fashion similar to that previously described for six nozzles. One important difference was the use of a 200 cubic foot tank to increase the bleed capability of the vacuum pump. The pump was connected to the tank and was able to lower the pressure inside it to approximately one-half pound per square inch. The bleed plenums were then connected to the bleed tank and the suction was controlled with a gate valve.

Flow conditions were observed and photographed at pressures up to the maximum attainable pressure of 250 pounds per square inch. Photographs were taken with and without

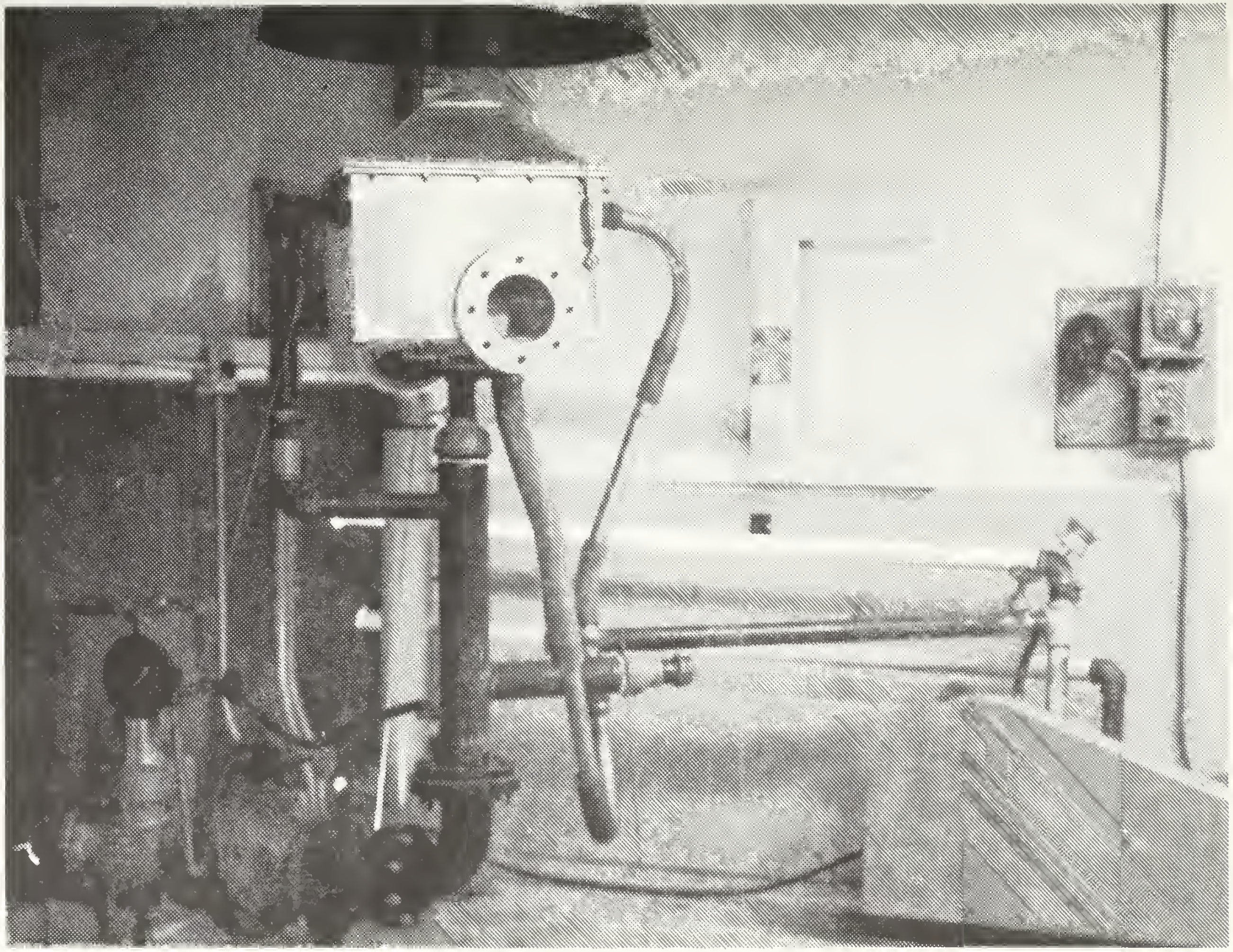

FIGURE (32) PHOTOGRAPH OF EXPERIMENTAL APPARATUS

boundary layer bleed to compare the resulting flow fields. The bleed hole pattern was also altered to obtain pressures in the bleed plenum due to the velocity of the flow across the holes at various radii as discussed in Section III-E. A pointed probe was inserted into the flow at various locations and different total pressures to determine regions of subsonic and supersonic flow.

IV. RESULTS AND CONCLUSIONS

A. RESULTS

As was previously mentioned, six nozzle rings were initially installed in the test apparatus shown in figure (32). Normal shocks were obtained in all except the end nozzles, but attempts at moving the shocks beyond the nozzle exit to form a "barrel" shock were unsuccessful at pressures of up to 130 psi.* Figures (33)(a) and (b) are Schlieren photographs of the six nozzles at pressures of 70 and 130 psi, respectively. Before attempting higher pressures it was decided to increase the throat area in order to lower the exit Mach number and thus make it easier to move the shocks out of the nozzles. Since the sum of the throat areas must remain smaller than the feed area to prevent choking at the ends of the stack, the number of nozzle rings was reduced to four and the throat height increased to .09 inches. This resulted in an exit Mach number of 3.9 and increased the Mach number at the feed holes to .9.

Three distinct flow patterns were observed in the flow over the range of pressures up to a maximum of 250 psi. Figures (34), (35) and (38) are Schlieren photographs showing the development of the first stage flow structure. Figure (37) is a schematic of the flow just prior to its

---

*Applied pressures are gage pressures unless otherwise specified.

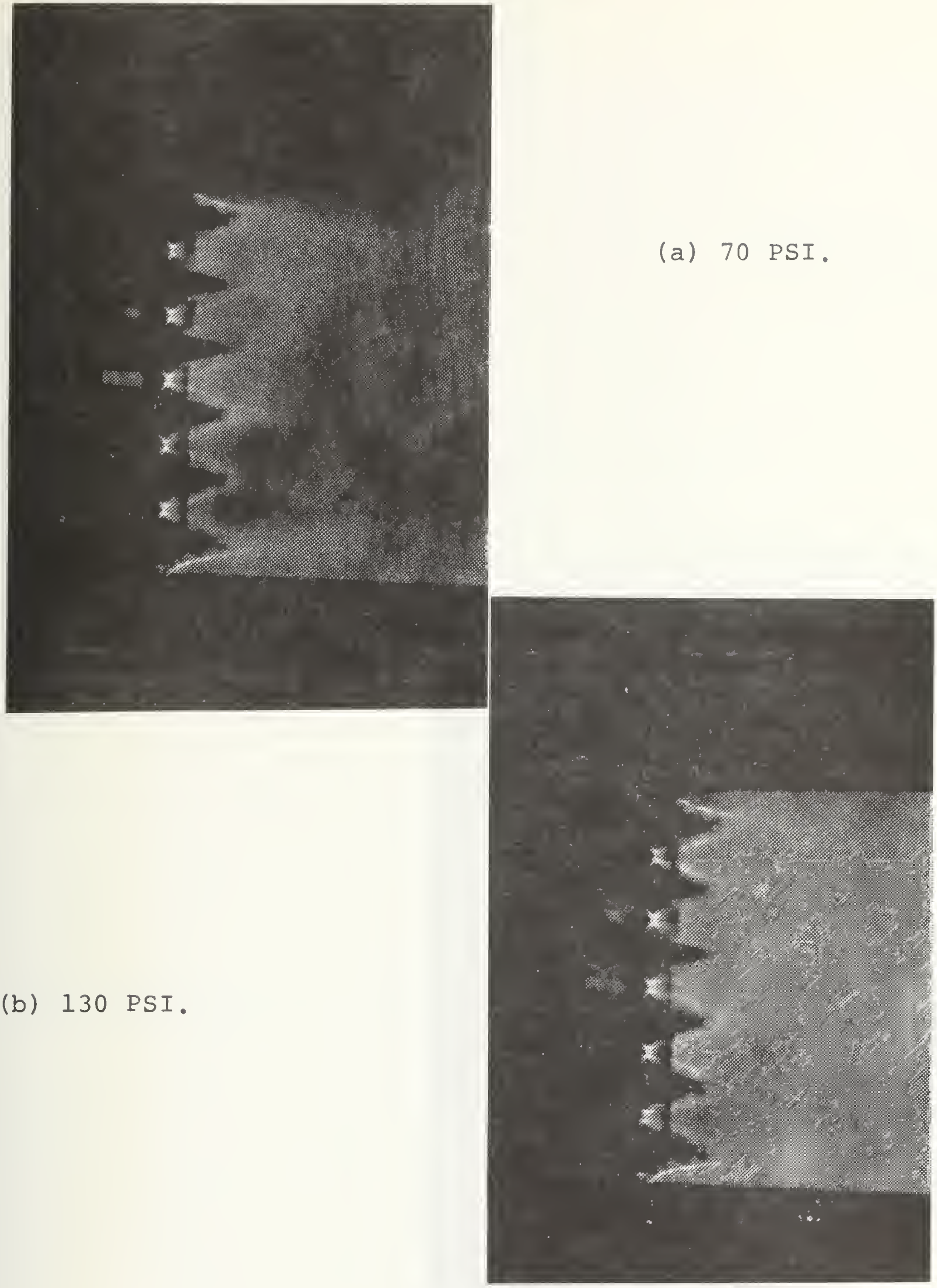

(a) 70 PSI.

(b) 130 PSI.

FIGURE (33) SCHLIEREN PHOTOGRAPHS OF NORMAL SHOCKS STANDING IN SIX NOZZLES

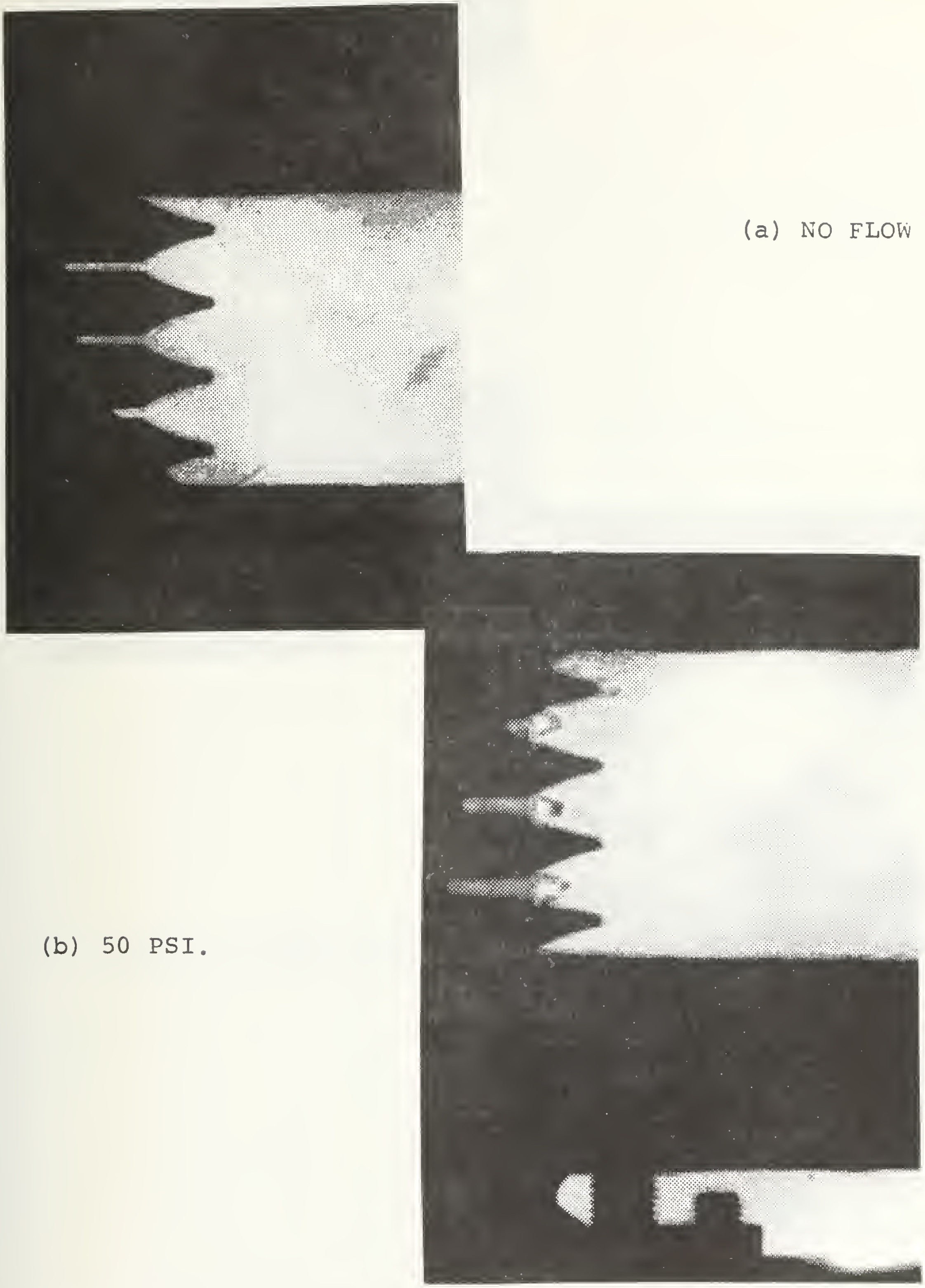

(a) NO FLOW

(b) 50 PSI.

FIGURE (34) SCHLIEREN PHOTOGRAPHS OF FOUR NOZZLES BEFORE "STARTING"

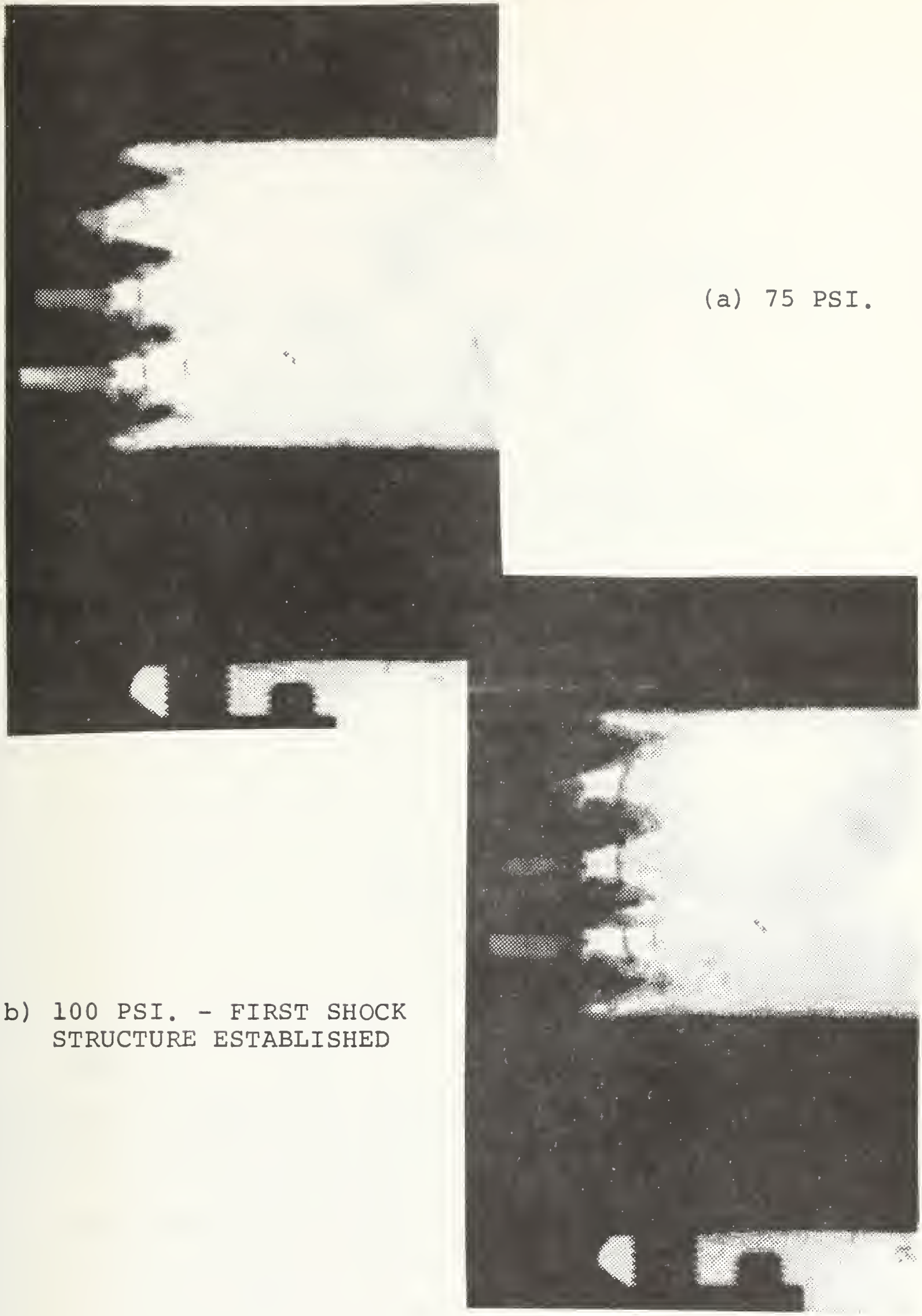

(a) 75 PSI.

(b) 100 PSI. - FIRST SHOCK STRUCTURE ESTABLISHED

FIGURE (35) SCHLIEREN PHOTOGRAPHS OF CENTER THREE NOZZLES STARTING

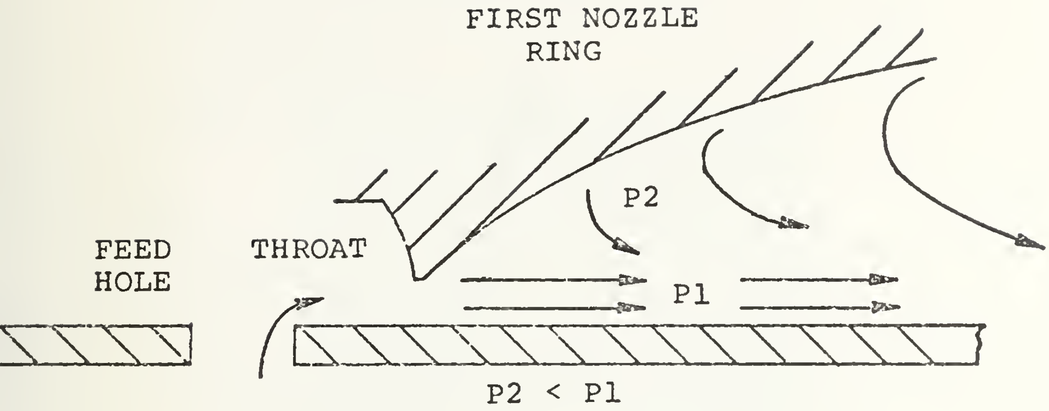
FIRST NOZZLE RING
P2
FEED HOLE
THROAT
P1
P2 < P1

(a) Flow at Pressure Less Than 50 PSI.

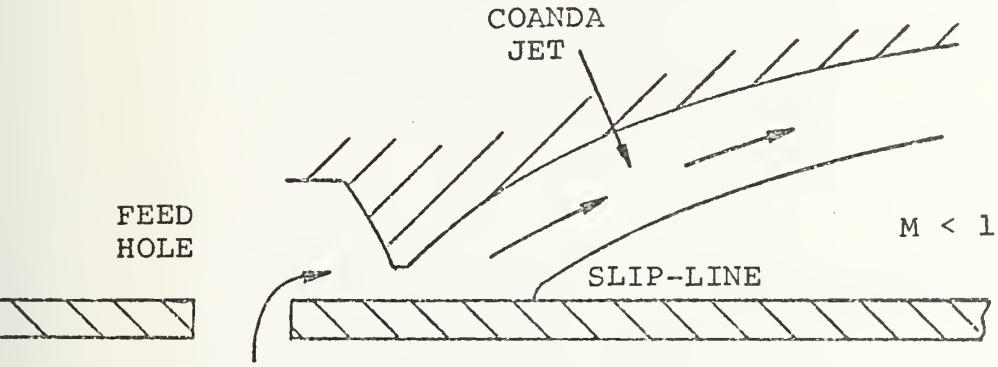
COANDA JET
FEED HOLE
M < 1
SLIP-LINE

(b) Resulting Coanda Jet Attached to Nozzle Wall

FIGURE (36) SCHEMATIC OF COANDA JET FORMATION

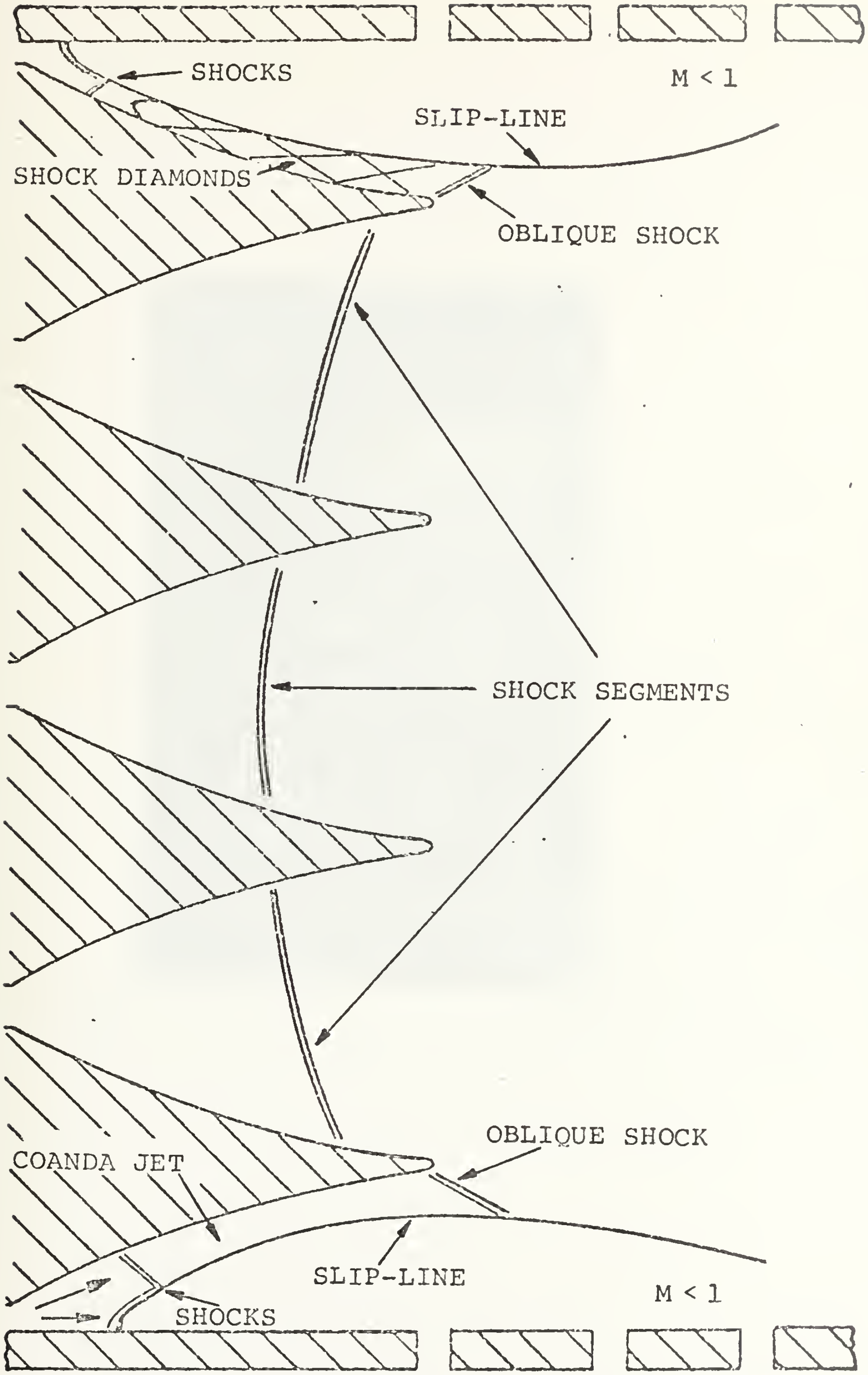
SHOCKS
M < 1
SLIP-LINE
SHOCK DIAMONDS
OBLIQUE SHOCK
SHOCK SEGMENTS
OBLIQUE SHOCK
COANDA JET
SLIP-LINE
M < 1
SHOCKS

FIGURE (37) SCHEMATIC OF FLOW AT A TOTAL PRESSURE OF 100 PSI.

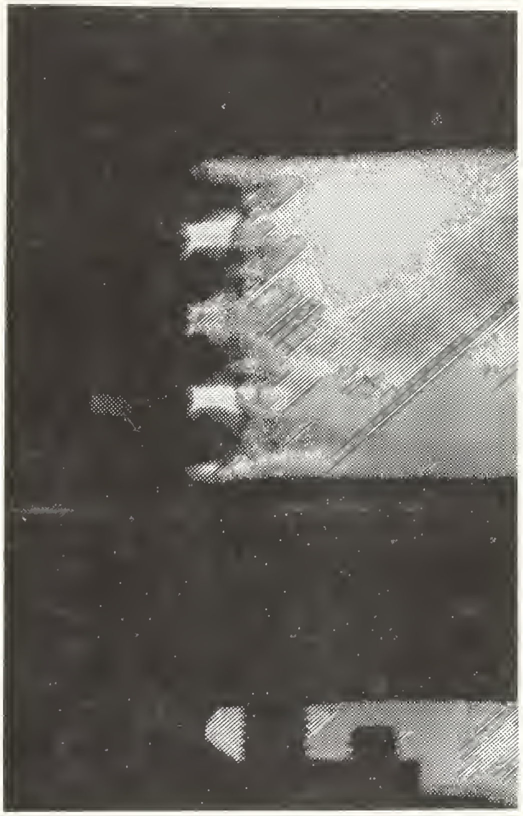

FIGURE (38) SCHLIEREN PHOTOGRAPH OF FLOW JUST BEFORE TRANSITION TO SECOND FLOW STRUCTURE — TOTAL PRESSURE 125 PSI.

transition to the second stage at 145 psi. It can be readily observed that failure of the end nozzles (actually "half" nozzles) to start complicates the flow structure a great deal. Coanda jets appear to be attached to end nozzle walls creating a "bubble" of relatively slow flow. A slip layer results between this slow region and the Coanda jet and appears in the Schlieren photographs as a light area. It was originally considered that these bright regions could be expansion waves turning the flow back to each wall. Inserting a probe into this region as shown in figure (42-b) established that the flow was in fact subsonic since it failed to produce oblique shock waves from the tip of the probe. Pressure readings were also recorded on the wall at the nozzle exit and by assuming isentropic flow from there to ambient pressures (calculating upstream), the Mach number was calculated and found to be subsonic. Table (5) lists the pressure data taken and the calculated Mach numbers. Figures (39) and (40) show the pressure and Mach number at the wall as functions of total pressure. The slip-line causes a bright area in the Schlieren photographs due to the higher entropy and temperature generated from friction, leading to an area of lower density.

Careful analysis of the photographs of the flow up to pressures of approximately 145 psi. (e.g. before transition to the second phase) show a shock wave starting normal to the wall within the end nozzles and then curving to the

Table 5 Wall Static Pressure at Nozzle Exit and Calculated Mach Number.

Total Gage Pressure (psi)	Wall Static Pressure (psi)*	Mach Number at Wall*
0	12.94	.43
20	12.42	.50
40	11.59	.59
60	11.0	.66
80	10.51	.71
100	9.72	.79
120	9.28	.84
130	- / 8.79	- / .89
135	- / 8.67	- / .90
140	8.56 / 10.63	.91 / .70
145	10.66 / 10.73	.69 / .69
150	10.69 / 10.78	.69 / .68
155	10.79	.68
160	10.78	.68

*The second values listed resulted from decreasing the total pressure from 150 psi (illustrating the hysteresis effect).

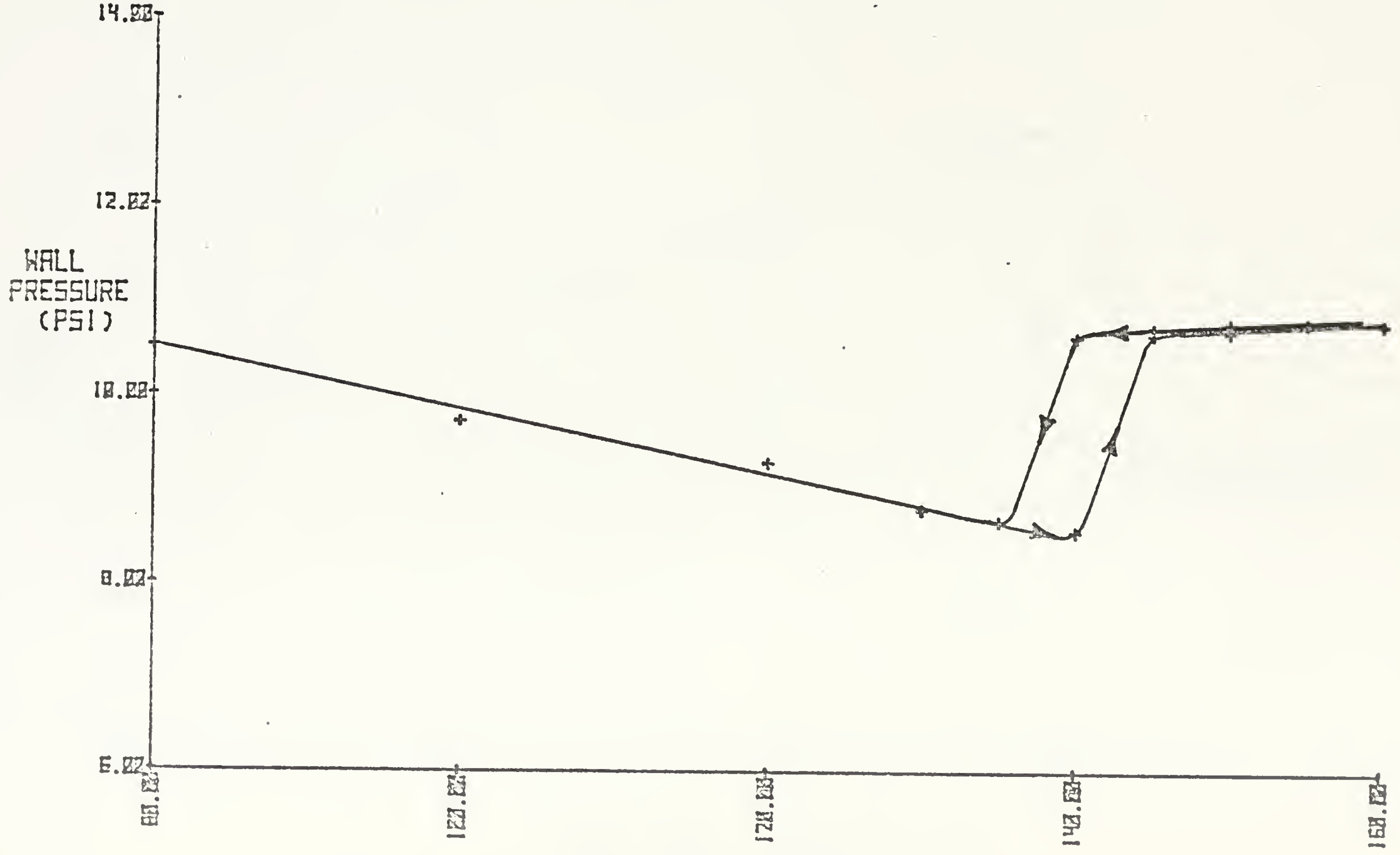

FIGURE (39) WALL STATIC PRESSURE VS. TOTAL PRESSURE

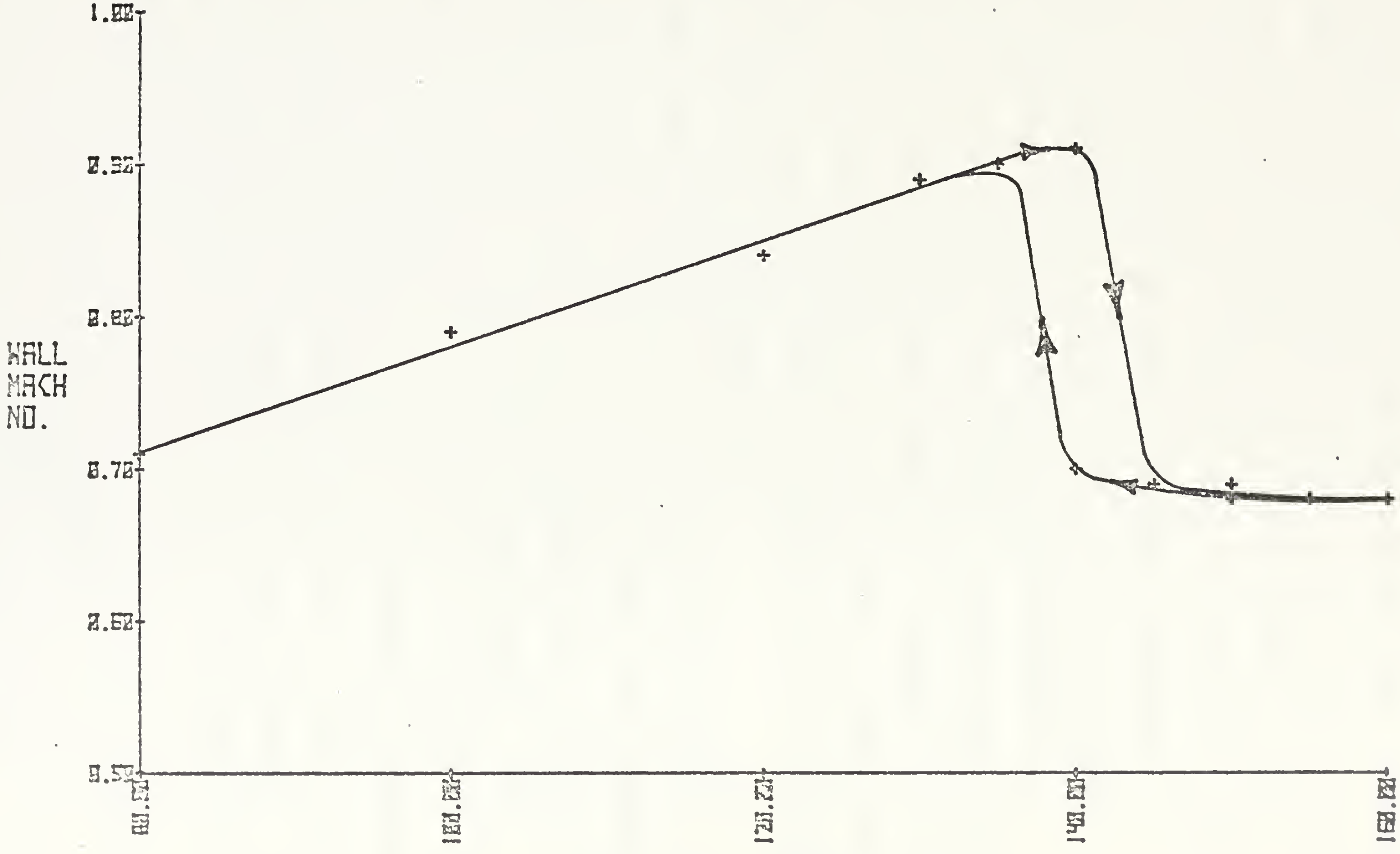

FIGURE (40) MACH NUMBER AT WALL VS. TOTAL PRESSURE

angle of the nozzle wall, where the slip layer forms between the Coanda jet and the subsonic "bubble." The slip layer continues to curve back toward the end wall. Observable in the lower jet are two small, nearly normal shock waves — one where the shock attached to the wall begins to curve outward and one from the trailing edge of the nozzle ring. These combine to slow the flow to subsonic velocities as testing with the probe revealed. The jet on the upper nozzle is smaller and faster which is attributable to a slightly smaller opening at the throat. Figure (38) shows the alternately light and dark regions of a series of shock diamonds in the upper Coanda jet, indicating a higher Mach number than in the lower nozzle. The slip line in the upper case also bends back toward the wall.

The high velocity jets occur for one of two reasons. First, since the end nozzles are really only "half-nozzles," the throats are only half the thickness of those in the center, in this case on the order of .045 inches. With these small openings located at the ends of the nozzle stack where the flow is entering axially at near sonic conditions, it has a difficult time "turning the corner" to exit out the first throat opening. If this were the case, whatever flow did make the 90° turn may attach itself to the nozzle wall as shown below.

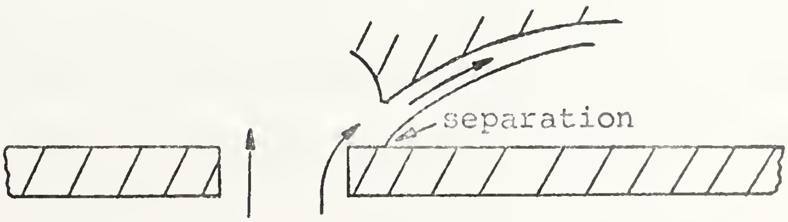

A second, more feasible explanation is that regardless of whether or not the flow has trouble turning the corner, the flow that travels through the throat starts as a jet of air near the wall at low pressures (in the order of 50 psi.) is shown in figure (36-a). This jet entrains the air near the nozzle wall and thus lowers the pressure in the wall region. The jet of air then moves toward the wall and attaches to it, displaying the "Coanda effect." As the flow in the jet moves out radially it slows and increases in pressure, forcing the slip line back toward the wall and creating a "bubble," observable in figure (35). As the total pressure increases toward the transition point of 145 psi., the bubble becomes longer as the flow in the jet takes a longer distance to reach a higher pressure.

The three nozzles in the center established normal shocks quite readily and moved outward to the nozzle exit with increasing pressure. As can be seen in the Schlieren photograph of figure (38), connecting these three waves would result in a cylindrical shock bowed inward at the center. Reference 2 states that a loss of total pressure in an axial direction will manifest itself in a shock wave that is conical, tapering inward in the direction of decreasing total pressure, rather than strictly cylindrical. For a stack of nozzle rings fed from both ends, as was the case in this experiment, such a loss in total pressure would result in the condition observed at pressures between 90 and 140 psi., that is, a tapering inward, from both ends. Total

pressures different from the region mentioned, however, did not result in a distortion of this type (see figures (41) through (48)). Seemingly, if axial total pressure losses were observable in a concave shock at pressures near 100 psi. they would also be observable at much higher pressures rather than disappear near 145 psi.

At a pressure of approximately ten atmospheres, transition to the second phase flow structure occurred. Figures (41)(a) and (b) are Schlieren photographs of the flow at total pressures of 150 and 175 psi. This transition consisted of a sudden rise in the wall pressure, and therefore a drop in the Mach number, as shown in figures (39) and (40), respectively. The Coanda jets no longer form a subsonic bubble, but instead the slip layer extends upward at an angle of 19 degrees. The cause of the transition to the condition shown in figure (43) is the movement of the normal shock segments beyond the trailing edges of the nozzles. Since the flow leaves the nozzles at approximately a five to ten degree angle, oblique waves bend the ends of the normal shock segments outward giving them a concave shape. Shock diamonds form behind the oblique waves serving to return the flow to subsonic conditions. AVCO Everett in Ref. 2 predicts that disturbances traveling downstream from the trailing edges would only affect the cylindrical shock wave locally, causing outward protrusions on the surface of the shock. Though the oblique shocks are rather large

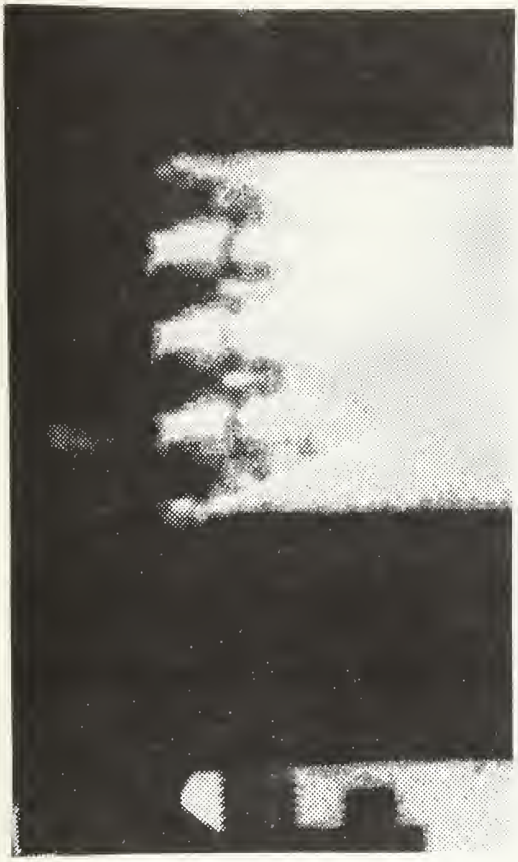

(a) 150 PSI.

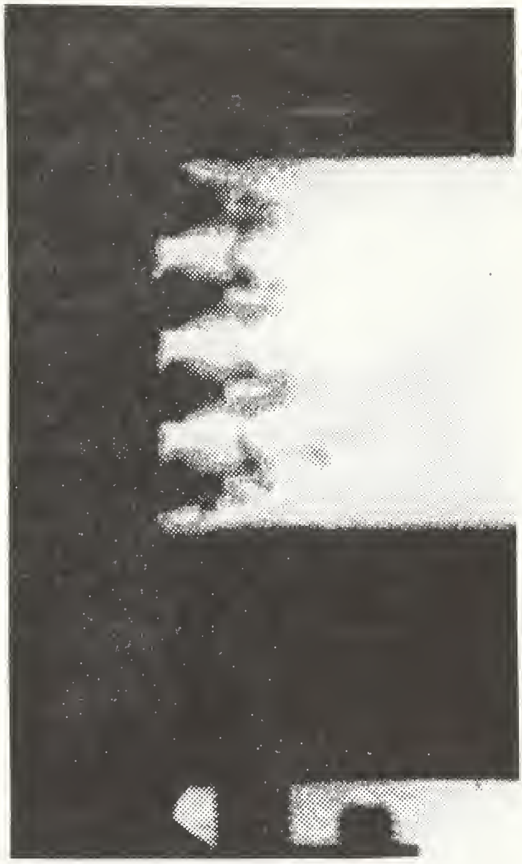

(b) 175 PSI.

FIGURE (41) SCHLIEREN PHOTOGRAPHS SHOWING CURVED SHOCK SEGMENTS BEYOND TRAILING EDGES OF NOZZLES AFTER TRANSITION TO SECOND PHASE

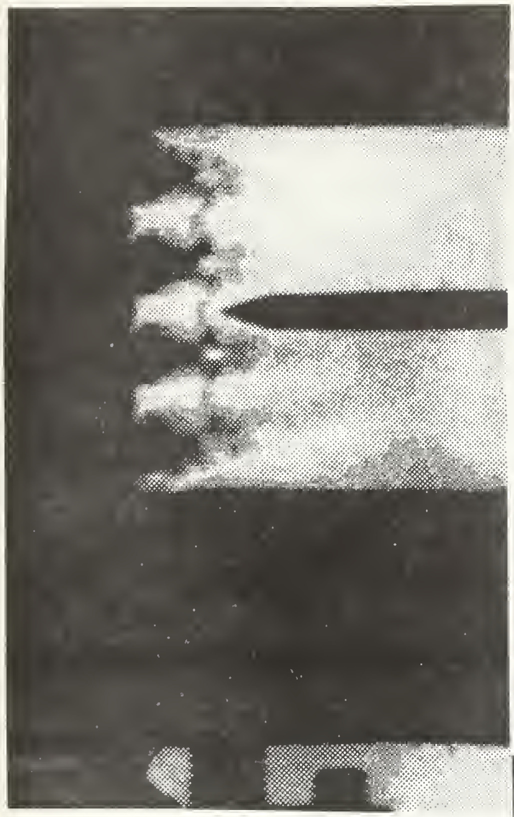

(a) 150 PSI. - SUBSONIC BEHIND CURVED SHOCK SEGMENT

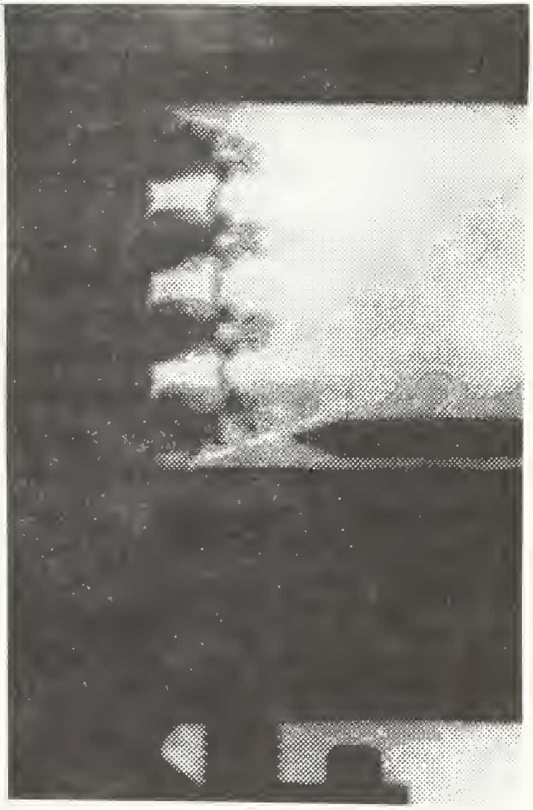

(b) 150 PSI. - SUBSONIC IN WALL REGION

FIGURE (42) SCHLIEREN PHOTOGRAPHS WITH PROBE SHOWING REGIONS OF SUBSONIC FLOW

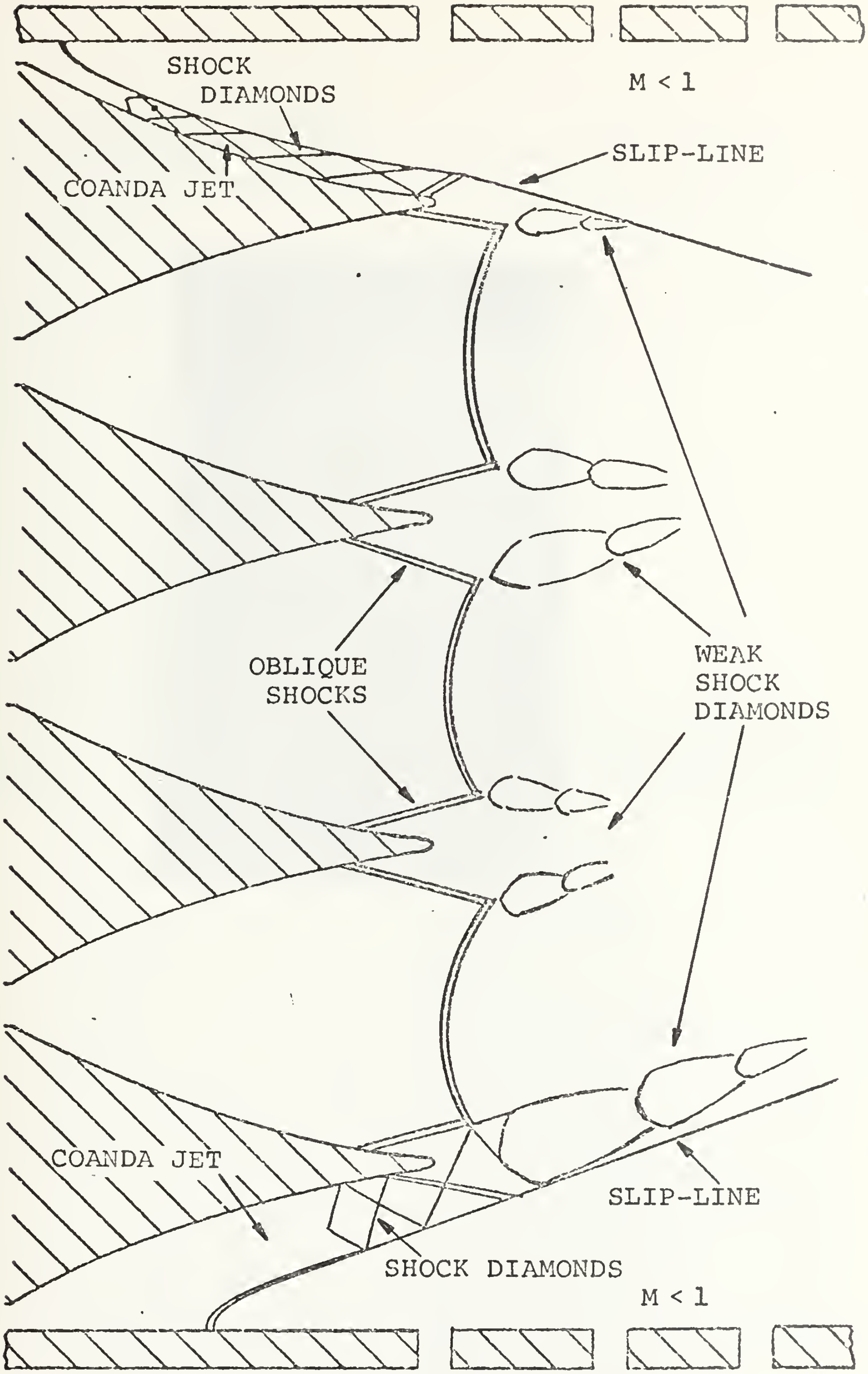
SHOCK DIAMONDS
M < 1
SLIP-LINE
COANDA JET
OBLIQUE SHOCKS
WEAK SHOCK DIAMONDS
COANDA JET
SLIP-LINE
SHOCK DIAMONDS
M < 1

FIGURE (43) SCHEMATIC OF THE FLOW STRUCTURE AT A TOTAL PRESSURE OF 175 PSI.

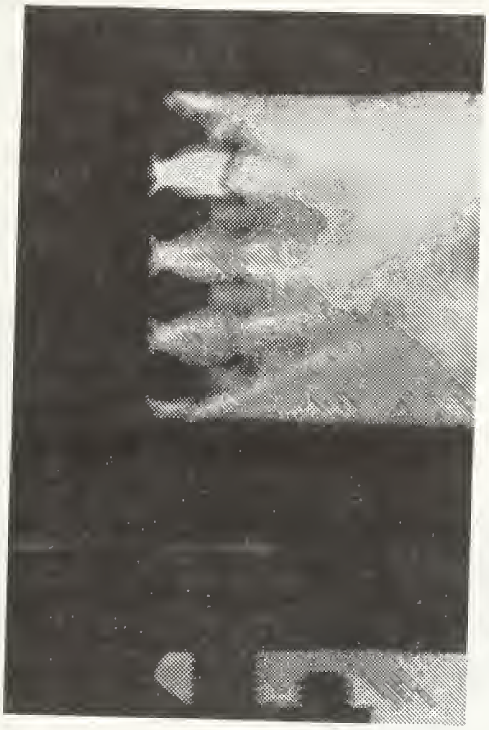

FIGURE (44) SCHLIEREN PHOTOGRAPHS OF FLOW JUST BEFORE DEVELOPING INTO THIRD STAGE — TOTAL PRESSURE OF 200 PSI.

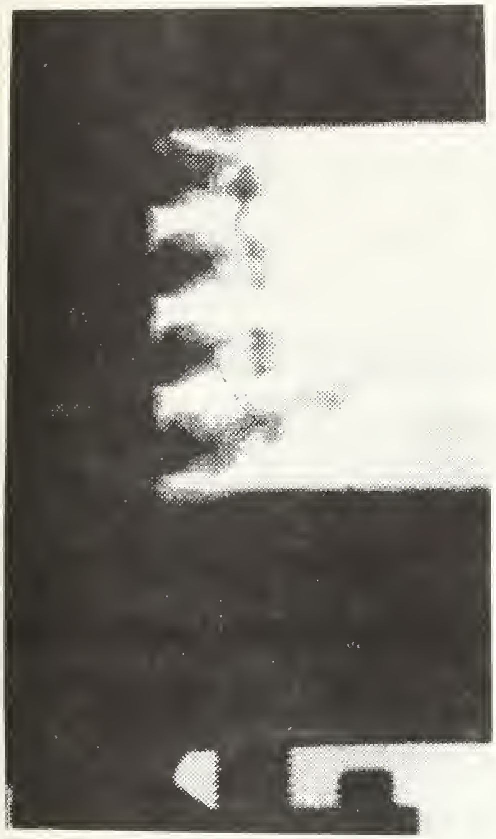

(a) 220 PSI.

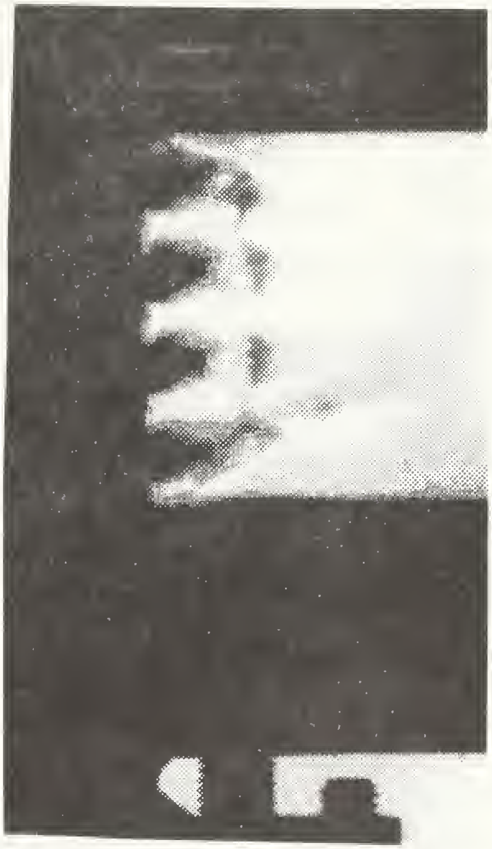

(b) 240 PSI.

FIGURE (45) SCHLIEREN PHOTOGRAPHS SHOWING DEVELOPMENT OF FLOW TO THIRD STAGE

"disturbances," this prediction appears to hold by the fact that the ends of the normal shock segments "protrude" outward. Flow exiting in a more nearly horizontal direction would minimize the strength of these oblique waves, thereby making the shock segments less curved and closer to joining into a complete cylindrical shock wave.

The second phase is also characterized by the disappearance of the subsonic "bubble" in each end nozzle. As the normal shock in the passage above (or below) the end nozzle moves beyond the trailing edge, a pressure mismatch occurs between the very low pressure region behind the shock and the Coanda jet coming off the trailing edge on the opposite side of the nozzle ring. This causes the Coanda jet to be diverted upward (or downward), and the resulting slip-line to extend upward (or downward). The angle that the slip-line forms increases from 19 degrees at transition (150 psi.) to 29 degrees at the maximum pressure of 250 psi. This change is due to the increase in the pressure mismatch created at the trailing edge. Since the trailing edge is blunt, the Coanda effect will continue to force the jet to higher angles as it tries to move around the trailing edge. This is not the case with a sharp trailing edge where the angle of the Coanda jet would remain the same.

As the pressure was increased from 150 psi. to 200 psi. the flow maintained the basic configuration shown in figure (43). Figures (41), (42) and (44) are Schlieren photographs

of the flow in this range of pressures. At 200 psi the oblique waves from the trailing edges are longer, better defined, and at a smaller angle. The curved shock segments have moved to approximately a quarter of an inch beyond the trailing edges. At approximately 210 psi. the flow structure is altered a second time.

Transition to the third stage, unlike the abrupt change at 145 psi., was a gradual development of normal shock segments in the nozzle wakes. Between pressures of 205 and 215 psi. the normal segments slowly appear, along with two weak oblique shocks at the trailing edges where one strong wave had been at lower pressures. Increasing the total pressure to 250 psi. changed the flow structure only by moving both the normal and curved segments of the shock slightly farther out from the trailing edges. Figure (47) is a schematic of the fully developed flow. Figure (46) is a Schlieren photograph of the flow at the maximum pressure applied, and shows that the normal portions of the shock are at a distance of approximately three eighths to a half of an inch. This distance is short of creating a lasing cavity wide enough to allow the theoretically available power in the flow to be extracted, which for four nozzles is 1.7 inches. For a spacing of the nozzles s , $(s)/(r_s-r_e) = 0.85$, where r_s is the shock location. As a fraction of the minimum shock location allowable to extract the power available, (r_m-r_e), the location of the shock wave is:

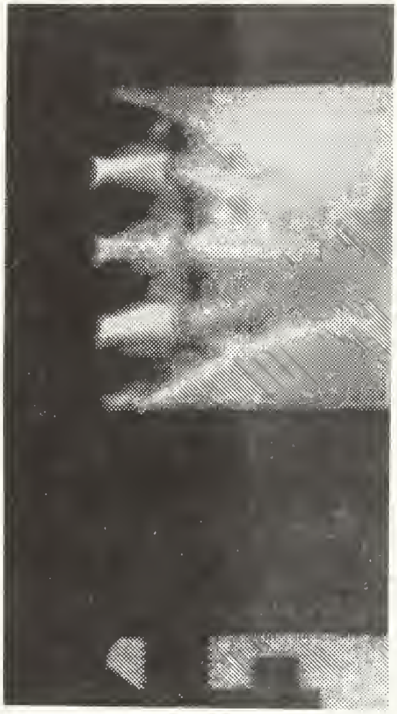

FIGURE (46) SCHLIEREN PHOTOGRAPH OF FLOW AT MAXIMUM TOTAL PRESSURE OF 250 PSI. NORMAL SHOCK SEGMENTS APPROXIMATELY 3/8 INCH FROM TRAILING EDGES

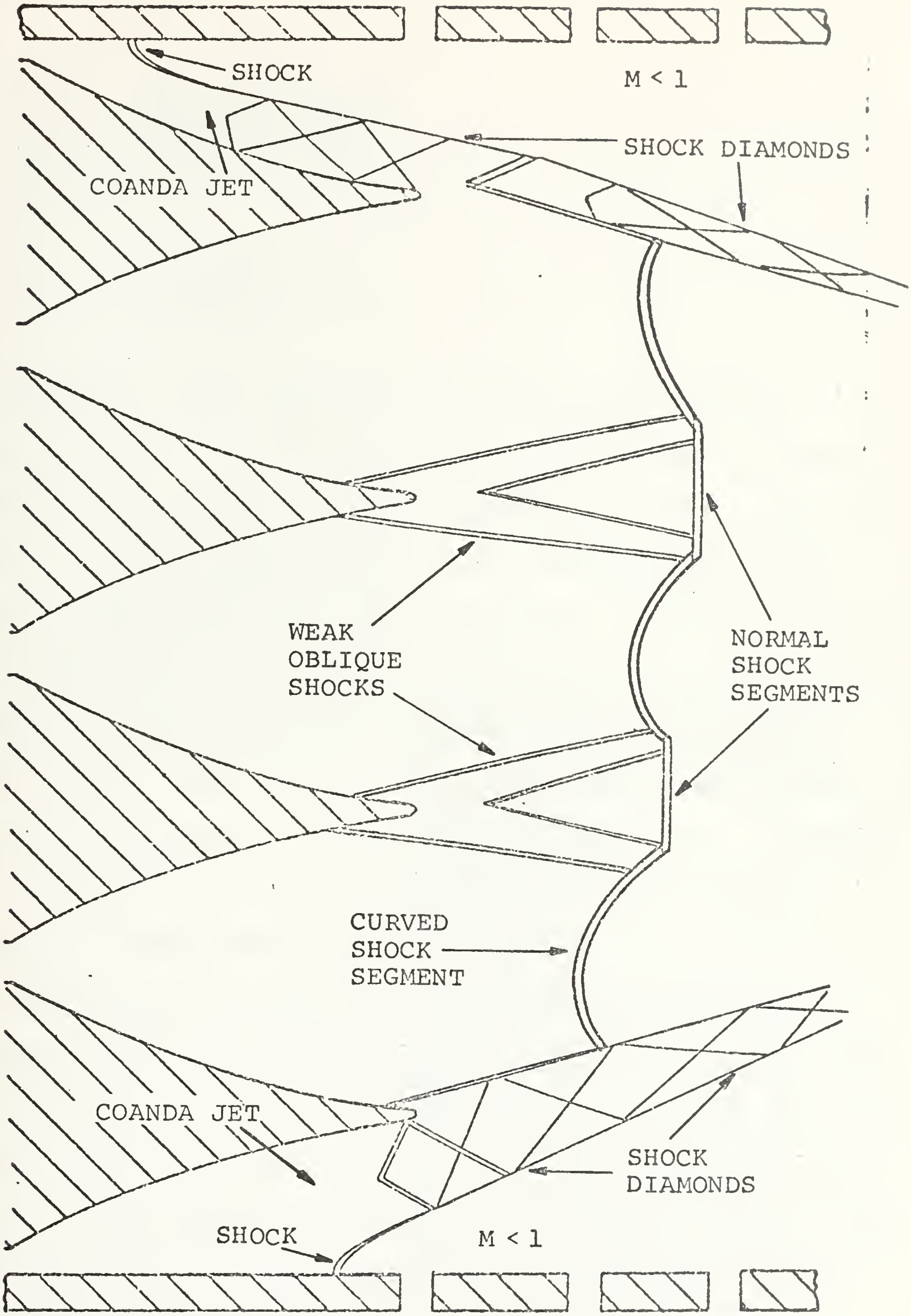
SHOCK
M < 1
SHOCK DIAMONDS
COANDA JET
WEAK
OBLIQUE
SHOCKS
NORMAL
SHOCK
SEGMENTS
CURVED
SHOCK
SEGMENT
COANDA JET
SHOCK
DIAMONDS
SHOCK
M < 1

FIGURE (47) SCHEMATIC OF THE FLOW STRUCTURE AT A TOTAL PRESSURE OF 250 PSI.

$$\frac{(r_s-r_e)}{(r_m-r_e)} = \frac{0.5}{1.7}$$

$$\frac{(r_s-r_e)}{(r_m-r_e)} = 0.3 \quad .$$

Boundary layer bleed was applied over the range of pressures with little if any effect on the flow. Figures (48)(a) and (b) are Schlieren photographs of the flow at 200 and 250 psi. respectively with a one-half psi. bleed pressure applied to the first three rows of bleed holes on the upper plate. At a total pressure of 250 psi the flow entrained between the slip-lines is diverted toward the bleed plate. This was the only noticeable change caused by the bleed over the entire range of pressures. Attempts were made at applying enough suction to start the end nozzles but were unsuccessful.

Homogeneity of the flow in the lasing cavity is a necessity for an operational laser. This was not the case for the fully developed flow at 250 psi. since the end nozzles failed to accelerate the flow to supersonic conditions. Other disturbances such as the oblique shock waves from the trailing edges should not be present to produce homogeneous conditions in the lasing cavity.

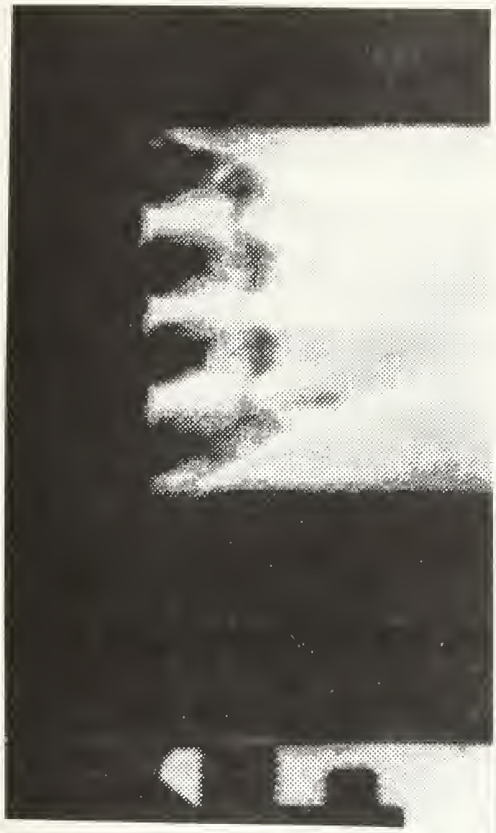

(a) 200 PSI.

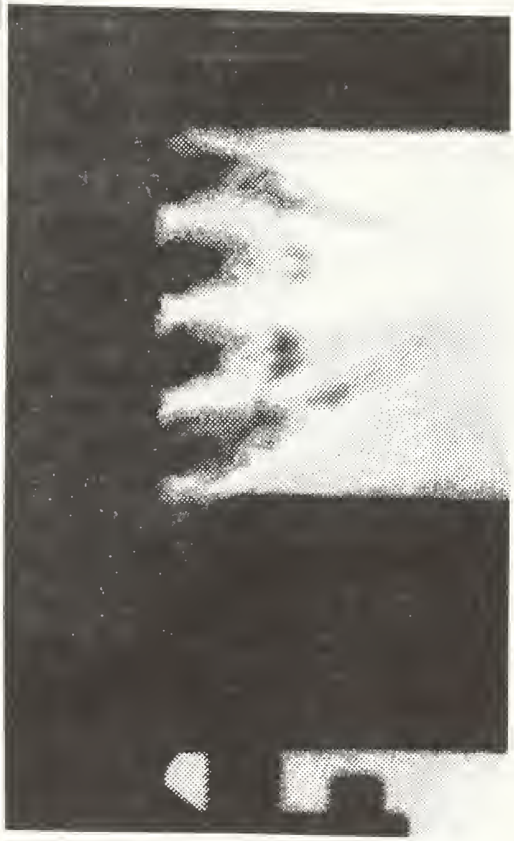

(b) 250 PSI.

FIGURE (48) SCHLIEREN PHOTOGRAPHS SHOWING FLOW WITH BOUNDARY LAYER BLEED APPLIED TO UPPER PLATE

B. CONCLUSIONS AND RECOMMENDATIONS

Testing of the cylindrical nozzle stack at a total pressure of 250 psi. established a shock wave approximately a half of an inch from the nozzle exit. The shock wave consisted of two segments normal to the flow (actually shock "bands" around the nozzle stack) connected by shock segments curved inward. Failure of the end "half-nozzles" to start resulted in subsonic flow near the end walls for the entire range of total pressures investigated. This prevented the normal shock from reaching the end walls.

Since subsonic flow existed at the end walls and the shock did not reach the walls, the use of boundary layer bleed had very little visible effect on the flow structure.

Flow visualization became very distorted at high pressures due to the extreme density gradients and the cylindrical geometry of the shock waves.

The following recommendations are made for further research on this subject:

1. Increase the diameter of the nozzle rings to allow for more mass flow to enter the nozzle stack without decreasing structural integrity and without choking in the feed passages.
2. Decrease the thickness of the nozzle rings to lower the expansion ratio and thus lower the exit Mach number.
3. Ensure sharp trailing edges on the nozzle rings.

4. To help avoid starting problems in the end nozzles, use half of a nozzle ring (sliced along the edge) at each end. This would eliminate the "half-nozzle" arrangement and the Coanda jets.
5. Investigate total pressures in excess of 250 psi.
6. Install pressure taps on the center nozzle wall to determine Mach number. Optical distortion due to the large density gradients and the cylindrical geometry results in difficulty observing shock angles from a probe inserted in the flow.

APPENDIX A

THEORETICAL LASING POWER AVAILABLE

Intensity is defined as radiation power per unit area, with units of kilowatts per square foot. Assuming a Gaussian intensity distribution on each mirror as shown in figure (A-1) the intensity is

$$I(r) = I_p \, e^{-r^2 c} \quad .$$

To satisfy the boundary condition of

$$I = I_p \, (1/e^2)$$

at $r = r_e$, then

$$c = 2/r_e{}^2 \quad .$$

Therefore:

$$I(r) = I_p \, e^{-2r^2/r_e{}^2} \quad . \qquad \text{(A-1)}$$

Equation (A-1) yields a Gaussian peak centered at r=0. To obtain a ring with Gaussian cross section having the peak intensity at $r=\bar{r}$, define

$$r = r - \bar{r} \quad .$$

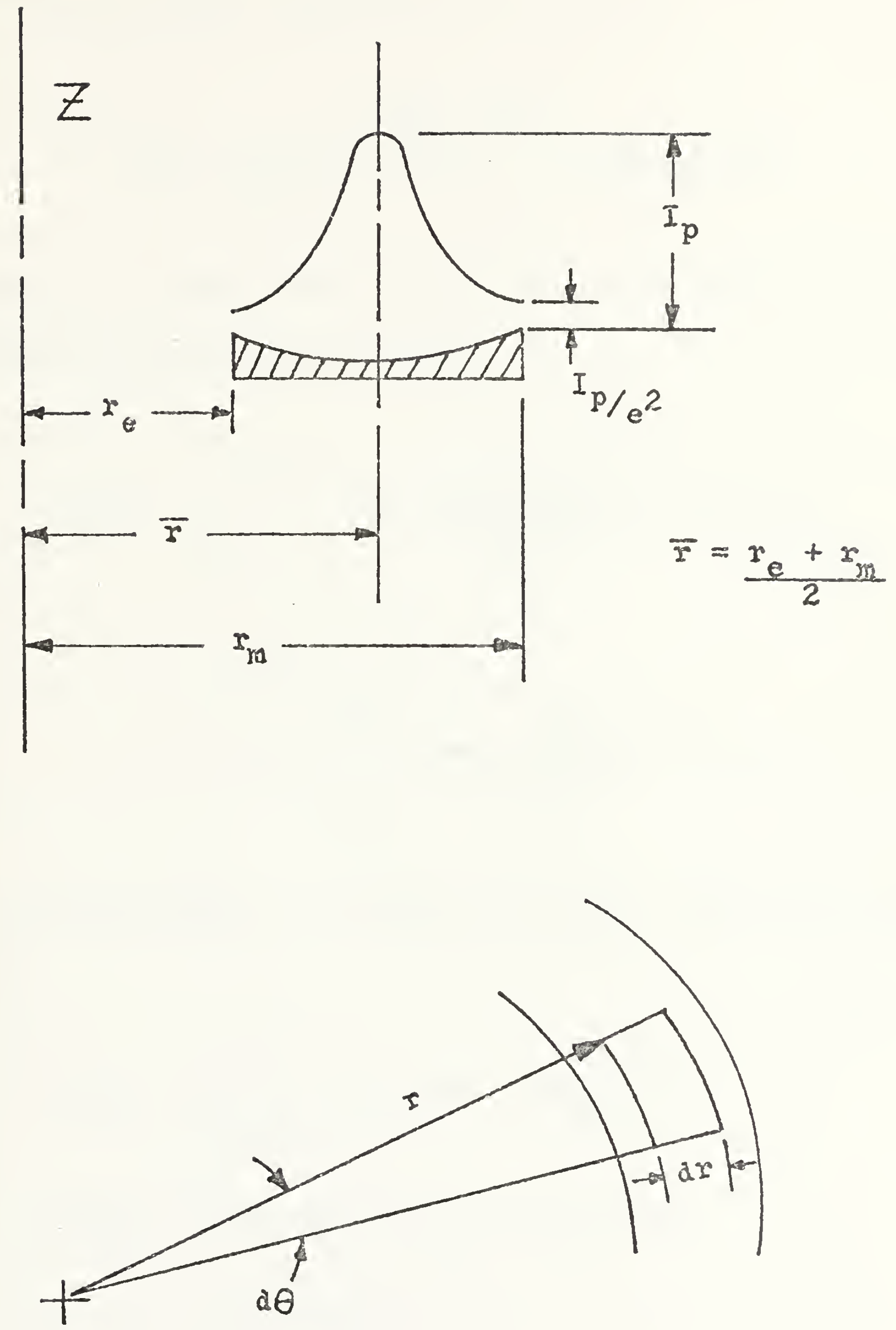
Z
I_p
I_{p/e^2}
r_e
$\overline{r}$
r_m
$\overline{r} = \frac{r_e + r_m}{2}$
r
dr
dθ

FIGURE (A-1) LASING MIRROR INTENSITY LOADING

Inserting this into equation (A-1) yields

$$I(r) = I_p \, e^{-[\frac{r-\bar{r}}{r_e-\bar{r}}\sqrt{2}]^2} \quad \text{kwatts/cm}^2 \quad .$$

To obtain the total power output, the intensity must be integrated over the mirror area.

$$\text{Power} = \int_{r_e}^{r_m} \int_0^{2} I_p \exp[\frac{r-\bar{r}}{r_e-\bar{r}}\sqrt{2}\ ]^2 \, r \, dr \, d\theta$$

$$P = 2\ I_p \int_{r_e}^{r_m} r \exp[\frac{r-\bar{r}}{r_e-\bar{r}}\sqrt{2}\ ]^2 \, dr \quad . \tag{A-2}$$

An alternate method of finding the power available from the flow is

$$\text{Power} = (\text{mass flow rate}) \binom{\text{specific}}{\text{energy}}$$

$$\text{Power} = E\ (\text{kjoules/lb}_m)\ \dot{m}\ (\text{lb}_m\text{/sec})$$

$$P = E\ \dot{m} \quad \text{kwatts}$$

or

$$P = 2\pi r_e L \rho_o a_o (\rho_e/\rho_o)(a_e/a_o) M_e E \quad . \tag{A-3}$$

Equating equations (A-2) and (A-3):

$$I_p \int_{r_e}^{r_m} r \exp\left[\frac{r-\bar{r}}{r_e-\bar{r}}\sqrt{2}\,\right]^2 dr = r_e L \rho_o a_o (\rho_e/\rho_o)(a_e/a_o) M_e E \,, \tag{A-4}$$

where the only unknown in equation (A-4) is the outer radius of the mirror, r_m.

In solving the integral Q on the left side of equation (A-4) define

$$x = \frac{r-\bar{r}}{r_e-\bar{r}}\sqrt{2} \,,$$

making

$$dx = \frac{\sqrt{2}}{r_e-\bar{r}}\, dr$$

and

$$r = \frac{r_e-\bar{r}}{\sqrt{2}}\, x + \bar{r} \,.$$

Making the corresponding changes in the limits of integration:

$$@ \quad r = r_e \,, \quad x = \sqrt{2}$$

$$@ \quad r = r_m \,, \quad x = -\sqrt{2} \,,$$

the integral now takes the form

$$Q = \int_{\sqrt{2}}^{-\sqrt{2}} (\bar{r} + \frac{r_e - \bar{r}}{\sqrt{2}} x)\ e^{-x^2}\ (\frac{r_e - \bar{r}}{\sqrt{2}})\ dx \quad ,$$

or

$$Q = \int_{\sqrt{2}}^{-\sqrt{2}} \bar{r}\ (\frac{r_e - \bar{r}}{\sqrt{2}})\ e^{-x^2}\ dx + (\frac{r_e - \bar{r}}{\sqrt{2}}) \int_{\sqrt{2}}^{-\sqrt{2}} x\ e^{-x^2}\ dx \ . \qquad \text{(A-5)}$$

Since the second term on the right side of equation (A-5) contains an integral of an odd function between symmetric limits, the integral goes to zero leaving

$$Q = -2 \int_{0}^{\sqrt{2}} \bar{r}\ \frac{(r_e - \bar{r})}{\sqrt{2}}\ e^{-x^2}\ dx \quad . \qquad \text{(A-6)}$$

Multiplying and dividing the right side of equation (A-6) by $\pi/2$ and rearranging,

$$Q = \frac{\sqrt{2\pi}\ \bar{r}\ (r - r_e)}{2} \int_{0}^{\sqrt{2}} \frac{2}{\sqrt{\pi}}\ e^{-x^2}\ dx \quad . \qquad \text{(A-7)}$$

Noting that the integral in equation (A-7) is the definition of the error function gives

$$Q = \sqrt{\pi/2}\ \ \bar{r}\ (\bar{r} - r_e)\ \operatorname{erf}(\sqrt{2}\,) \quad . \qquad \text{(A-8)}$$

Substituting equation (A-8) for the integral in equation (A-4):

$$I_p[\sqrt{\pi/2}\,\bar{r}\,(\bar{r}-r_e)\ \mathrm{erf}(\sqrt{2}\,)] = r_e L \rho_o a_o (\rho_e/\rho_o)(a_e/a_o) M_e E\ ,$$

or, solving for $\bar{r}$,

$$\bar{r} = (r_e\,/\,2) + 1/2\sqrt{r_e^{\,2} + C} \qquad \text{(A-9)}$$

where

$$C = \frac{4\ r_e\ L \qquad M_e\ E}{\sqrt{\pi/2}\ I_p\ \mathrm{erf}(\sqrt{2}\,)}\ .$$

Since

$$\bar{r} = \frac{r_e + r_m}{2}\ ,$$

equation (A-9) can be written

$$r_m = \quad r_e^{\,2} + C\ . \qquad \text{(A-10)}$$

The values in the expression for C are:

r_e = 1.5 inches

ρ_o = (.002378)(32.174)(10) = .765 lb_m/ft^3

a_o = 1119 ft/sec

$(a/a_o)_{M=4.5} = .445$

$(\rho/\rho_o)_{M=4.5} = .01745$

$M_e = 4.5$

$E = 5$ kwatts/(lb$_m$/sec)

$I_p = 3$ kwatts/cm^2 $= 2.8 \times 10^3$ kwatts/ft^2

$\operatorname{erf}(\sqrt{2}) = 2(.9773 - .500) = .9546$.

Using these values in the expression for C:

$$C = .2692(L) \text{ inches}^2 \quad .$$

For $r_e = 1.5$ inches, equation (A-10) becomes

$$r_m = \sqrt{2.25 + .2692\, L} \quad ,$$

where L is the length of the nozzle stack in inches. Dimension L is illustrated in figure (7).

As an example the power available from six nozzles was calculated. The theoretical lasing power available was found to be

$$\text{Power} = 2\pi I_p \int_{r_e}^{r_m} r \exp\left[\frac{r-\bar{r}}{r_e-\bar{r}}\sqrt{2}\,\right]^2 dr$$

$$= 2\pi I_p \operatorname{erf}(\sqrt{2})\sqrt{\pi/2}\,\left[\bar{r}(\bar{r}-r_e)\right]$$

$$= 2\pi(3)(30.5^2/144)(.9546)(\pi/2)^{\frac{1}{2}}[1.635(.135)]$$

Power = 32.16 kilowatts.

APPENDIX B

CALCULATIONS FOR DETERMINING INLET (FEED) AREA

Figure (13) shows the dimensions of the nozzle ring. The area of the hole segment between two centers is

$$A = \text{length} \times \text{width}$$

$$= \frac{\text{circumference}}{8} \times (\text{hole diameter})$$

$$= 2\pi \frac{(3/8 + 3/4)}{2} (1/8) \times (3/8)$$

$$A = .1407 \text{ in}^2 \ .$$

Since there are four segments:

$$A_1 = 4(.1407)$$

$$A_1 = .6627 \text{ in}^2 \ .$$

The area of the remaining half circles is

$$A_2 = 8 \times \frac{1}{2}\left[\frac{\pi(3/8)^2}{4}\right]$$

$$A_2 = .4418 \text{ in}^2 \ .$$

Therefore the total inlet area is

$$A_{in} = A_1 + A_2$$

$$A_{in} = 1.104 \text{ in}^2 \ .$$

APPENDIX C

DETAILS OF THROAT HEIGHT CALCULATIONS

The feed flow and the flow exiting through the nozzles must satifsy the continuity equation:

$$\dot{m}_{in} = \sum_{n=1}^{6} \dot{m}_{nozzle}$$

$$2\rho_{in}U_{in}A_{in} = 6\rho^*U^*A^* \qquad \text{(C-1)}$$

where the factor 2 in equation (C-1) results from the nozzle stack being fed from both ends.

Using the equation of state, and noting that velocity is the product of Mach number and the speed of sound, equation (C-1) can be written

$$\frac{P_{in}}{RT_{in}}(M_{in}a_{in})(A_{in}) = 3(\frac{P^*}{RT^*})(1)(a^*)(2\pi r_t h)$$

$$\frac{P_{in}}{\sqrt{T_{in}}} M_{in}A_{in} = 6\,\frac{P^*}{\sqrt{T^*}}\,h \quad .$$

Solving for the throat height:

$$h = (\frac{1}{6\pi})\, M_{in}A_{in}(\frac{P_{in}}{P^*})(\frac{T^*}{T_{in}})^{\frac{1}{2}} \quad . \qquad \text{(C-2)}$$

Multiplying the right side by $(\frac{P_o}{P_o})$ and $(\frac{T_o}{T_o})^{\frac{1}{2}}$, equation (C-2) can be written as

$$h = (\frac{1}{6\pi}) M_{in} (\frac{P_{in}}{P_o}) (\frac{P_o}{P*}) (\frac{T*}{T_o})^{\frac{1}{2}} (\frac{T_o}{T_{in}})^{\frac{1}{2}} \quad . \qquad \text{(C-3)}$$

Using the isentropic equation relating stagnation temperature and pressure to static temperature and presure respectively, and applying them to the Mach equals one condition, equation (C-3) becomes

$$h = (\frac{1}{6\pi}) M_{in} (\frac{P_{in}}{P_o}) (\frac{1}{.5283}) (.8333) (\frac{T_o}{T_{in}})^{\frac{1}{2}}$$

or

$$h = .0917 \frac{M_{in} (P_{in}/P_o)}{(T_{in}/T_o)^{\frac{1}{2}}} \quad . \qquad \text{(C-4)}$$

Noting that

$$\frac{P_o}{P} = (\frac{T_o}{T})^{\gamma/\gamma-1} = (1 + \frac{(\gamma-1)}{2} M^2)^{\gamma/\gamma-1} \quad ,$$

equation (C-4) reduces to

$$h = .0917 M_{in} \frac{1}{(T_o/T_{in})^{-\frac{1}{2}} (T_o/T_{in})^{\gamma/\gamma-1}}$$

or

$$h = .0917\ M_{in}(T_{in}/T_o)^{\frac{\gamma+1}{2(\gamma-1)}}$$

$$h = .0917\ M_{in}\left(1 + \frac{(\gamma-1)}{2}\ M_{in}{}^2\right)^{\frac{-(\gamma+1)}{2(\gamma-1)}}$$

$$h = \frac{.0917\ M_{in}}{(1 + .2\ M_{in}{}^2)^3}\ .$$

APPENDIX D

AXIAL VARIATION OF MACH NUMBER AND PRESSURE

From Ref. 4, influence coefficients for flow in a channel are given as

$$\frac{dM^2}{M^2} = -2\,\frac{(1 + \frac{\gamma-1}{2} M^2)}{1-M^2}\,\frac{dA}{A} \qquad \text{(D-1)}$$

and

$$\frac{dP}{P} = \frac{\gamma M^2}{1-M^2}\,\frac{dA}{A} \qquad \text{(D-2)}$$

assuming isentropic flow and constant specific heat and molecular weight. Using the model shown in figure (D-1) and an inlet area of 1.105 square inches,

$$\frac{A_{out}}{A_{in}} = \frac{1}{16}$$

$$A_{out} = (\frac{1}{16})\ (A_{in})$$

$$A_{out} = .06906\ in^2\ .$$

Since

$$A_2 - A_1 = A_{out}\ ,$$

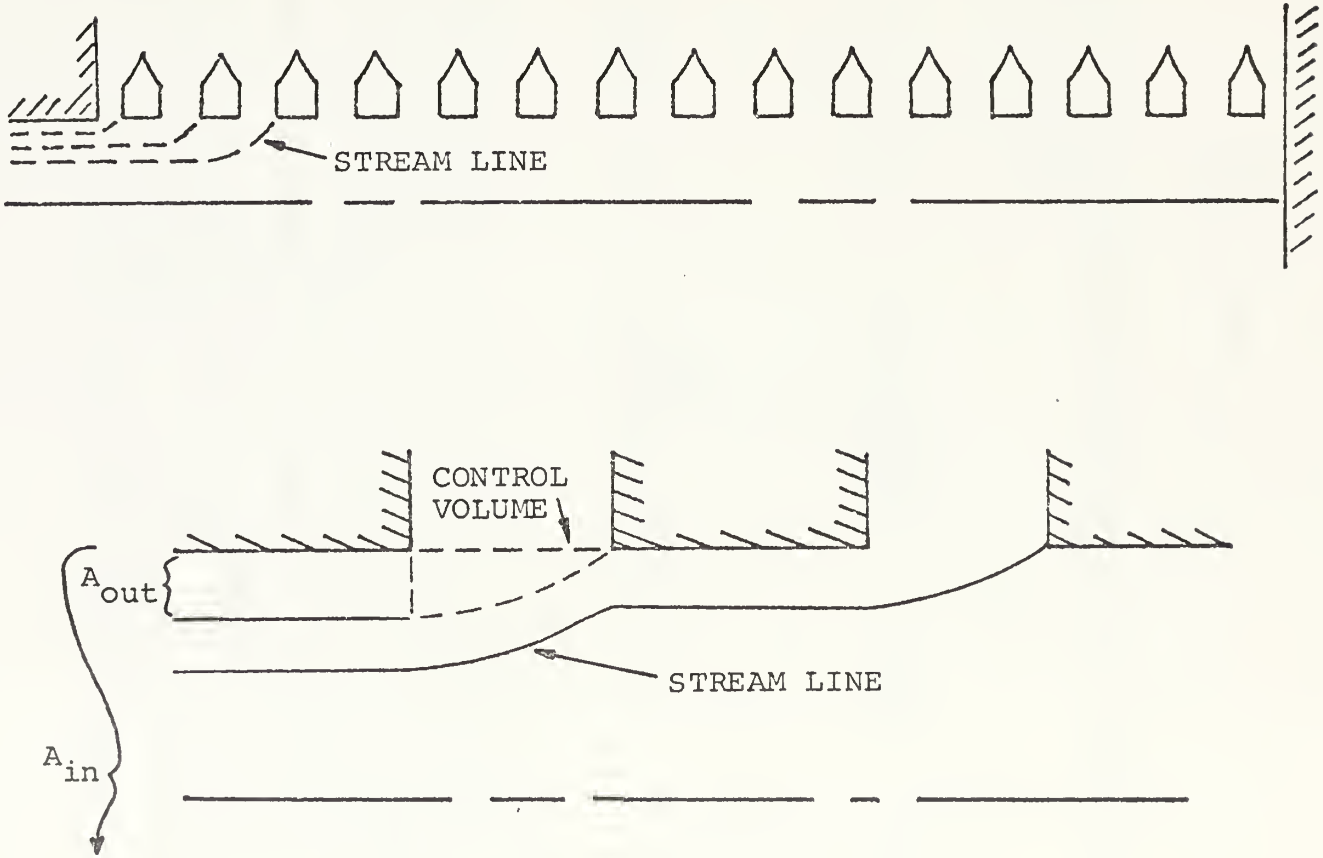
STREAM LINE
CONTROL VOLUME
A_{out}
STREAM LINE
A_{in}

FIGURE (D-1) AXIAL FLOW MODEL

$$\frac{A_2 - A_1}{A_1} = \frac{.06906}{1.105 - .06906}$$

or

$$\frac{dA}{A} = .06667 \quad .$$

Substituting this value into equations (D-1) and (D-2) and rearranging yields

$$M_{i+1} = M_i - M_i \left[\frac{1 + \frac{\gamma-1}{2} M_i^2}{1 - M_i^2} (.06667)\right] \qquad \text{(D-3)}$$

and

$$P_{i+1} = P_i + P_i \left[\frac{\gamma M_i^2}{1 - M_i^2} (.06667)\right] \quad . \qquad \text{(D-4)}$$

A program was written for the Hewlett Packard model 9830-A computer to calculate the axial variation of Mach number and pressure using equations (D-3) and (D-4). The program determines Mach number and pressure at stations one through thirteen using values of inlet Mach number and total pressure (PSF) as inputs. A listing of the program AXIAL and the results of the program are found in this appendix.

Table D-1 Symbols for Program AXIAL

Computer Notation	Algebraic	Description
M1	M_{in}	Inlet Mach number
P0	P_o	Stagnation pressure (PSF)
M( )		Mach number at subscripted station
P( )		Static pressure at subscripted station

LISTING OF COMPUTER PROGRAM "AXIAL"

```
10 PRINT "INPUT INLET MACH# AND TOTAL PRESS(PSF)"
20 DIM M[13],P[13]
30 INPUT M1,P0
40 M[1]=M1
50 P[1]=P0/((1+0.2*M1↑2)↑3.5)
60 PRINT
70 PRINT "INLET MACH#=";M1,"TOTAL PRESS=";P0;"PSF"
80 PRINT
90 PRINT "STA #","MACH#";"P STATIC(PSF)"
100 PRINT
110 PRINT "1";M[1];P[1]
120 FOR I=2 TO 13
130 A=1-M[I-1]↑2
140 M[I]=M[I-1]-0.06667*M[I-1]*(1+0.2*M[I-1]↑2)/A
150 P[I]=P[I-1]+P[I-1]*0.06667*(1.4*M[I-1]↑2)/A
160 PRINT I,M[I];P[I]
170 NEXT I
180 END
```

RESULTS OF PROGRAM "AXIAL"

```
INLET MACH#= 0.2                    TOTAL PRESS= 2116.8   PSF

STA #              MACH#            P STATIC(PSF)

1                   0.2              20376.03027
 2                  0.135993[illegible]       20658.3599
 3                  0.173065470      20727.15727
 4                  0.161099[illegible]82      20786.89163
 5                  0.150015754      20838.5879
 6                  0.139737386      20883.36808
 7                  0.130198914      20922.18773
 8                  0.121338930      20955.86257
 9                  0.113104202      20985.09164
 10                 0.105446287      21010.4726
 11                 0.098321328      21032.52282
 12                 0.091689461      21051.68504
 13                 0.085514332      21068.34491



INLET MACH#= 0.4                    TOTAL PRESS= 2116.8   PSF

STA #              MACH#            P STATIC(PSF)

1                   0.4              18951.20034
 2                  0.367236457      19288.12742
 3                  0.338172818      19568.77096
 4                  0.312133254      19804.62463
 5                  0.288627767      20004.16139
 6                  0.267286489      20173.84140
 7                  0.247821242      20318.71595
 8                  0.230001659      20442.81211
 9                  0.213639648      20549.38963
 10                 0.198578871      20641.11920
 11                 0.184687414      20720.21089
 12                 0.171852514      20788.50753
 13                 0.159976700      20847.55658
```

RESULTS OF PROGRAM "AXIAL" (CON'T)

```
INLET MACH#= 0.6               TOTAL PRESS= 21160   PSF

STA #          MACH#           P STATIC(PSF)

1               0.6             16589.52363
 2              0.53299665      17460.51714
 3              0.488540045     18107.21786
 4              0.436959864     18614.67462
 5              0.399577780     19024.70217
 6              0.36686411      19352.08675
 7              0.337846455     19643.14661
 8              0.311834403     19879.37194
 9              0.288357130     20079.23716
 10             0.267040150     20249.20577
 11             0.247596104     20394.33305
 12             0.229795217     20518.65006
 13             0.213449837     20625.4203



INLET MACH#= 0.8               TOTAL PRESS= 21160   PSF

STA #          MACH#           P STATIC(PSF)

1               0.8             13881.41744
 2              0.632880533     16184.81965
 3              0.556855368     17194.1841
 4              0.499706062     17915.50933
 5              0.453085391     18472.03545
 6              0.413514623     18917.40723
 7              0.379121795     19281.61093
 8              0.348754325     19583.71062
 9              0.321639268     19836.82393
 10             0.297226339     20050.4701
 11             0.275105941     20231.82379
 12             0.254962478     20386.44623
 13             0.236545949     20518.74135
```

APPENDIX E

DETERMINING POINTS ON THE NOZZLE WALL

Following a development similar to Ref. 4, but changing the characteristic network as shown in figure (E-1), equations can be developed to determine points along a right running characteristic proceeding in the $-\xi$ direction.

Along the characteristic segment

$$\int_2^3 \frac{\partial}{\partial \eta} (\nu-\theta)\, d\eta = \int_2^3 \sin \mu \frac{\sin \theta}{r}\, d\eta \tag{E-1}$$

and

$$\int_1^3 \frac{\partial}{\partial \xi} (\nu-\theta)\, d\xi = - \int_1^3 \sin \mu \frac{\sin \theta}{r}\, d\xi \tag{E-2}$$

where the negative sign on the right side of equation (E-2) results from traveling in the negative $-\xi$ direction when proceeding from point 1 to point 3. Assuming a very small characteristic mesh, the integrands on the right sides of equations (E-1) and (E-2) can be taken to be constant. With this assumption and some rearranging, the equations become

$$\nu_3 = \frac{1}{2} (\nu_1+\nu_2) + \frac{1}{2}(\theta_1-\theta_2)$$

$$+ \frac{1}{2} [-\sin \mu_1 \frac{\sin \theta_1}{r_1} \Delta\xi_{13} + \sin \mu_2 \frac{\sin \theta_2}{r_2} \Delta\eta_{23}]$$

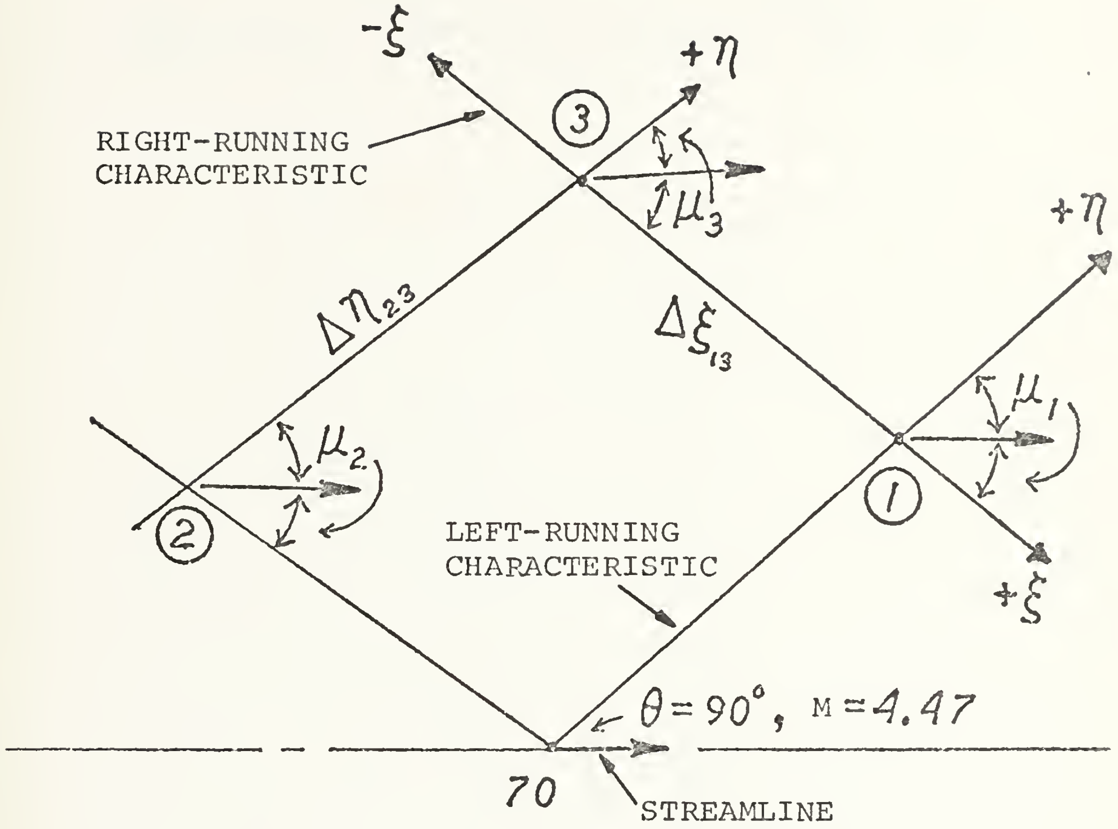
$-\xi$
$+\eta$
③
RIGHT-RUNNING CHARACTERISTIC
μ_3
$+\eta$
$\Delta\eta_{23}$
$\Delta\xi_{13}$
μ_2
μ_1
②
①
LEFT-RUNNING CHARACTERISTIC
$+\xi$
$\theta = 90°$, M = 4.47
70
STREAMLINE

FIGURE (E-1) MODIFIED CHARACTERISTIC ELEMENT

and

$$\theta_3 = \frac{1}{2}(\nu_1-\nu_2) + \frac{1}{2}(\theta_1+\theta_2)$$

$$+ \frac{1}{2}\left[-\sin\mu_1 \frac{\sin\theta_1}{r_1}\Delta\xi_{13} - \sin\mu_2 \frac{\sin\theta_2}{r_2}\Delta\eta_{23}\right] .$$

Table E-1 Results of Axisymmetric M. O. C.

POINT	MACH #	μ	θ	ν	θ+μ	θ−μ
1	1.082	67.57	91	1		23.4
2	1.256	52.74	95	5		42.3
4	1.435	44.17	100	10		55.83
6	1.605	38.55	105	15		66.45
8	1.775	34.29	110	20		75.71
10	1.95	30.85	115	25		84.153
12	2.134	27.945	120	30		92.05
14	2.14	27.8	122.65	32.65		94.85
3	1.198	56.6	90	3.55	146.6	
5	1.35	47.8	93.57	7.59	141.37	45.77
7	1.53	41.0	48.36	12.62	139.36	57.36
9	1.70	36.1	103.23	17.68	139.33	67.13
11	1.873	32.31	108.12	22.72	140.43	75.81
13	2.05	29.2	113.03	27.77	142.23	83.83
15	2.24	26.5	117.95	32.83	144.45	91.45
17	2.349	25.2	120.58	35.51	145.78	95.38
16	1.49	42.1	90.0	11.65	132.1	47.9
18	1.66	36.9	94.75	16.71	131.65	57.85
20	1.835	33.0	99.58	21.81	132.58	66.58

Table E-1 Results of Axisymmetric M. O. C. (Continued)

POINT	MACH #	μ	θ	ν	θ+μ	θ−μ
22	2.02	29.7	114.43	26.89	134.13	74.73
24	2.21	26.9	109.30	31.98	136.20	82.40
26	2.415	24.5	114.18	37.09	138.68	89.68
28	2.52	23.3	116.78	39.80	140.08	93.48
21	1.835	33.0	90	21.81	123.0	
23	2.02	29.65	94.82	26.95	124.47	65.17
25	2.215	26.85	99.65	32.08	126.50	72.80
27	2.42	24.40	104.50	37.22	128.90	80.1
29	2.64	22.20	109.36	42.40	131.56	87.16
31	2.77	21.15	111.95	45.15	133.10	90.80
34	2.218	26.75	90	32.18	116.75	
36	2.42	24.35	94.81	37.36	119.16	70.46
38	2.65	22.18	99.64	42.58	121.82	77.46
40	2.90	20.10	104.48	47.86	124.58	84.38
42	3.045	19.15	107.06	50.67	126.21	87.91
39	2.655	22.13	90.0	42.63	112.13	
41	2.9	20.1	94.81	47.95	114.91	74.71

Table E-1 Results of Axisymmetric M. O. C. (Continued)

POINT	MACH #	μ	θ	ν	$\theta+\mu$	$\theta-\mu$
43	3.19	18.25	99.63	53.37	117.88	81.38
45	3.36	17.31	102.20	56.26	119.51	84.89
52	3.19	18.23	90.00	53.42	108.23	
54	3.53	16.45	94.82	59.03	111.27	78.37
56	3.73	15.55	97.38	62.03	113.93	81.83
57	3.94	14.70	90.00	64.98	104.7	
59	4.19	13.82	92.55	68.16	106.37	78.73
70	4.47	12.93	90.00	71.49	102.93	
72	4.47	12.93	90.00	71.49	102.93	77.07
61	4.22	13.70	92.10	68.66	105.80	78.40
58	3.78	15.35	96.97	62.68	112.32	81.62
47	3.41	16.92	101.78	57.01	118.70	84.86
44	3.08	18.95	106.61	51.41	125.56	87.66
33	2.8	20.9	111.47	45.87	132.37	90.57
30	2.56	23.0	116.24	40.49	139.24	93.24
19			119.92	36.24		

Table E-1 Results of Axisymmetric M. O. C. (Continued)

POINT	MACH #	μ	θ	ν	$\theta+\mu$	$\theta-\mu$
74	4.47	12.94	90.00	71.49	102.93	77.07
63	4.24	13.65	91.87	68.87	105.52	78.22
60	3.79	15.32	96.72	62.88	112.04	81.40
49	3.42	17.03	101.5	57.18	118.53	84.47
46	3.1	18.85	106.31	51.55	125.16	87.46
35	2.81	20.8	111.15	45.97	131.95	90.35
32			115.90	40.55		
76	4.47	12.93	90.00	71.49	102.93	77.07
65	4.27	13.54	91.51	69.20	105.05	77.97
62	3.81	15.22	96.33	63.15	111.55	81.11
51	3.43	16.96	101.08	57.41	118.04	84.12
48	3.105	18.79	105.86	51.73	124.65	87.07
37	2.82	20.8	110.67	46.12	131.47	89.87
78	4.47	12.93	90.00	71.49		
67	4.315	13.41	91.03	69.65	104.44	77.62
64	3.84	15.11	95.80	63.59	110.91	80.69
53	3.455	16.8	100.49	57.82	117.29	83.69
50	3.125	18.63	105.21	52.10	123.84	86.58
80*	3.5		99			

* estimated

APPENDIX F

A. EJECTOR NOZZLE DESIGN

To assure starting of the cylindrical nozzles a back pressure must exist which is lower than the total pressure downstream of the shock. For a stagnation pressure of ten atmospheres, the total pressure downstream of a normal shock at a Mach number of five is less than one atmosphere. Ejectors were designed to lower the back pressure to a value below the total pressure downstream of the shock assuming Mach-five flow.

The models used for finding the flow conditions at the ejector nozzles are shown in figures (F-1) and (F-2). Applying the continuity equation

$$\rho_1U_1A_1 + \rho_2U_2A_2 = \rho_3U_3A_3 \quad , \qquad \text{(F-1)}$$

the momentum equation

$$\rho_1U_1^{\;2}A_1 + P_1A_1 + \rho_2U_2^{\;2}A + P_2A_2 = \rho_3U_3^{\;2}A_3 + P_3A_3 \quad , \qquad \text{(F-2)}$$

and the energy equation

$$\rho_1U_1A_1(C_pT_1 + U_1^{\;2}/2) + \rho_2U_2A_2(C_pT_2 + U_2^{\;2}/2) = \rho_3U_3A_3(C_pT_3 + U_3^{\;2}/2) \qquad \text{(F-3)}$$

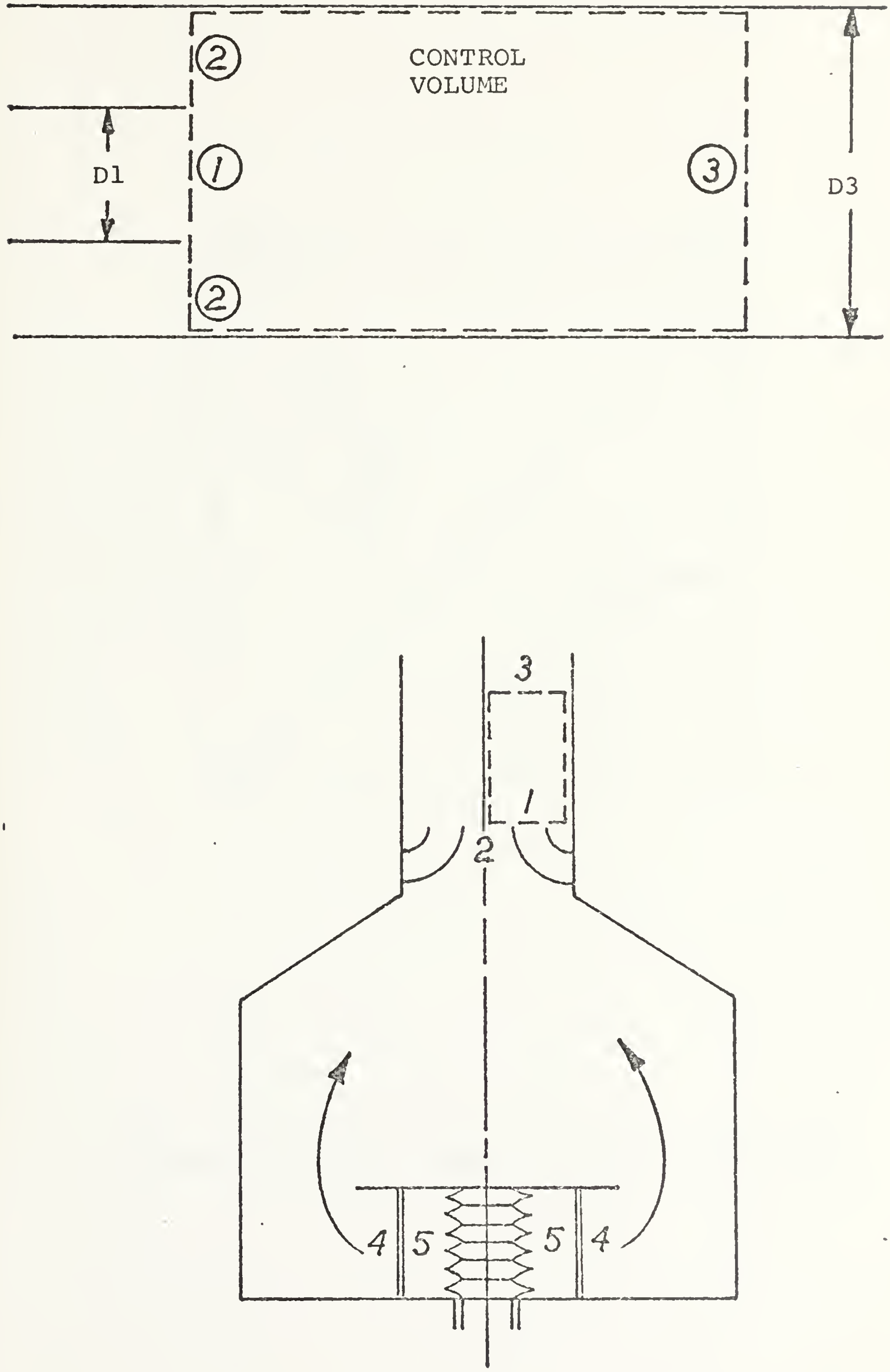
CONTROL
VOLUME
②
①
③
②
D1
D3
3
1
2
4
5
5
4

FIGURE (F-1) EJECTOR NOZZLE MODEL

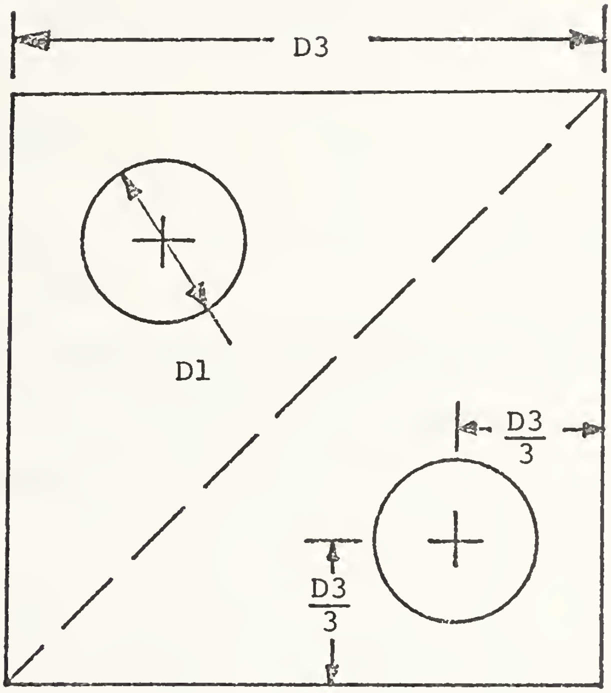
D3
D1
$\frac{D3}{3}$
$\frac{D3}{3}$

FIGURE (F-2) TOP VIEW OF EJECTOR FLOW MODEL

to the control volume shown will yield the flow conditions necessary at station one to assure the desired back pressure.

The following assumptions are made:

(1) isentropic flow from station 4 to 2

(2) isentropic flow from reservoir to ejector nozzle exit

(3) $P_3 = 1$ atm.

(4) $P_{T_1} = 9.5$ atm.

(5) $P_2 = P_1$

(6) $T_{T_1} = 520°R$

(7) $M = 5.0$ at shock

Using normal shock relations the known flow at station (5) can be used to obtain conditions at station (4). For $M = 5.0$, the pressure

$$P_4/P_5 = 29.0$$

$$P_4 = (29)(39.99)$$

$$P_4 = .548 \text{ atm.} \quad ,$$

density

$$\rho_4/\rho_5 = 5.0$$

$$\rho_4 = (5.0)(\rho_o)(\rho_5/\rho_o)$$

$$\rho_4 = (5.0)(.02378\ g)(.01134)$$

$$\rho_4 = .0434 \text{ lb}_m/\text{ft}^3 \quad ,$$

and temperature

$$T_4/T_5 = 5.8$$

$$T_4 = (5.8)(T_o)(T/T_o)$$

$$= (518)(520)(.1667)$$

$$T_4 = 502.76 \text{ °R}$$

can easily be found.

Using the isentropic relations

$$P_4/P_2 = (\rho_2/\rho_4) = (T_2/T_4) \quad ,$$

all conditions at station two can be found in terms of the static pressure:

$$\rho_2 = \rho_4(P_4/P_2)^{1/\gamma}$$

$$\rho_2 = (.0434)(\frac{.548}{P_2})^{1/1.4}$$

and

$$T_2 = T_4(P_4/P_2)^{(\gamma-1)/\gamma}$$

$$T_2 = (502.76)(\frac{.548}{P_2})^{4/1.4} \quad .$$

Since $\dot{m}_2 = \dot{m}_4$, the velocity at 2 can also be found:

$$\dot{m}_2 = \rho_2 U_2(2A_2) = \dot{m}_4$$

where the area is taken as $(2 \cdot A_2)$ since the control volume inlet area (A_2) is only one-half of the total exit area of the flow. Rearranging:

$$U_2 = \frac{\dot{m}_4}{\rho_2 [2(A_3 - A_1)]} * (144)$$

$$= \frac{(6.463)(144)}{\rho_2 (2)(9 - .785)}$$

$$U_2 = \frac{55.9}{\rho_2} \quad .$$

All conditions at station two are now known in terms of P_2. Again using isentropic relations, conditions at station one can be determined in terms of P_1:

$$T_1 = T_{T_1} \left(\frac{P_{T_1}}{P_1}\right)^{-(\gamma-1)/\gamma}$$

$$T_1 = 520 \left(\frac{9.5}{P_1}\right)^{-.4/1.4} \quad °R$$

and

$$\rho_1 = \rho_0 \left(\frac{P_{T_0}}{P_1}\right)$$

$$\rho_1 = (.02378\ g) \left(\frac{9.5}{P_1}\right)^{-1/1.4} \quad lb_m/ft^3 \quad .$$

To find the velocity at station one:

$$T_{T_1} = T_1(1 + \frac{\gamma-1}{2} M_1^{\,2}) \quad .$$

Since $M_1^{\,2} = \frac{U_1^{\,2}}{\gamma R T_1}$,

$$U_1 = \sqrt{(\frac{T_{T_1}}{T_1} - 1)(\frac{2\gamma R T_1}{\gamma - 1})\, g} \qquad \text{ft/sec} \quad .$$

Hence all conditions at station one are known in terms of P_1.

If P_1 ($=P_2$) is known, equations (E-1) and (E-2) can be combined to find U_3 and ρ_3. A computer program was written to vary the values of D_1 and D_3 and to iteratively increase P_1 from a set value until it satisfied the energy equation. An explanation of the program EJECTOR, a listing, and the results in tabular form are found in this appendix. Figure (26) shows the results in graphical form. The broken line at a pressure of 0.617 represents the total pressure downstream of the shock assuming P_o (upstream) = 10 atm. and $M = 5.0$. Acceptable combinations of D_1 and D_3 must result in a pressure P_2 below this line.

B. EXHAUST LENGTH

The length of the exhaust stack must be long enough to ensure complete mixing of the primary flow from the ejector nozzles and the secondary flow from the cylindrical nozzles.

The model used for mixing of the two flows is shown in figure (F-3).

Bailey [Ref. 6] defines a non-dimensional spread parameter which is a good approximation to experimental data:

$$\sigma = 24 \frac{U_{mean}}{U_1} \tag{F-4}$$

where

$$U_{mean} = \frac{U_1 + U_2}{2} \quad .$$

The non-dimensional similarity variable for the mixing zone was defined to be

$$\eta = \frac{\sigma Y}{X} \quad . \tag{F-5}$$

A value of $\eta = 1.84$ gives the outer edge of the mixing zone where the velocity equals 99% of the centerline value.

The minimum value of the mixing length is where the edge of the mixing zone touches the side walls, or when

$$Y = Y_{max} = \frac{D_3 - D_1}{2} \quad .$$

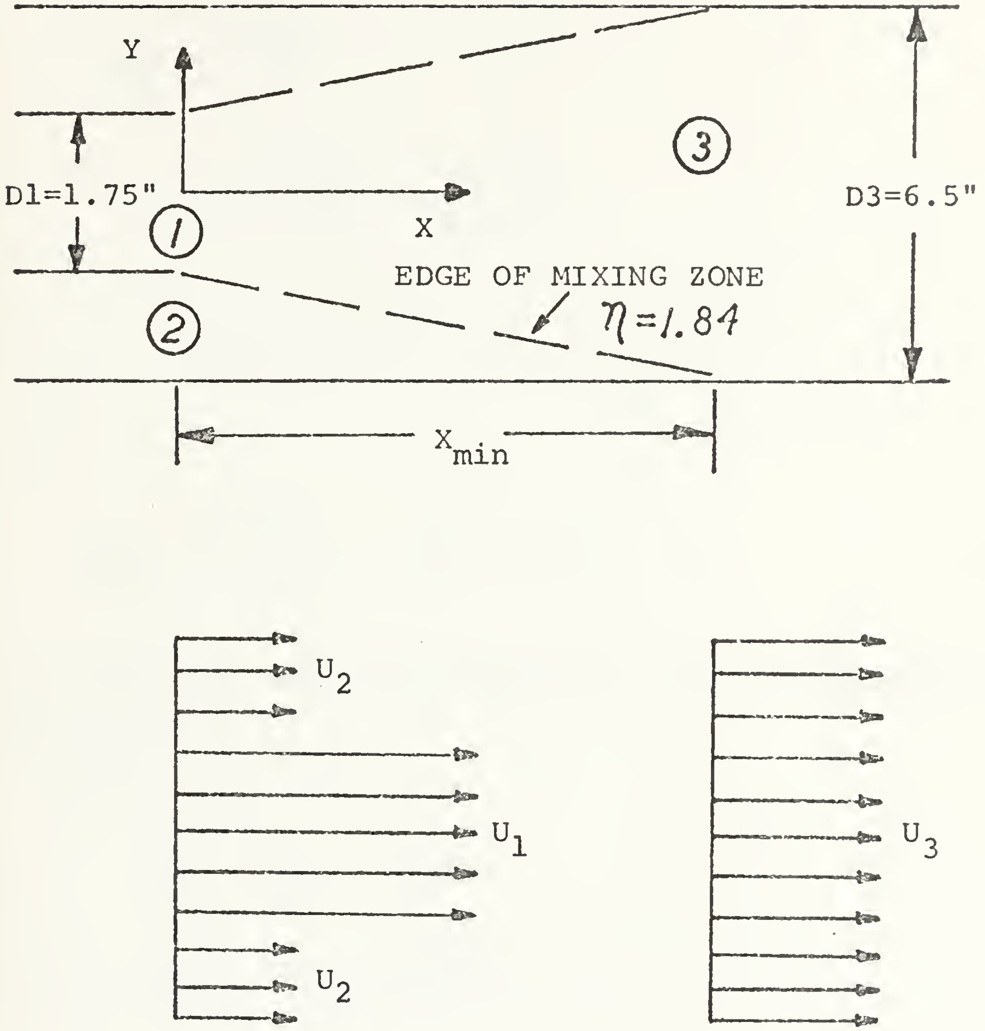
Y
X
D1=1.75"
D3=6.5"
①
②
③
EDGE OF MIXING ZONE
$\eta=1.84$
X_{min}
U_2
U_1
U_2
U_3

FIGURE (F-3) EJECTOR FLOW MIXING MODEL

Substituting $Y = Y_{max}$ and equation (F-4) into equation (F-5), the minimum mixing length, X_{min}, can be found:

$$X_{min} = \frac{\sigma Y_{max}}{\eta}$$

$$= 24 \frac{U_{mean}}{U_1} \frac{(D_3 - D_1)}{2(1.84)}$$

$$= 6.522(4.85 - 1.75) \frac{(U_1 + U_2)}{2U_1}$$

$$X_{min} = \frac{6.522}{2} (1 + \frac{U_2}{U_1}) (3.1) \quad . \qquad \text{(F-6)}$$

Using values from program EJECTOR for the combination of D_1 and D_3 chosen:

$U_1 = 1860$ ft/sec

$U_2 = 664$ ft/sec .

Putting these values in equation (F-6):

$$X_{min} = \frac{6.522}{2} (1 + \frac{664}{1860}) (3.1)$$

$$X_{min} = 13.72 \text{ inches} \quad .$$

The exhaust stack must therefore extend a minimum of 13.72 inches beyond the ejector nozzle exit. Figure (F-4) shows the length of the exhaust stack with the ejector nozzles installed.

C. NOZZLE SHAPE

For the chosen combination of $D_1 = 1.75$ inches and $D_3 = 6.5$ inches

$$U_1 = 1860 \text{ ft/sec} \quad .$$

(See section D of this Appendix.) This velocity is clearly supersonic. To determine the throat area required for the given exit diameter and flow velocity, the exit Mach number must first be found. Since

$$M^2 = \frac{U^2}{A^2}$$

$$M^2 = \frac{U^2}{\gamma RT} \quad ,$$

and

$$T = T_o/(1 + \frac{\gamma-1}{2} M^2) \quad ,$$

then, after substituting and rearranging, the Mach number can be expressed as

$$M = \sqrt{\frac{K}{1 - \frac{\gamma-1}{2} (K)}}$$

where

$$K = \frac{U^2}{\gamma R g T_o} \quad .$$

Inserting the appropriate values:

$$M = \sqrt{\frac{2.77}{1 - .554}}$$

$$M = 2.49 \quad .$$

For isentropic flow through the nozzle

$$A/A^* = \frac{1}{M}\left[\left(\frac{2}{\gamma+1}\right)\left(1 + \frac{\gamma-1}{2} M^2\right)\right]^{\frac{\gamma+1}{2(\gamma-1)}} \quad .$$

For M = 2.49

$$A/A^* = 2.61 \quad .$$

Solving for throat height:

$$A^* = \frac{\pi(1.75)^2}{4}\left(\frac{1}{2.61}\right)$$

$$A^* = .921 \text{ in}^2 \quad ,$$

or

$$D^* = \sqrt{\frac{4A^*}{\pi}}$$

$$D^* = 1.08 \text{ inches} \quad .$$

The ejector nozzles were fabricated from plexiglas with the throat diameter of 1.08 inches. Figure (F-4) shows the details of the ejector nozzle geometry.

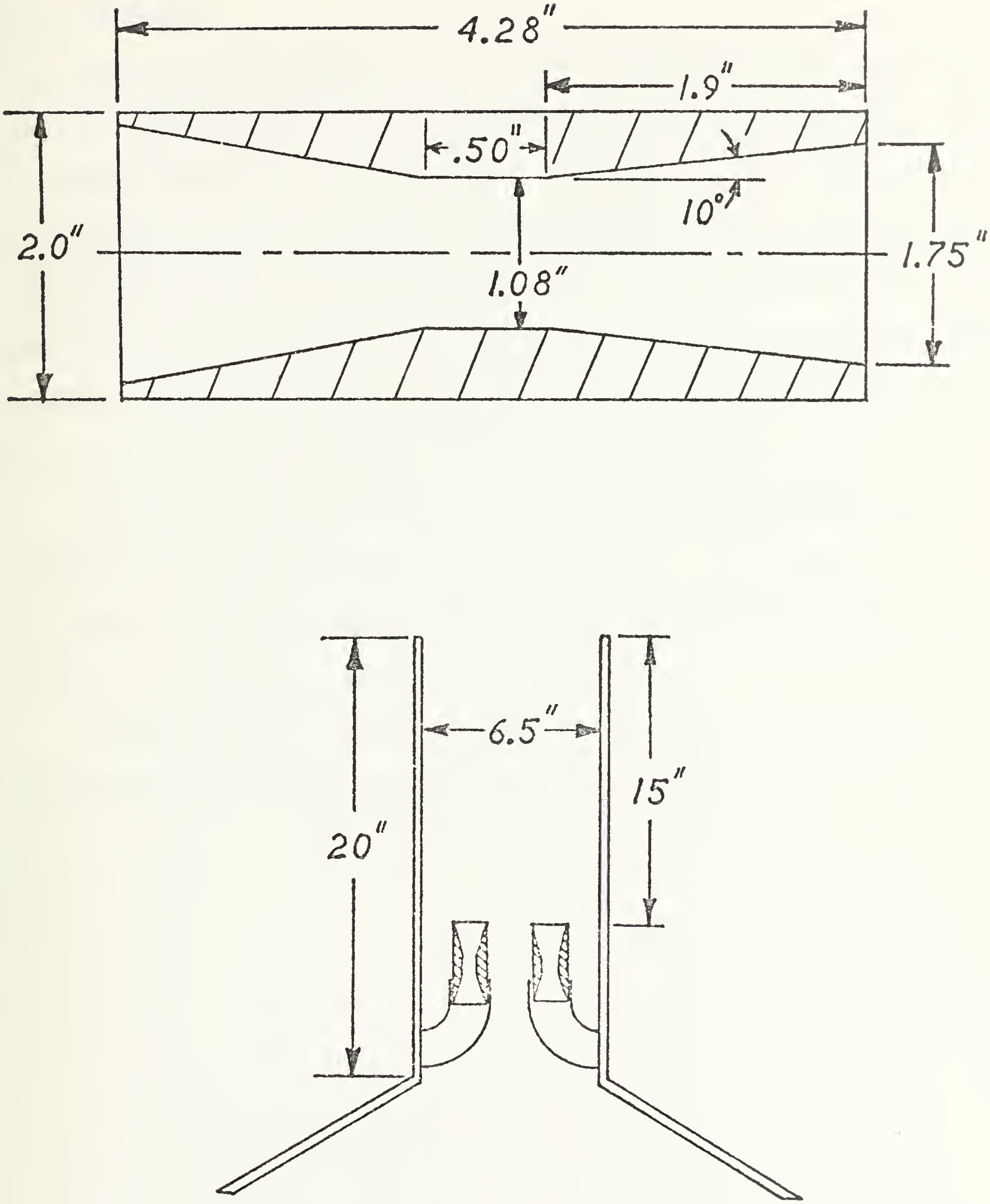
4.28"
1.9"
.50"
10°
2.0"
1.08"
1.75"
6.5"
20"
15"

FIGURE (F-4) EJECTOR NOZZLE GEOMETRY

D. EJECTOR

The program EJECTOR solves the continuity and momentum equations for different combinations of nozzle diameter and exhaust stack width assuming a starting value of pressure at stations one and two of 0.37 atmospheres. The pressure P_1 is increased in increments of 0.0001 atmospheres until the flow conditions at 1, 2 and 3 satisfy the energy equation. When the energy equation is satisfied, the values are printed, and the process is repeated with new values of D_1 and D_3.

Inputs to the program include conditions immediately downstream of the shock: ρ_4 (lb_m/ft^3) , T_4 (°R) , P_4 (atm.) and $\dot{m}_4$ (lb_m/ft^3) ; and total temperature (°R) and total pressure (atm.) at station one.

Outputs are D_1 and D_3 (both in inches), P_1 $(=P_2)$ in atmospheres, and U_1 and U_2, both in ft/sec.

Table F-1 Symbols for Program EJECTOR

Computer Notation	Algebraic	Description
A A2 A3	A_1 A_2 A_3	Flow area (in^2)
P1 P2 P3 P4	P_1 P_2 P_3 P_4	Static pressure (atm.)
R1 R2 R3 R4	ρ_1 ρ_2 ρ_3 ρ_4	Static density (lb_m/ft^3)
M1 M2 M3 M4	$\dot{m}_1$ $\dot{m}_2$ $\dot{m}_3$ $\dot{m}_4$	Mass flow (lb_m/sec)
G	γ	Specific heat ratio
R	R	Gas constant for air (53.3 ft-lb_f/lb_m °R)
C1	C_p	Specific heat @ constant pressure
J	J	778.26 ft-lb_f/BTU
T1 T2 T3 T4	T_1 T_2 T_3 T_4	Static temperatures (°R)
T	T_{T1}	Stagnation temperature (°R)
P	P_{T1}	Stagnation pressure (atm.)
U1 U2 U3	U_1 U_2 U_3	Velocities at stations 1, 2 and 3 respectively (ft/sec)
K	$2*g$	
L	C_p*J	
D1	D_1	Diameter of one of the two ejector nozzles (inches)
D3	D_3	Length of one side of exhaust stack.

D. LIST OF COMPUTER PROGRAM "EJECTOR" AND RESULTS

```
10 PRINT "INPUT CONDITIONS AT STA. 4 [illegible]"
20 PRINT "INPUT RHO4(LB/CU FT),T4(R),P4(ATM),M4(LB/SEC)"
30 INPUT R4,T4,P4,M4
40 PRINT "INPUT TOTAL CONDITIONS AT STA 1"
50 PRINT "INPUT TT1(R),PT1(ATM)"
60 INPUT T,P
105 P3=1
120 G=1.4
130 R=53.3
140 J=778.26
150 C1=0.241
160 PRINT "D1","D3","P1","U1","U2"
170 PRINT
174 FOR D1=1 TO 2.5 STEP 0.25
176 A=2*3.1416*D1↑2/(4*144)
177 P1=0.37
178 FOR D3=6 TO 9 STEP 0.5
180 A3=D3↑2/144
186 A2=A3-A-(2*(D3/3)*D1/144-A/2)
200 P2=P1
210 R2=R4*(P4/P2)↑(1/G)
220 T2=T4*(P4/P2)↑((G-1)/G)
230 U2=M4/(R2*A2)
240 T1=T*(P/P1)↑((1-G)/G)
250 R1=(P/(R*T))*(P/P1)↑(-1/G)*2116
260 U1=SQR(((T/T1)-1)*2*G*R*T1*32.17/(G-1))
270 C3=R1*U1*A/A3+R2*U2*A2/A3
280 U3=(R1*U1↑2*A/A3+(P2-P3)*2116*32.17+R2*U2↑2*A2/A3)/C3
290 R3=R1*U1*A/(U3*A3)+R2*U2*A2/(U3*A3)
300 T3=P3*2116/(R*R3)
310 M1=R1*U1*A
320 M2=R2*U2*A2
330 M3=R3*U3*A3
340 K=2*32.17
350 L=C1*J
360 W1=M1*(L*T1+U1↑2/K)
370 W2=M2*(L*T2+U2↑2/K)
380 W=W1+W2
390 X=M3*(L*T3+U3↑2/K)
400 D=W-X
402 IF D<10 THEN 410
403 IF P1>0.65 THEN 410
404 P1=P1+0.001
406 GOTO 200
410 PRINT D1,D3,P1,U1,U2
420 NEXT D3
430 PRINT
440 NEXT D1
450 END
```

RESULTS OF COMPUTER PROGRAM "EJECTOR"

D1 (in)	D3 (in)	P1 (atm)	U1 (fps)	U2 (fps)
1.5	6	0.578	1853.784608	[illegible]
1.5	6.5	0.619	1838.764831	[illegible]
1.5	7	0.651	1827.447956	[illegible]
1.75	6	0.523	1874.970928	[illegible]
1.75	6.5	0.562	1853.818244	[illegible]
1.75	7	0.598	1846.38128	[illegible]
1.75	7.5	0.633	1834.126552	[illegible]
2	6	0.47	1896.700606	[illegible]
2	6.5	0.507	1881.224773	[illegible]
2	7	0.542	1867.506946	[illegible]
2	7.5	0.575	1854.30822	[illegible]
2	8	0.605	1843.825040	[illegible]
2	8.5	0.634	1833.41798	[illegible]
2	9	0.651	1827.447956	[illegible]
2.5	6	0.377	1938.786207	[illegible]
2.5	6.5	0.408	1924.111707	[illegible]
2.5	7	0.438	1910.551470	[illegible]
2.5	7.5	0.469	1897.124775	[illegible]
2.5	8	0.498	1885.045807	[illegible]
2.5	8.5	0.527	1873.386149	[illegible]
2.5	9	0.554	1862.873692	[illegible]
2.25	6	0.422	1917.709925	[illegible]
2.25	6.5	0.456	1902.687229	[illegible]
2.25	7	0.488	1889.161476	[illegible]
2.25	7.5	0.52	1876.164316	[illegible]
2.25	8	0.55	1864.41135	[illegible]
2.25	8.5	0.579	1853.410842	[illegible]
2.25	9	0.606	1843.151306	[illegible]

APPENDIX G

LISTING OF BOUNDARY LAYER BLEED COMPUTER PROGRAM

```
10 INPUT M,V,G,A,X,A9,P1,P2,U8
20 PRINT "M=";M;"REYNOLD'S NUMBER=";V;"GAMMA=";G;"A=";A
30 PRINT "X=";X;"A9=";A9;"P1=";P1;"P2=";P2
40 PRINT "VELOCITY AT THE EDGE OF THE BOUNDARY LAYER IS";U8
50 INPUT N5
60 PRINT "N5=";N5
70 C1=(1+((G-1)/4)*(M↑2))
80 C2=(G-1)*(M↑2)/(8*A)
90 N8=PI/(2*A)
100 D=N8*C1*X*SQR(2/V)
110 PRINT "N8=";N8;"D=";D
120 Q7=P1/P2
130 PRINT "PRESSURE RATIO IS";Q7
140 G1=(G-1)/G
150 Q6=Q7↑G1
160 G2=2/(G-1)
170 G3=1/G2
180 G4=(G+1)/(2*(G-1))
190 PRINT "CI=";C1;"C2=";C2;"G1=";G1;"Q6=";Q6;"G2=";G2;"G3=";G3;"G4=";G4
200 DIM N[6],B[6],Y[6],U[6],W[6],J[6],M[6],R[6],F[6],Z[6],S[6],H[6]
210 FOR I=1 TO.5
220 N[I]=0.2*I*N5
230 B[I]=N[I]*X*SQR(2/V)
240 Y[I]=B[I]*C1+(C2*B[I]*SIN(2*A*N[I]))/N[I]
250 U[I]=SIN(A*N[I])
260 NEXT I
270 PRINT "N4=";N[4];"B4=";B[4];"Y4=";Y[4];"U4=";U[4]
280 PRINT "Y1=";Y[1];"Y2=";Y[2];"Y3=";Y[3];"Y4=";Y[4];"Y5=";Y[5]
```

LISTING OF BOUNDARY LAYER BLEED PROGRAM (Continued)

```
290 W[1]=0.5*U[1]
300 W[2]=0.5*(U[1]+U[2])
310 W[3]=0.5*(U[2]+U[3])
320 W[3]=0.5*(U[2]+U[3])
330 W[4]=0.5*(U[3]+U[4])
340 W[5]=0.5*(U[4]+U[5])
350 J[1]=Y[1]
360 J[2]=Y[2]-Y[1]
370 J[3]=Y[3]-Y[2]
380 J[4]=Y[4]-Y[3]
390 J[5]=Y[5]-Y[4]
400 FOR I=1 TO 5
410 M[I]=SQR((W[I]↑2)/(((A9/U8)↑2)-((G-1)/2)*(W[I]↑2)))
420 R[I]=G*P1*(1+((G-1)/2)*(M[I]↑2))/(A9↑2)
430 F[I]=U8*R[I]*J[I]*W[I]
440 Z[I]=SQR(G2*((Q6*(1+G3*(M[I]↑2)))-1))
450 S[I]=(1+G3*(Z[I]↑2))/(1+G3*(M[I]↑2))
460 H[I]=((S[I]↑G4)*M[I]*J[I])/Z[I]
470 NEXT I
480 H=H[1]+H[2]+H[3]+H[4]+H[5]
490 H6=12*H
500 H7=H/D
510 D[5]=Y[5]/D
520 F=F[1]+F[2]+F[3]+F[4]+F[5]
530 PRINT "W1=";W[1];"W2=";W[2];"W3=";W[3];"W4=";W[4];"W5=";W[5]
540 PRINT "D=";D;"J1=";J[1];"J2=";J[2];"J3=";J[3];"J4=";J[4];"J5=";J[5]
550 PRINT "D5=";D[5]
560 PRINT "M1=";M[1];"M2=";M[2];"M3=";M[3];"M4=";M[4];"M5=";M[5]
570 PRINT "R1=";R[1];"R2=";R[2];"R3=";R[3];"R4=";R[4];"R5=";R[5]
580 PRINT "F1=";F[1];"F2=";F[2];"F3=";F[3];"F4=";F[4];"F5=";F[5]
590 PRINT "Z1=";Z[1];"Z2=";Z[2];"Z3=";Z[3];"Z4=";Z[4];"Z5=";Z[5]
600 PRINT "MASS FLOW INTO BLEED HOLE IS";F;"SLUGS/SEC"
610 PRINT "H1=";H[1];"H2=";H[2];"H3=";H[3];"H4=";H[4];"H5=";H[5]
620 PRINT "PRESSURE RATIO IS";Q7;"BLEED HOLE WIDTH IS";H;"FEET OR";H6;"INCHES"
630 PRINT "RATIO OF BLEED HOLE WIDTH TO BOUNDARY LAYER THICKNESS IS";H7
640 PRINT "FRACTION OF BOUNDARY REMOVED IS";D[5]
650 END
```

LIST OF REFERENCES

1. Ortwerth, Dr. James, AFWL, Kirtland AFB, personal communication via Professor A. E. Fuhs.

2. Air Force Weapons Laboratory report TR 74-005, Cylindrical Gas Dynamic Laser, written by the staff of the AVCO Everett Research Laboratory, December, 1973.

3. Liepmann, H. W., and Roshko, A., Elements of Gasdynamics, John Wiley & Sons, 1957.

4. Shapiro, A. H., The Dynamics and Thermodynamics of Compressible Fluid Flow, v. 1, Ronald Press, 1953.

5. Christiansen, W. H., Hertzberg, A., and Russell, D. A., Gasdynamic Laser, Theory and Practice, lecture notes from AIAA short course, 1973.

6. Bailey, D. L., An Analytical and Experimental Analysis of Factors Affecting Exhaust System Performance in Sea Level Static Jet Engine Test Facilities, Engineer's Thesis, Naval Postgraduate School, Monterey, 1972.

7. Stewertson, K., The Theory of Laminar Boundary Layers in Compressible Fluids, Oxford at the Clarendon Press, 1972.

8. Donoghue, D. R., and Fuhs, A. E., "Supersonic or Hypersonic Boundary Layer Bleed", April, 1975, submitted to The Physics of Fluids.

9. Lukasiewicz, J., "Diffusers for Supersonic Wind Tunnels", Journal of the Aeronautical Sciences, September, 1953.

10. Schlichting, H., Boundary-Layer Theory, Sixth Edition, McGraw-Hill, 1968.

INITIAL DISTRIBUTION LIST

		No. Copies
1.	Defense Documentation Center Cameron Station Alexandria, Virginia 22314	2
2.	Library, Code 0212 Naval Postgraduate School Monterey, California 93940	2
3.	Dr. R. W. Bell Chairman, Department of Aeronautics Naval Postgraduate School Monterey, California 93940	1
4.	Professor A. E. Fuhs, Code 57Fu Department of Aeronautics Naval Postgraduate School Monterey, California 93940	6
5.	Ens. D. R. Donoghue 137 Creekdale Walnut Creek, California 94595	2
6.	William Volz Code 320 Naval Air Systems Command Washington, D.C. 20360	1
7.	Ronald Dettling Naval Weapons Center China Lake, Ca. 93555	3
8.	Dr. Jim Ortwerth AFWL Kirtland AFB, N.M.	1
9.	Captain James Wilson, USN PMS-405 Naval Sea Systems Command Washington, D.C. 20360	1
10.	LCDR. Hugo Hardt Code 350 Naval Air Systems Command Washington, D.C. 20360	1

11. Dr. W. R. Warren 1
Director, Aerodynamics and Propulsion Laboratory
Aerospace Corporation
Los Angeles Ca. 90245

12. Dr. Barry Hagge 1
AFWL
Kirtland AFB, New Mexico

13. Professor O. Biblarz 1
Department of Aeronautics
Naval Postgraduate School
Monterey, Ca. 93940

14. Dr. George Sutton 1
AVCO Everett Research Laboratory
2385 Revere Beach Parkway
Everett, Massachusetts

161383

Thesis
D6458 Donoghue
c.1 An experimental analysis of a cylindrical shock wave for use in a cylindrical gas dynamic laser.

161383

Thesis
D6458 Donoghue
c.1 An experimental analysis of a cylindrical shock wave for use in a cylindrical gas dynamic laser.

thesD6458
An experimental analysis of a cylindrica
3 2768 002 00592 8
DUDLEY KNOX LIBRARY